

Rotational Support of Giant Clumps in High- z Disc Galaxies

Daniel Ceverino¹*, Avishai Dekel¹†, Nir Mandelker¹, Frederic Bournaud²,
Andreas Burkert³, Reinhard Genzel⁴, Joel Primack⁵

¹*Racah Institute of Physics, The Hebrew University, Jerusalem 91904, Israel*

²*Laboratoire AIM Paris-Saclay, CEA/IRFU/SAP - CNRS - Université Paris Diderot, 91191 Gif-sur-Yvette Cedex, France*

³*Universitäts-Sternwarte Ludwig-Maximilians-Universität, Scheinerstr. 1, München, D-81679, Germany*

⁴*Max-Planck-Institut für Extraterrestrische Physik, Giessenbachstr. 1, D-85748 Garching, Germany*

⁵*Department of Physics, University of California, Santa Cruz, CA, 95064, USA*

ABSTRACT

We address the internal support against total free-fall collapse of the giant clumps that form by violent gravitational instability in high- z disc galaxies. Guidance is provided by an analytic model, where the proto-clumps are cut from a rotating disc and collapse to equilibrium while preserving angular momentum. This model predicts prograde clump rotation, which dominates the support if the clump has contracted to a surface-density contrast $\gtrsim 10$. This is confirmed in hydro-AMR zoom-in simulations of galaxies in a cosmological context. In most high- z clumps, the centrifugal force dominates the support, $\mathcal{R} \equiv V_{\text{rot}}^2/V_{\text{circ}}^2 > 0.5$, where V_{rot} is the rotation velocity and the circular velocity V_{circ} measures the potential well. The clump spin indeed tends to be in the sense of the global disc angular momentum, but substantial tilts are frequent, reflecting the highly warped nature of the high- z discs. Most clumps are in Jeans equilibrium, with the rest of the support provided by turbulence, partly driven by the gravitational instability itself. The general agreement between model and simulations indicates that angular-momentum loss or gain in most clumps is limited to a factor of two. Simulations of isolated gas-rich discs that resolve the clump substructure reveal that the cosmological simulations may overestimate \mathcal{R} by $\sim 30\%$, but the dominance of rotational support at high z is not a resolution artifact. In turn, isolated gas-poor disc simulations produce at $z = 0$ smaller gaseous non-rotating transient clouds, indicating that the difference in rotational support is associated with the fraction of cold baryons in the disc. In our current cosmological simulations, the clump rotation velocity is typically more than twice the disc dispersion, $V_{\text{rot}} \sim 100 \text{ km s}^{-1}$, but when beam smearing of ≥ 0.1 arcsec is imposed, the rotation signal is reduced to a small gradient of $\leq 30 \text{ km s}^{-1} \text{ kpc}^{-1}$ across the clump. The velocity dispersion in the simulated clumps is comparable to the disc dispersion so it is expected to leave only a marginal signal for any beam smearing. Retrograde minor-merging galaxies could lead to massive clumps that do not show rotation even when marginally resolved. Testable predictions of the scenario as simulated are that the mean stellar age of the clumps, and the stellar fraction, are declining linearly with distance from the disc center.

Key words: cosmology — galaxies: evolution — galaxies: formation — galaxies: kinematics and dynamics — galaxies: spiral — stars: formation

1 INTRODUCTION

More than half the massive star-forming galaxies observed in the redshift range $z \sim 1 - 3$ (e.g. Steidel et al. 1999; Adelberger et al. 2004; Daddi et al. 2004) turn out to be thick, turbulent, extended, rotating discs that are highly perturbed by transient elongated features and giant clumps (Genzel et al. 2006; Elmegreen & Elmegreen

2006; Genzel et al. 2008; Stark et al. 2008; Law et al. 2009; Förster Schreiber et al. 2009, 2011). First dubbed “clump-cluster” and “chain” galaxies, based on their face-on or edge-on images (Cowie et al. 1995; van den Bergh 1996; Elmegreen et al. 2004, 2005, 2007), a significant fraction of these galaxies ($> 50\%$ for the more massive ones) are confirmed by spectroscopic measurements to be rotating discs (Genzel et al. 2006; Shapiro et al. 2008; Förster Schreiber et al. 2009). The massive discs of $\sim 10^{11} M_{\odot}$ in baryons and radii $\sim 10 \text{ kpc}$ tend to have

* E-mail: ceverino@phys.huji.ac.il

† E-mail: dekel@phys.huji.ac.il

high rotation-to-dispersion ratios of $V_{\text{rot}}/\sigma \sim 2 - 7$ (Cresci et al. 2009) with high $\sigma \sim 20 - 80 \text{ km s}^{-1}$ (one dimensional), while among the smaller galaxies there is a larger fraction of “dispersion-dominated” galaxies with $V_{\text{rot}}/\sigma < 2$ (Law et al. 2007, 2009; Förster Schreiber et al. 2009).

These clumpy high-redshift discs are very different from the low-redshift disc galaxies of similar masses and sizes. In a typical $z \sim 2$ disc, up to half its restframe-UV light is emitted from a few giant clumps, each of a mass $\sim 10^9 M_{\odot}$, a characteristic size $\sim 1 \text{ kpc}$ that is resolved in HST imaging, and a star-formation rate (SFR) that could reach tens of $M_{\odot} \text{ yr}^{-1}$ (Elmegreen et al. 2004; Elmegreen & Elmegreen 2005; Förster Schreiber et al. 2006; Genzel et al. 2008). The non-negligible clump sizes, and the fact that the SFRs are not extremely high, indicate that the clumps are supported against catastrophic free-fall collapse. These clumps are much larger than the typical star-forming molecular clouds of $\sim 10^5 - 10^6 M_{\odot}$ in local galaxies¹. This pronounced clumpy morphology is not a bandshift artifact in the sense that the restframe-UV images of low-redshift galaxies would not appear as clumpy if observed at high redshift with limited resolution and low signal-to-noise ratio (Elmegreen et al. 2009), and indeed the high-redshift clumps are also seen in restframe-optical emission (Genzel et al. 2008; Förster Schreiber et al. 2009, 2011). Estimates of the molecular gas to baryon fraction in the high-redshift discs, based on CO measurements, range from 0.2 to 0.8, with an average of $\sim 0.4 - 0.6$ at $z \sim 2$ (Daddi et al. 2008, 2010; Tacconi et al. 2010), systematically higher than the molecular gas fraction of $\sim 0.05 - 0.1$ in today’s discs (Saintonge et al. 2011). This gas may be in large molecular complexes, which give rise to star formation and the associated ionized gas that emits $\text{H}\alpha$. The typical ages of the stellar populations in these clumps are crudely estimated to range from one to several hundred Myr (Elmegreen et al. 2009; Förster Schreiber et al. 2009), on the order of ten dynamical times, indicating that the clumps survive for such durations, but do not age unperturbed for Hubble times. The kinematic properties of $z \sim 2$ clumps are being studied by adaptive-optics $\text{H}\alpha$ spectroscopy (Genzel et al. 2011).

The gravitational fragmentation of gas-rich and turbulent galactic discs into giant clumps has been addressed by simulations in the idealized context of an isolated galaxy (Noguchi 1999; Immeli et al. 2004a,b; Elmegreen et al. 2005; Bournaud et al. 2007; Elmegreen et al. 2008; Bournaud & Elmegreen 2009), and in a cosmological context, using analytic theory (Dekel, Sari & Ceverino 2009, DSC09) and cosmological simulations (Agertz et al. 2009; Ceverino et al. 2010; Genel et al. 2010). According to the standard Toomre instability analysis (Toomre 1964), a rotating disc becomes unstable to local gravitational collapse if its surface density is sufficiently high for its self-gravity to overcome the forces induced by rotation and velocity dispersion that resist the collapse. If the disc is maintained in a marginally unstable state with the maximum allowed velocity dispersion, and the cold fraction of the disc is

about one third of the total mass within the disc radius, as obtained in a steady state (DSC09), the clumps are expected to be as massive as a few percent of the disc mass, with radii $\sim 10\%$ the disc radius. According to this robust theoretical understanding, most of the giant clumps in high-redshift discs were formed *in situ* in the discs by gravitational instability of the gas and cold stars. The perturbed disc induces angular-momentum outflow and mass inflow into the disc centre, partly by clump migration through clump-clump interaction and dynamical friction. In the high- z gas-rich discs, where the clumps are massive, this process operates on a timescale comparable to the orbital time at the disc edge. The gravitational energy gained by the inflow is driving turbulence that helps maintaining the disc in the marginally unstable state (Krumholz & Burkert 2010; Cacciato, Dekel & Genel 2011). The mass inflow contributes to the growth of a central bulge, which in turn tends to stabilize the disc, but the continuous intense streaming of fresh cold gas from the cosmic web into the disc (Birnboim & Dekel 2003; Kereš et al. 2005; Dekel & Birnboim 2006; Ocvirk et al. 2008; Dekel et al. 2009) maintains the high surface density and keeps the instability going for cosmological times (DSC09).

Zoom-in cosmological simulations by Agertz et al. (2009) and Ceverino et al. (2010, CDB10), which employed AMR hydrodynamics, confirmed the theoretical picture. With maximum resolution of 70 pc or less at all times, these simulations approached the physical conditions in star-forming regions, with densities well above $n \sim 10 \text{ cm}^{-3}$ and temperatures of 100 K. Indeed, the empirical values at high redshift are $n(\text{H}_2) \sim 10^3 - 10^4 \text{ cm}^{-3}$ and 30 – 80 K (e.g., Danielson et al. 2011). The simulations, zooming in on haloes of mass $\sim 5 \times 10^{11} M_{\odot}$ at $z \sim 2.3$, typically revealed discs of a few $\times 10^{10} M_{\odot}$ and central bulges of comparable mass. The discs spend periods of $\sim 1 \text{ Gyr}$ in a marginally unstable state where they are continuously forming giant clumps, which account for $\sim 20\%$ of the disc mass at a given time and about half the total star formation rate. In these simulations, the individual clump masses indeed range from 10^8 to a few times $10^9 M_{\odot}$. The mean stellar ages within individual clumps range from 20 to 700 Myr, with a median at 150 Myr and a systematic decline with distance from the disc center (§8), consistent with observations (Elmegreen et al. 2009; Genzel et al. 2011; Förster Schreiber et al. 2011) and analytical estimates (DSC09; Krumholz & Dekel 2010). In these simulations, the clumps remain intact as they form stars and survive moderate supernova-driven outflows (but see other possibilities below). As expected, they migrate to the disc centre on an orbital timescale, where they coalesce with the bulge. External galaxies also come in with the streams — the rare massive ones cause major mergers that help build the spheroid, while the more common small ones join the disc as mini-minor mergers, and can become a minor part of the clump population in or near the disc.

It is still debatable whether the *in situ* giant clumps survive intact under stellar-feedback-driven outflows for durations longer than their migration timescale. There are observations of massive outflows from high- z giant clumps (Genzel et al. 2011), which, in extreme cases, are interpreted as potentially leading to disruption on a timescale

¹ although there are also giant molecular associations of one to a few $10^7 M_{\odot}$ in local galaxies (e.g., in M51, Rand & Kulkarni 1990).

comparable to the orbital time. Theoretical considerations argue that the typical high- z giant clumps are supposed to survive stellar feedback, as long as the SFR efficiency (relative to star formation on a free-fall time) is obeying the local Kennicutt law between SFR and gas density. In this case, energy-driven winds from standard supernovae do not provide enough power for un-binding the giant clumps (DSC09, based on Dekel & Silk 1986). Momentum-driven outflows by stellar radiation and winds, which in principle could be more effective and may be responsible for clump disruption in local galaxies (Murray et al. 2010), are expected to remove only a fraction of the typical giant-clump mass at high redshift (Krumholz & Dekel 2010). It has been argued, however, that the SFR efficiency could have been higher and then the feedback more effective, leading to disruption (Murray et al. 2010). Also, if the surface density is high enough, multiple scattering of photons may drive stronger outflows (Murray et al. 2010; Hopkins, Quataert & Murray 2011, Dekel & Krumholz, in preparation). This motivated Genel et al. (2010) to simulate discs in which enhanced outflows do disrupt the clumps on a dynamical timescale. Even if the clumps are disrupted, the instability is associated with mass inflow within the disc toward bulge formation at its center, as argued by theory and simulations (DSC09, Genel et al. 2010), as also indicated by observations (Genzel et al. 2008; Elmegreen et al. 2009). In this paper, we limit the analysis to five cases simulated as in CDB10, where the clumps survive intact for an orbital time ~ 250 Myr or more, such that the typical clump is caught in what seems to be dynamical equilibrium during its migration to the centre.

Our purpose in this paper is to find out to what extent the simulated giant clumps are in Jeans equilibrium between gravity, internal pressure forces and centrifugal forces, and to identify the mechanisms responsible for the support of the clumps against gravitational collapse. We estimate that the thermal pressure of the $\leq 10^4$ K gas, the pressure floor introduced in order to prevent artificial fragmentation on the grid scale, and the supernova feedback as simulated, each contributes energy per unit mass that amounts to only $\lesssim (10 \text{ km s}^{-1})^2$, which falls short compared to the clump binding energy per unit mass of $(40 - 200 \text{ km s}^{-1})^2$. The main source of pressure in the simulated clumps is the macroscopic turbulent motions in the clumps, adding to a possible centrifugal force contribution if the clumps are rotating. Our main goal is thus to quantify the relative contributions of rotation and pressure by random motions to the support of the clumps against collapse under their own gravity.

Using a simple model, we will quantify the expected rotation of the proto-clump in its own frame as induced by the global disc rotation, and the degree of rotational support after collapse by a given collapse factor under the assumption of conservation of angular momentum. An analysis of the simulated clumps with this simple model in mind will allow us to evaluate the validity of the simple model and to estimate the level of angular-momentum conservation during the clump collapse and evolution. We use five zoom-in cosmological simulations, extending the sample of three used in CDB10. The simulated discs produce giant clumps that form stars and survive for a couple of orbital times until they migrate to the centre and merge with

the bulge. The cosmological simulations, with maximum resolution of 35-70 pc, only marginally resolve the clumps, so we complement our analysis with a convergence test using simulations of isolated discs with different resolutions reaching ~ 1 pc, which allow us to test the effects of clump substructure on the level of rotation support. The combination of cosmological simulations and the simulations of isolated discs with higher resolution enables coverage of a large dynamical range. The cosmological simulations form realistic unstable discs in steady state as they are continuously fed by streams from the cosmic web, while the simulations of isolated discs can follow in more detail the internal structure and dynamics within individual clumps.

This paper is organized as follows. In §2 we describe a simple analytic model for clump support, that will guide our interpretation of the simulation results. In §3 (and Appendix §A) we describe the cosmological simulations and address the kinematics in example discs and giant clumps. In §4 (and Appendix §C) we analyze the clump support in a sample of 77 *in situ* clumps drawn from the cosmological simulations at $z = 2 - 3$. In §5 (and Appendix §B) we study the effect of resolution on the clump support using isolated simulations of gas-rich discs with resolution that ranges from the resolution of the cosmological simulations to a resolution 60 times better. In §6 we address the detectability of clump rotation in $H\alpha$ observations with a given beam width. In §7 we consider the minor population of *ex situ* clumps that joined the discs as minor mergers, and highlight the case of retrograde rotators. In §8 we explore the clumps stellar age and gas fraction gradients across the disc as a testable prediction for the scenario simulated. In §9 we investigate the non-rotational clump support in isolated simulations of gas-poor discs that mimic low- z galaxies. In §10 we summarize our results, discuss them, and draw conclusions.

2 ANALYTIC MODEL

Our analysis is motivated by a simple analytic model, that will guide our interpretation of simulation results.

2.1 Clump Support

We approximate the clump as an axisymmetric rotator with an isotropic velocity dispersion. The Jeans equation inside the clump then reads (e.g. Binney & Tremaine 2008, eq. 4.230)

$$V_{\text{rot}}^2(r, z) = r \frac{\partial \Phi}{\partial r} + \frac{r}{\rho_c} \frac{\partial(\rho_c \sigma_c^2)}{\partial r}. \quad (1)$$

Here r is the polar-coordinate radius from the clump centre, and all other quantities are functions of r and z within the clump: V_{rot} is the average rotational velocity, Φ is the gravitational potential, ρ_c is the mass density, and σ_c is the 1D velocity dispersion. Thermal pressure gradients are ignored, as the temperature is $\leq 10^4$ K, equivalent to $\sigma_c \leq 10 \text{ km s}^{-1}$. In the equatorial plane, the potential well defines the circular velocity of the clump,

$$V_{\text{circ}}^2 = r \frac{\partial \Phi}{\partial r} \simeq \frac{GM(r)}{r}, \quad (2)$$

so

$$V_{\text{circ}}^2 \simeq V_{\text{rot}}^2 - \frac{r}{\rho_c} \frac{\partial(\rho_c \sigma_c^2)}{\partial r}. \quad (3)$$

This separates the contributions of rotation and pressure to the support of the clump against gravitational collapse. If the clump is approximately an isothermal sphere, i.e., $\sigma_c = \text{const.}$ and $\rho_c \propto r^{-2}$, we obtain²

$$V_{\text{circ}}^2 = V_{\text{rot}}^2 + 2\sigma_c^2. \quad (4)$$

The relative contribution of the centrifugal force to the clump support can be expressed by the *rotation parameter*

$$\mathcal{R} \equiv \frac{V_{\text{rot}}^2}{V_{\text{circ}}^2}. \quad (5)$$

According to eq. (4), \mathcal{R} is related to the familiar ratio of rotation to dispersion by

$$\left(\frac{V_{\text{rot}}}{\sigma_c}\right)^2 = 2(\mathcal{R}^{-1} - 1)^{-1}. \quad (6)$$

One can refer to the clump as “rotationally supported” when $\mathcal{R} > 0.5$, namely $V_{\text{rot}}/\sigma_c > \sqrt{2}$.

2.2 Clumps in Wildly Unstable Discs

As described for example in DSC09, the wildly unstable discs self-regulate themselves in a marginally unstable state with a Toomre parameter $Q \simeq 1$. The mutual gravitational interaction between the perturbations in the disc, both the transient features and the bound giant clumps, keeps the disc velocity dispersion at a level that maintains $Q \simeq 1$.

Generalizing §2 of DSC09 to a disc with a rotation curve $V_d \propto r_d^\alpha$, we have

$$Q = [2(1 + \alpha)]^{1/2} \frac{\sigma_d}{V_d} \delta^{-1}, \quad (7)$$

where V_d and σ_d are the disc circular velocity and one-dimensional velocity dispersion respectively, and $\delta = M_d/M_{\text{tot}}$ is the ratio of cold disc mass to total mass inside the disc radius, involving also a stellar spheroid and the inner part of the dark-matter halo. A typical value for an unstable disc in steady state at high redshift is $\delta \sim 0.33$ (DSC09). Note that solid-body disc rotation is $\alpha = 1$, a self-gravitating uniform disc is $\alpha = 0.5$, flat rotation curve is $\alpha = 0$, and Keplerian rotation is $\alpha = -0.5$.

Marginal instability $Q \simeq 1$ corresponds to

$$\delta \simeq [2(1 + \alpha)]^{1/2} \frac{\sigma_d}{V_d}. \quad (8)$$

The characteristic clump initial radius R_{ci} and mass M_c relative to the disc radius R_d and mass M_d as estimated from the “most unstable” mode of Toomre instability are given by

$$\frac{R_{\text{ci}}}{R_d} \simeq \frac{\sqrt{2}\pi}{4(1 + \alpha)^{1/2}} \frac{\sigma_d}{V_d}, \quad \frac{M_c}{M_d} \simeq \left(\frac{R_{\text{ci}}}{R_d}\right)^2. \quad (9)$$

² If the clump was a self-gravitating exponential disc with scale length r_{exp} , the pressure term should have been multiplied by r/r_{exp} (Burkert et al. 2010).

For example, with $V_d/\sigma_d \sim 5$ and $\alpha = 0$, the typical clump mass is $\sim 5\%$ of the disc mass. For a disc of $\sim 10^{11} M_\odot$, we expect clumps of a few times $10^9 M_\odot$. If the disc radius is ~ 5 kpc, the initial clump radius is ~ 1 kpc.

Assume that the clump has contracted by a factor c , from its initial radius to a final radius R_c where it is supported by rotation and pressure,

$$c \equiv \frac{R_{\text{ci}}}{R_c} = \left(\frac{\Sigma_c}{\Sigma_d}\right)^{1/2}, \quad (10)$$

with Σ_c/Σ_d the 2D overdensity in the clump. Note that the contraction factor is not expected to be much larger than two or a few, because when $Q \simeq 1$, the initial unstable perturbation is already not far from being supported against gravitational collapse both by pressure and by rotation. Indeed, the simulations discussed below show typical overall clump overdensities of $\Sigma_c/\Sigma_d \sim 10 - 20$, namely $c \sim 3 - 5$ (Figures 4-6 of Ceverino et al. 2010).

Based on eq. (8) and eq. (9), and using the fact that $V_d^2 = GM_d \delta^{-1}/R_d$, the circular velocity of the bound clump (independent of the disc rotation curve slope α) is

$$V_{\text{circ}}^2 \simeq \frac{GM_c}{R_c} \simeq \frac{\pi}{2} c \sigma_d^2. \quad (11)$$

2.3 Rotation of a Protoclump Patch due to Disc Rotation

We assume that the proto-clump is a small cylindrical patch cut from a purely rotating disc. Let the disc centre be $\vec{r}_d = 0$ and the patch centre \vec{r}_{d0} , and let the disc rotation curve be $V_d(r_d) = r_d^\alpha$ near r_{d0} , with radii and velocities measured in units of r_{d0} and $V_{d0} = V_d(r_{d0})$ respectively.

In the non-rotating inertial frame that is momentarily moving with the centre of the patch, consider a ring of radius r . At a longitude ϕ along the ring (measured from the radius vector \hat{r}_{d0}), the tangential velocity is

$$v(\phi) = r_d^{\alpha-1} (\cos \phi + r) - \cos \phi, \quad (12)$$

where

$$r_d = (1 + 2r \cos \phi + r^2)^{1/2}. \quad (13)$$

In the limit of a small patch, $r \ll 1$, simple algebra yields

$$v(\phi) \simeq r [1 + (\alpha - 1) \cos^2 \phi]. \quad (14)$$

We see that for a disc in solid-body rotation, $\Omega_d = V_d/r_d = \text{const.}$, the patch is also in prograde solid-body rotation with $\Omega_{c,i} = \Omega_d$, as expected. For any smaller α , at $\phi = \pm\pi/2$, namely at $r_d = r_{d0}$, the patch tangential velocity remains the same, $v = (r/r_{d0})V_{d0}$, independent of α . On the other hand, at $\phi = 0$ and π , along the disc radius vector, the disc differential rotation has a retrograde contribution that brings the patch tangential velocity to its α -dependent minimum, $v = \alpha(r/r_{d0})V_{d0}$. This is illustrated in Fig. 1.

Assuming that the disc is uniform within the small patch, by integrating eq. (14) over a circular ring of radius r one obtains the average tangential velocity

$$\langle v(r) \rangle \simeq 0.5(1 + \alpha) \frac{r}{r_{d0}} V_{d0}, \quad (15)$$

with the corresponding average angular frequency independent of r

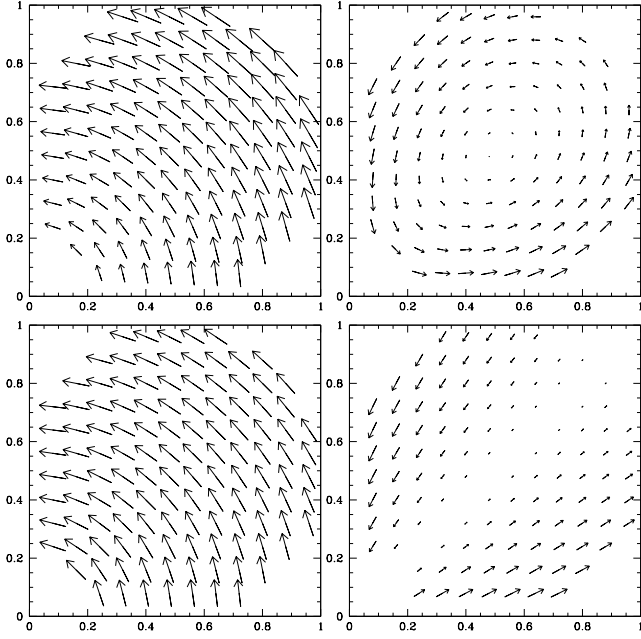


Figure 1. Velocity in a circular patch [centred at (0.5,0.5)], part of a rotating disc [centred at (0,0)]. Left: in the disc frame. Right: about the patch centre. Top: self-gravitating uniform disc, Bottom: flat rotation curve. The tangential component in the patch frame is given in eq. (14).

$$\langle \Omega_{c,i} \rangle \simeq 0.5(1 + \alpha) \Omega_d(r_0). \quad (16)$$

For the four types of rotation curves $\alpha = 1, 1/2, 0, -1/2$, the patch has $\langle \Omega_{c,i} \rangle / \Omega_d \simeq 1, 3/4, 1/2, 1/4$ respectively. In all cases the overall patch rotation is prograde. Note that by assuming that the proto-clump is a cylindrically symmetric patch we are ignoring the distortions by the shear, which are expected to be more severe as the disc rotation curve deviates from solid-body rotation.

In a $Q \simeq 1$ disc, using eq. (15) and eq. (9), the rotation velocity in the initial clump at radius R_{ci} is thus

$$V_{rot,i} \simeq 0.5(1 + \alpha) \frac{R_{ci}}{R_d} V_d \simeq \frac{\sqrt{2}\pi}{8} (1 + \alpha)^{1/2} \sigma_d. \quad (17)$$

For a flat-rotation-curve disc, this is $V_{rot,i} \simeq 0.56 \sigma_d$.

The specific angular momentum at r in the protoclump is $j(r) = \Omega_{c,i} r^2$. For a flat rotation curve, the average specific angular momentum at the proto-clump edge R_{ci} is

$$j(R_{ci}) \simeq \frac{\pi^2}{32} \delta^2 R_d V_d. \quad (18)$$

If the clump surface-density profile mimics a projection of an isothermal sphere, $\Sigma \propto r^{-1}$, the average specific angular momentum over the whole clump is one-third its value at the edge.

2.4 Rotation of a Collapsed Clump

We next assume that the circular patch contracts by a factor c to form a clump in equilibrium, and tentatively make the assumption that angular momentum is conserved during this contraction, to be tested below using the simulations. If angular momentum is conserved, the clump is spun up by the contraction and its rotation velocity becomes

$$V_{rot} \simeq c V_{rot,i} \simeq \frac{\sqrt{2}\pi}{8} (1 + \alpha)^{1/2} c \sigma_d \simeq 0.56 c \sigma_d, \quad (19)$$

where the last equality is for $\alpha = 0$.

A comparison with the circular velocity of the bound clump (eq. (11)) gives

$$\mathcal{R} = \frac{V_{rot}^2}{V_{circ}^2} \simeq \frac{\pi(1 + \alpha)c}{16} \simeq 0.2c. \quad (20)$$

Using eq. (6), the latter corresponds to

$$\frac{V_{rot}}{\sigma_c} \simeq \sqrt{2} (5.1 c^{-1} - 1)^{-1/2}. \quad (21)$$

For $\alpha = 0$, full rotation support ($\mathcal{R} = 1$, $V_{rot}/\sigma_c \gg 1$) is obtained for a collapse factor $c \simeq 5$. Equal contribution from rotation and pressure ($\mathcal{R} = 0.5$, $V_{rot}/\sigma_c = \sqrt{2}$) is obtained for $c \simeq 2.5$. For a rotation curve mimicking a uniform disc, $\alpha = 0.5$, full rotation support is obtained for $c \simeq 3.4$. Thus, if the clumps conserve most of their angular momentum as they collapse to 2D overdensities of ~ 10 , the rotation provides most of the support.

The assumptions of a circular proto-clump patch and conservation of angular-momentum during collapse are quite uncertain. The actual proto-clump is expected to deviate from circularity because of shear, and the disc exerts torques on the clump. These torques could involve the transient features in the disc, clump-clump encounters, dynamical friction and gas drag. Angular-momentum loss could also be associated with mass exchange between the clumps and the disc. These effects are not easy to estimate analytically, and it is not even clear a priori whether the clump rotation as estimated above is an overestimate or an underestimate. Nevertheless, it may serve as a reference for the results obtained from the simulations.

Velocity dispersion provides the rest of the support against gravitational collapse. If a clump has lost all its angular momentum, its internal one-dimensional velocity dispersion, from eq. (4), is

$$\sigma_c \simeq \frac{1}{\sqrt{2}} V_{circ} \simeq \frac{\pi^{1/2}}{2} c^{1/2} \sigma_d \quad (22)$$

for any α . With a collapse factor $c \simeq 3$ we get a maximum possible velocity dispersion of $\sigma_c \simeq 1.5 \sigma_d$. Realistically, with a significant contribution from rotation, the internal velocity dispersion in the clumps is expected to be comparable to and somewhat smaller than that of the disc. Some variations may be expected from clump to clump, but in typical clumps, one does not expect large coherent dispersion residuals to be associated locally with the clumps. In particular, based on eq. (22), any correlation between the clump internal velocity dispersion and the clump surface-density contrast is expected to be rather weak, $\sigma_c \propto \Sigma_c^{1/4}$.

If the resolution allows measuring the velocity dispersion on sub-clump scales, where dissipative collapse may correspond to $c \gg 1$, one may obtain a somewhat larger velocity dispersion in the clumps, but growing only in proportion to $\Sigma_c^{1/4}$. If the dispersion is weighted by $H\alpha$ density, and if it traces regions of surface-density contrast ~ 100 , say, one may expect a positive dispersion residual but still comparable to σ_d , $\sigma_c \sim 2\sigma_d$.

3 GIANT CLUMPS IN COSMOLOGICAL SIMULATIONS

3.1 The cosmological simulations

We use zoom-in hydro cosmological simulations of five moderately massive galaxies with an AMR maximum resolution of 70 pc or better, evolved till after $z \sim 2$. They utilize the ART code (Kravtsov et al. 1997; Kravtsov 2003), which accurately follows the evolution of a gravitating N-body system and the Eulerian gas dynamics using an adaptive mesh. Beyond gravity and hydrodynamics, the code incorporates at the subgrid level many of the physical processes relevant for galaxy formation. They include gas cooling by atomic hydrogen and helium, metal and molecular hydrogen cooling, photoionization heating by a UV background with partial self-shielding, star formation, stellar mass loss, metal enrichment of the ISM, and feedback from stellar winds and supernovae, implemented as local injection of thermal energy. More details concerning the simulation method are provided in an appendix, §A, as well as in Ceverino & Klypin (2009) and CDB10.

The five dark-matter haloes were drawn from N-body simulations of the Λ CDM cosmology with the WMAP5 parameters (§A), in a comoving cosmological box. The haloes were selected to have a virial mass in a desired mass range at $z = 1$. The only other selection criterion was that they show no ongoing major merger at that time. This eliminates less than 10% of the haloes, and has no noticeable selection effect at $z \geq 2$, where our main analysis is performed. Galaxies A, B and C, which have been studied in some detail in CDB10, were selected to have a virial mass $M_v \sim 10^{12} M_\odot$ at $z = 1$ (intended to end up as $(3 - 4) \times 10^{12} M_\odot$ today, somewhat more massive than the Milky Way). Two new galaxies, D and E, were selected to have $M_v \sim 4 \times 10^{12} M_\odot$ at $z = 1$, four times more massive than the other galaxies. The virial properties of the five dark-matter haloes in the snapshots analyzed in the redshift range $z \sim 1.9 - 3$ are listed in Table C1. As expected, the halos of galaxy D and E are more massive than A-C at all times. For example, at $z=2.3$, galaxies A-C have a virial mass of $(0.40, 0.35, 0.61) \times 10^{12} M_\odot$, whereas galaxy D and E have $M_v = (0.94, 1.54) \times 10^{12} M_\odot$, roughly two and four times more massive than galaxy A.

The initial conditions corresponding to each of the selected haloes were filled with gas and refined to a much higher resolution on an adaptive mesh within a zoom-in Lagrangian volume that encompasses the mass within twice the virial radius at $z = 1$, roughly a sphere of comoving radius 1 Mpc. This was embedded in a comoving cosmological box of side 20 and $40 h^{-1}$ Mpc for galaxies A-C and D-E respectively. Each galaxy has been evolved with the full hydro ART and subgrid physics on an adaptive comoving mesh refined in the dense regions to cells of minimum size between 35-70 pc in physical units. This maximum resolution is valid in particular throughout the cold discs and dense clumps, allowing cooling to ~ 300 K and gas densities of $\sim 10^3 \text{ cm}^{-3}$. The dark-matter particle mass is $6.6 \times 10^5 M_\odot$, and the particles representing stars have a minimum mass of $10^4 M_\odot$.

As listed in Table C3, the sample spans roughly an order of magnitude in stellar mass inside the disc radius, ranging from 10^{10} to $10^{11} M_\odot$, in an order that reflects the halo mass. Galaxy B is the smallest, with $M_* = 1.3 \times 10^{10} M_\odot$ inside

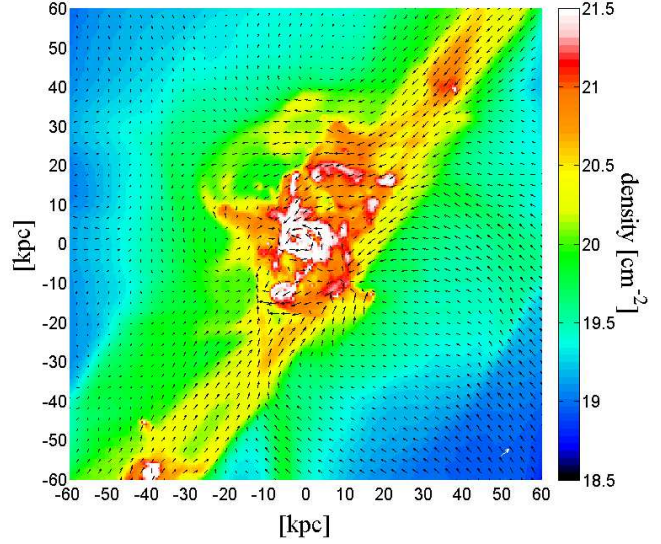


Figure 2. Gas surface density and projected velocity field within the halo of galaxy A at $z = 2.3$. The box roughly encompasses the virial sphere of $R_v = 70$ kpc, and the projection depth along the line of sight is 80 kpc. The arrows represent the velocity field, mass-weighted average along the line of sight, with the white arrow denoting 200 km s^{-1} . Narrow, long streams of cold gas and merging galaxies feed a central rotating disc through a messy interphase region. The disc is seen nearly face on.

$R_d = 3$ kpc at $z=2.3$, and galaxy E is the biggest, with $M_* = 1.4 \times 10^{11} M_\odot$ inside $R_d = 8.5$ kpc at $z = 2.3$. Although this is a small set of galaxies, they span the mass range of typical observed massive star-forming galaxies at $z \sim 2$ (Förster Schreiber et al. 2009), and otherwise no selection criteria was imposed on their properties at $z \sim 2 - 3$. As shown in CDB10, galaxies A-C are consistent with the observed scaling relations of $z \sim 2$ galaxies, including the relation between SFR and stellar mass and the Tully-Fisher relation (Förster Schreiber et al. 2009; Cresci et al. 2009). We can therefore assume that this is a fair sample of galaxies in the relevant mass and redshift range.

3.2 Cold streams and clumpy discs

In order to get familiar with the large-scale context of the disc giant clumps, Fig. 2 shows the gas in the halo of galaxy A at redshift $z \sim 2.3$ – a prototypical case of a high- z clumpy disc (see CDB10). The central disc, of radius ~ 6 kpc, is continuously fed by a few, co-planar narrow streams that extend to hundreds of kpc as they ride the dark-matter filaments of the cosmic web (Dekel et al. 2009, Danovich et al. in prep.). The streams consist of gas at $\sim (1 - 5) \times 10^4 \text{ K}$ as well as clumps of all sizes, the biggest of which are actual galaxies with gas, stars and dark-matter haloes, to be merged with the central galaxy. These supersonic streams penetrate to the central regions of the dark-matter halo where they interact with other streams and the disc and blend into a turbulent interphase region that encompasses about 20% of the virial radius before the gas and stars settle in the central disc and bulge. The complex structure and kinematics in this interphase region, where energy, momentum and angular momentum are being transferred among the different components of gas,

stars, dark matter and radiation, is yet to be investigated. A significant fraction of the gravitational energy gained by the infall into the halo potential well is released as Lyman-alpha radiation (Goerdt et al. 2010, Kasen et al. in prep.), while the cold streams can also be detected in absorption mostly as Lyman-limit systems (Fumagalli et al. 2011). The continuous intense input of cold gas drives the disc into violent disc instability, and helps maintain this configuration in a self-regulated steady state for cosmological times (DSC09, CDB10). Although the disc is perturbed by the continuous instreaming, it does maintain a global disc shape and organized rotation pattern for long periods, and it behaves according to the expectations from Toomre instability (DSC09, CDB10).

Although a detailed analysis of the galaxy properties in these simulations is beyond the scope of the present paper, Table C2 and Table C3 list relevant global properties for the five clumpy discs at the different snapshots used for the analysis of giant clumps. The disc of stars and gas and the stellar bulge are typically comparable in mass. The disc mass ranges from $M_d = 7 \times 10^9 M_\odot$ in galaxy B to $M_d = 7 \times 10^{10} M_\odot$ in galaxy E at $z \sim 2$. Despite their perturbed morphology, the discs rotate with a rotation speed that ranges between $V_d \sim 200 \text{ km s}^{-1}$ in galaxy A and B to $V_d \sim 400 \text{ km s}^{-1}$ in galaxy E. The gas velocity dispersion is high, $\sigma_d = 20 - 60 \text{ km s}^{-1}$, which should lead to Toomre giant clumps with masses of a few percent of the disc mass, $M_c = 10^8 - 10^9 M_\odot$. Many of the simulated galaxy properties resemble the properties of observed clumpy discs at high redshift (Genzel et al. 2006; Elmegreen & Elmegreen 2006; Genzel et al. 2008, 2011; Förster Schreiber et al. 2011), although the simulated gas fractions of 0.1-0.35 are somewhat low compared to the values 0.3-0.6 observed at $z \sim 2$ (Daddi et al. 2010; Tacconi et al. 2010), probably due to an overproduction of stars in the simulation at earlier times by a factor of ~ 2 (CDB10). The underestimated gas fractions suggest that our simulations conservatively underestimate the actual effects of gravitational instability in real galaxies at $z \sim 2$. In particular, the modest gas fractions are likely to cause an underestimate of the degree of dissipation and therefore the clump contraction factor, thus lowering the degree of clump rotational support (§2).

Figure 3 shows the gas in the central disc of galaxy A at redshift $z = 2.3$, face on and edge on. The total mass of baryons in the disc is $1.1 \times 10^{10} M_\odot$, and the gas fraction is 0.35. A comparable baryonic mass is in a stellar bulge. The disc shows a systematic rotation of $\sim 180 \text{ km s}^{-1}$ extending to a radius of $\sim 6 \text{ kpc}$, and certain local perturbations. The density is highly perturbed, with elongated transient features and eight giant clumps, of baryonic masses $(1.8 - 4.0) \times 10^8 M_\odot$ (Table C4). The clumps labelled 1-8 were all formed *in situ* in the disc. They contain stars and gas but show no trace of local dark-matter haloes. There are also two clumps with dark-matter components (labelled 9 and 10), which were formed externally as small galaxies and merged into the disc (§7).

Figure 3 also shows the gas in an edge-on slice of galaxy A at $z = 2.3$. The x axis is the same as in the face-on view, and the depth of the slice is from $y = -2.8$ to $y = -1.6 \text{ kpc}$, chosen to show clumps 1 and 3. While there is clearly a global disc configuration, it is highly perturbed, twisted and

warped, with indications of incoming streams. The clumps seem to be oblate, with the minor axis along the normal to the local disc plane.

Figure 4 shows the gas in the central disc of galaxy E at redshift $z = 2.4$, face on and edge on. This galaxy is more massive, with a baryonic disc mass $5.8 \times 10^{10} M_\odot$, a bulge of $8.2 \times 10^{10} M_\odot$, and gas fraction 0.14. The rotation velocity is 400 km s^{-1} . The rotating disc extends to $\sim 9 \text{ kpc}$, and on top of being locally inhomogeneous and warped, it shows a global asymmetry, indicating intense fresh gas supply. The seven marked clumps have masses in the range $(0.4 - 1) \times 10^9 M_\odot$ (Table C4). The edge-on slice is 2 kpc thick, centered on clump 6 and chosen to contain both the global angular momentum vector of the disc and the angular momentum vector of clump 6. The y axis in this projection coincides with the global angular momentum vector of the disc and the x axis extends from the top right to the center left in the face on projection. Only clump 6 is visible in the image, but it also shows a cut through the perturbation near the top left of the face on image, (between clump 7 and clumps 4 and 5 in that image).

Figure 5 shows the evolution of the face-on gas disc in galaxy E in parts of its continuous clumpy phase, from $z = 3$ to $z = 2$. At $z = 2$, the disc seems to tentatively stabilize in a less perturbed configuration, but it resumes its clumpy phase soon thereafter, to fade away only at $z \sim 1.4$, after which the gas disc shrinks and becomes less perturbed. Right before $z = 3$, the galaxy suffered a 1:4 merger, which makes the bulge-to-disc mass ratio as high as ~ 2 at $z = 3$. Between $z = 3$ and $z = 2$, the disc is growing by smoother gas inflow. This makes the disc double its mass (and increase its size by 50%), while the bulge mass grows only by 30%, reducing the bulge-to-disc mass ratio to ~ 1 at $z = 2$. During this period, the disc-to-total mass ratio within the disc radius remains near 0.2. This configuration agrees with the cosmological steady state of a clumpy disc, as predicted by DSC09. The onset and termination of the violent instability phase is determined by several factors including the evolution of the cosmological accretion rate and the accretion and merger history of the specific galaxy, the star-formation history and evolution of stellar fraction in the disc, and the growth of the stabilizing bulge (DSC09, Agertz et al. 2009; Martig et al. 2009; Cacciato, Dekel & Genel 2011).

3.3 Zoom-in on a few typical clumps

We describe in §C how we identify the clumps in the simulated discs and measure their properties. This includes identifying the clump center and its major plane, measuring the density and velocity profiles within the clump, obtaining a clump radius and mass in the different components, as well as the associated circular velocity, evaluating the effective rotation velocity, velocity dispersion and rotation parameter, and estimating the clump density contrast compared to the disc and the associated contraction factor.

We start with a zoom-in on the dynamical properties of a few typical clumps formed *in situ* in our simulated discs. Figure 6 shows face-on and edge-on views of the gas density and velocity field in clump 1 of galaxy A at $z \simeq 2.3$. This clump is located roughly half way between the galaxy centre and the disc edge. It is the most massive clump in that snapshot, with baryon mass $M_c = 3.9 \times 10^8 M_\odot$ inside the

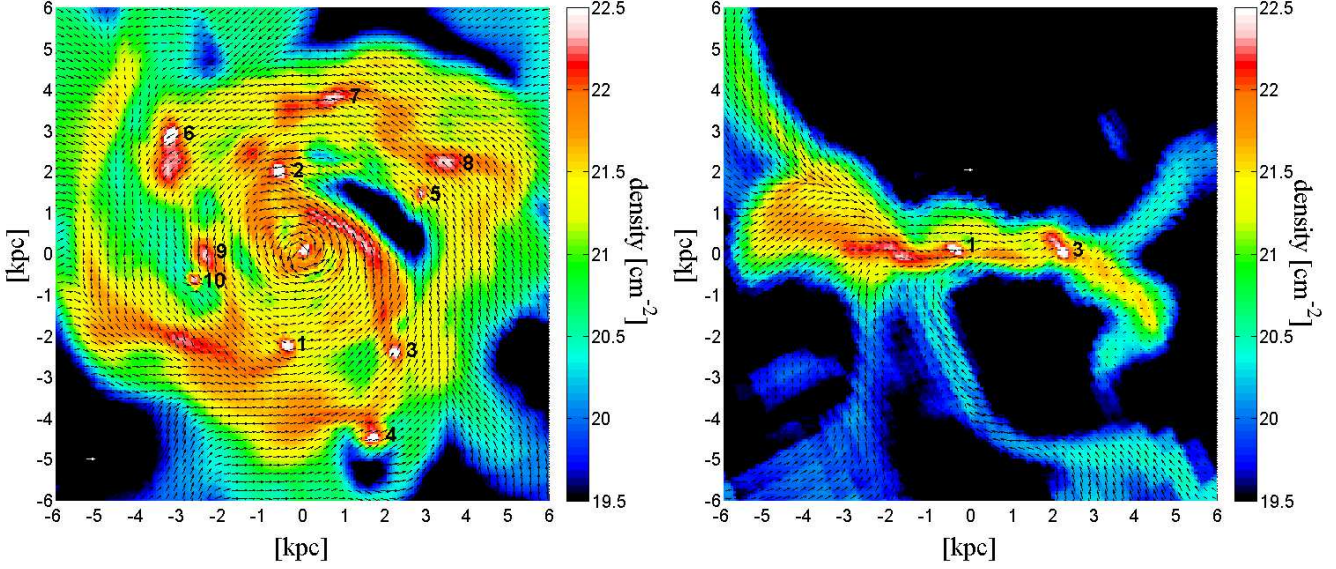


Figure 3. Gas surface density and projected velocity field in the disc of galaxy A at $z = 2.3$, face on and edge on (details similar to Fig. 2). The box encompasses the main body of the gas disc, a radius of ~ 6 kpc. The face-on projection depth is 2 kpc, and the edge-on depth is 1.2 kpc, about clumps 1 and 3. The reference velocity (white arrow) is 200 km s^{-1} . The rotating disc shows a highly-perturbed morphology, with large elongated transient features and ten compact giant clumps marked by numbers (two of which are *ex situ* clumps, §7), see Table C4. The mass of a typical clump is a few percent of the disc mass, and the total mass in clumps is ~ 0.2 of the disc mass. The disc is highly warped locally, sometimes tilting the clumps relative to the global disc plane.

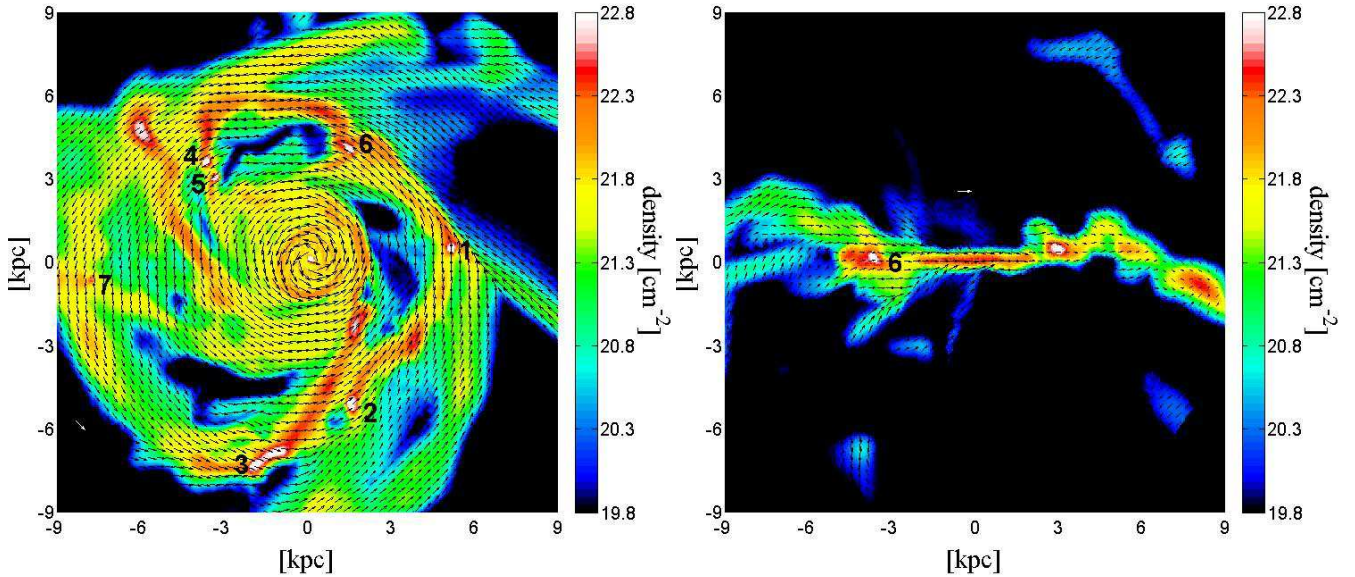


Figure 4. Gas surface density and projected velocity field in the disc of galaxy E at $z = 2.4$, face on and edge on (details as in Fig. 3 and Fig. 2). The box encompasses the main body of the gas disc, which has a radius of ~ 9 kpc, but is asymmetric about the kinematic center. The projection depths are 2 kpc, with the edge-on slice including clump 6 and another perturbation. The white arrow marks a velocity of 500 km s^{-1} . The rotating disc shows a highly-perturbed morphology, with large elongated transient features and seven compact giant clumps marked by numbers (see Table C4). The mass of a typical clump is a few percent of the disk mass, and the total mass in clumps is ~ 0.2 of the disk mass. The disc is highly warped locally, sometimes tilting the clumps relative to the global disc plane.

clump radius $R_c = 455 \text{ pc}$. Its potential well is characterized by $V_{\text{circ}} = 68 \text{ km s}^{-1}$ at $r = 310 \text{ pc}$, the center of the shell in which V_{rot} is computed. The face-on and edge-on views are selected by the total angular momentum vector of the cold gas ($T \leq 10^4 \text{ K}$) in a spherical shell between $0.5R_c$ and R_c .

The surface density and velocity field shown are generated from a cube of side 1.2 kpc centred on the clump centre of mass. The clump is centrally condensed, embedded in an elongated large-scale perturbation (see also Fig. 3) with a relative gas overdensity of ~ 30 compared to the background

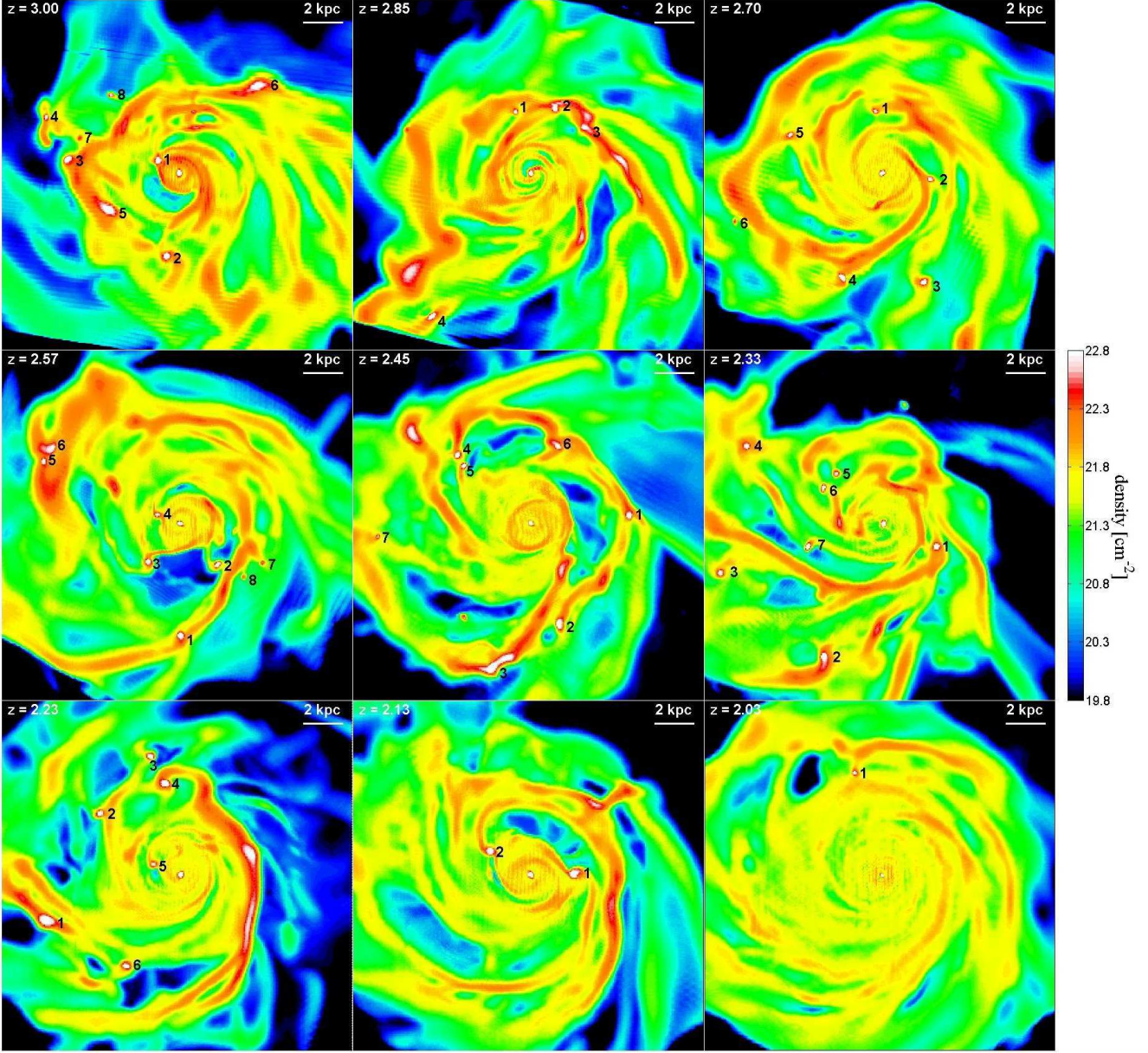


Figure 5. Evolution of gas surface density in the disc of galaxy E from $z = 3$ to $z = 2$. The orientation is face on and the depth is 5 kpc. The box encompasses the main body of the disc, face on in a slice of 18 kpc on the side and 5 kpc depth. The snapshots are equally spaced in expansion factor, $\Delta a = 0.1$, corresponding to $\Delta z \simeq 0.123$. All identified clumps are marked in each panel with a (random) serial number corresponding to Table C4. The disc is large and highly perturbed with many clumps until $z = 1.4$, except near $z = 2$ when it is temporarily featureless.

disc. It has an oblate morphology with an apparent axial ratio of about 2:3. It is important to realize that this clump is only marginally resolved, with ~ 14 cells across its major axis and ~ 9 cells across its minor axis. It therefore shows no substructure (see §5). The resolution effects are more severe along the minor axis, where they may affect the flattening of the clump. We therefore limit our analysis of the density profile to the clump equatorial plane.

The velocity field shown in Fig. 6 is in the rest frame of the clump, and is computed as the mass-weighted average along the line of sight across 0.6 kpc. The face-on view shows systematic rotation from the centre of the clump to about 300 pc, with a velocity of $\sim 60 \text{ km s}^{-1}$. The clump

is thus highly rotation supported with $\mathcal{R} = 0.86$, and with a tilt of $\cos(\text{tilt}) = 0.94$ between the clump spin and the global disc angular momentum. Outside the clump radius we notice bulk motions in different directions, towards the clump and away from it, reflecting the disc rotation as well as the perturbations about it. The apparent infall pattern along the minor axis in the edge-on view involves only $\sim 10\%$ of the clump mass, and it is largely an artifact of the limited resolution along this axis. In fact, most of the clump mass has a rather isotropic velocity dispersion, computed as the standard deviation of each cylindrical component within a given shell.

Figure 7 shows zoom-in views of clump 6 of galaxy

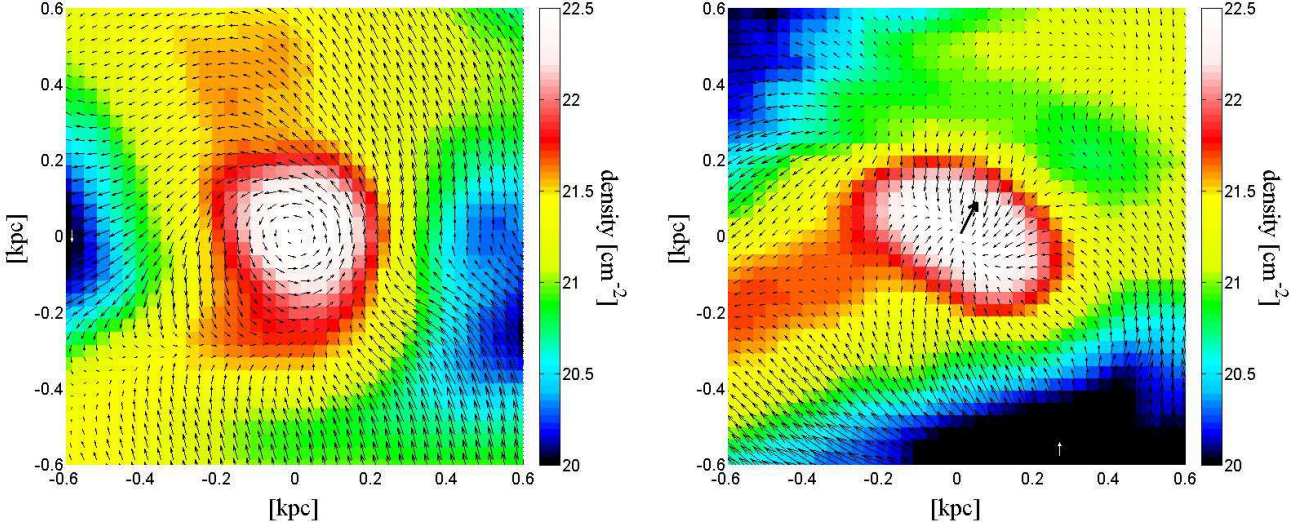


Figure 6. Zoom-in on the gas in clump 1 of galaxy A at $z = 2.3$, face on and edge on in the clump frame. The depth of the slice is 0.6 kpc. The velocity field is as in Fig. 2, with the white arrow denoting 70 km s^{-1} . The clump, of radius $\sim 450 \text{ pc}$, shows systematic rotation of $\sim 63 \text{ km s}^{-1}$ and is highly rotation supported with $\mathcal{R} = 0.86$. The y axis in the edge-on orientation is aligned with the global disc rotation axis, while the thick black arrow marks the clump spin axis. A small tilt of $\sim 20^\circ$ ($\cos(\text{tilt}) = 0.94$) between the clump spin and the global disc angular momentum is evident. The apparent inflow along the minor axis involves only $\sim 10\%$ of the clump mass and is largely an artifact of the marginal resolution along this axis.

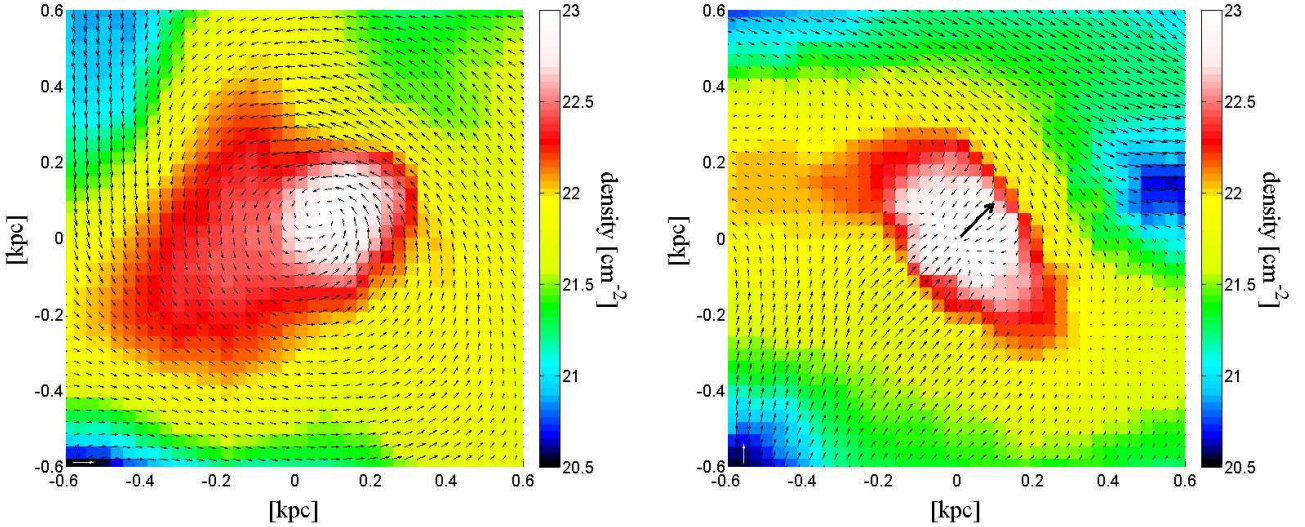


Figure 7. Zoom-in on clump 6 of galaxy E at $z = 2.4$ (more massive than the clump shown in Fig. 6), face on and edge on in the clump frame. The depth of the slice is 0.6 kpc. The velocity field is as in Fig. 2, with the white arrow denoting 200 km s^{-1} . This clump is rotating with $V_{\text{rot}} = 108 \text{ km s}^{-1}$ and is highly rotation supported with $\mathcal{R} \simeq 1$. The y axis in the edge-on orientation is aligned with the global disc rotation axis, while the thick black arrow marks the clump spin axis. The clump spin is tilted compared to the global disc angular momentum, by $\sim 47^\circ$ ($\cos(\text{tilt}) = 0.68$), but it appears to be aligned with the local disc plane.

E at $z = 2.4$, similar to Fig. 6, but more massive, $M_c = 9.6 \times 10^8 M_\odot$ within $R_c = 432 \text{ pc}$. This clump is rotating with $V_{\text{rot}} = 108 \text{ km s}^{-1}$ and it is highly rotation supported with $\mathcal{R} = 0.94$. However, the clump spin is quite tilted with respect to the global disc angular momentum, with a tilt of $\sim 47^\circ$ ($\cos(\text{tilt}) = 0.68$). Despite this, the clump does

appear to be aligned with the local disc plane. This example shows that despite the tendency for prograde rotation and rotation support, the perturbed and warped discs can give rise to highly tilted clumps compared to the global disc.

Figure 8 shows profiles of gas velocity and three-dimensional gas density for six representative high- z clumps

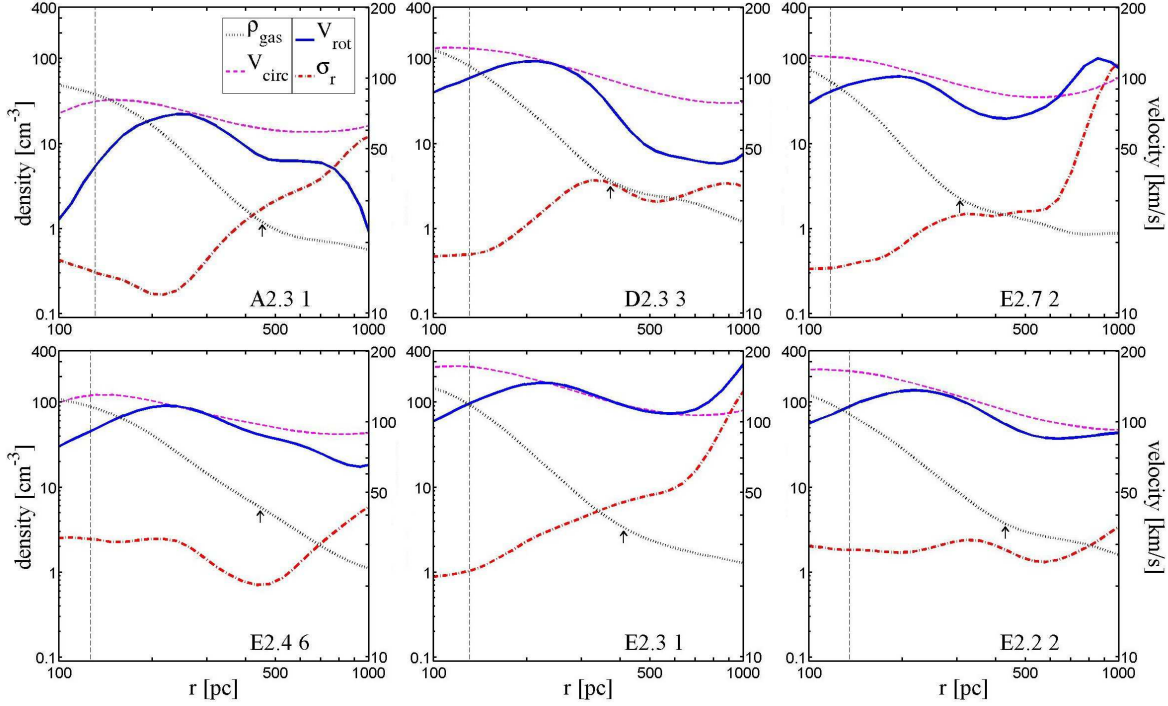


Figure 8. Profiles of the gas in the equatorial plane for a sample of six high- z clumps from the cosmological simulations. Each panel shows the profiles of density (left axis), circular velocity, rotation velocity and radial velocity dispersion (right axis). The clump masses are $(3.9, 8.3, 6.2, 9.6, 13, 12) \times 10^8 M_\odot$. within the clump radii marked by an arrow. The force resolution is marked by a vertical line. The rotation curves rise to a maximum and then decline toward the clump edge, beyond which they are dominated by the disc rotation. All the clumps shown are rotation supported with $\mathcal{R} > 0.8$.

from the cosmological simulations, including the two clumps discussed above. The profiles are averages over rings in the clump equatorial plane. The density profiles crudely resemble the familiar NFW function, namely a local logarithmic slope that steepens with radius from a core of slope flatter than -1 below the resolution scale, through -2 to -3 in the resolved scales, before it flattens again near the clump edge toward a uniform background. The mass-weighted average slope in the clump outside the force resolution scale is close to -2 , implying that for certain purposes the clump profile can be very crudely approximated by the profile commonly associated with an isothermal sphere. As described in §C, we define the clump radius R_c where the local slope becomes flatter than -2 in its approach to a constant at larger radii, or where there appears to be a “shoulder” in the density profile (as in clump 6 from galaxy E at $z = 2.4$). This definition is very similar to the standard definition of subhalo radius as an upturn or inflexion point, generally used in dark-matter halo-finders (see review in Knebe et al. 2011). The background density outside the clump varies from clump to clump and from host disc to host disc, typically in the range $n \sim (2 - 5) \text{ cm}^{-3}$, depending on the large-scale perturbation that the clump is embedded in.

The six clumps have maximum rotation velocities of $(70, 118, 117, 146, 102, 136) \text{ km s}^{-1}$ at $r \sim 200 - 300 \text{ pc}$, and they then decline slowly toward the clump edge and sometimes beyond. The σ_r profiles tend to be rather flat within the clump, with values of $(24, 32, 24, 25, 41, 31) \text{ km s}^{-1}$ near the clump edge. The profiles of the other components of the velocity dispersion

are similar to the σ_r profiles, implying that the velocity dispersion is rather isotropic for most of the clump material. The rotation support parameters are $\mathcal{R} = (0.86, 0.90, 0.83, 0.94, 1.01, 0.88)$, and V_{rot}/σ_r is given by eq. (6). These clumps, like most of the *in situ* giant clumps in the high-redshift discs studied here (§4 below), can indeed be approximated as isotropic rotators mostly supported by rotation, with the pressure that is built up inside the clumps providing the rest of the support against gravitational collapse.

4 STATISTICAL ANALYSIS OF CLUMP SUPPORT

4.1 A sample of clumps

Table C4 presents a sample of 86 disc clumps selected from our simulations for a crude statistical analysis of their properties. The clumps, above a circular-velocity threshold $V_{\text{circ}} > 30 \text{ km s}^{-1}$, were extracted from the five simulated discs, in the redshift range $z \sim 1.9 - 3.0$, from snapshots where they show gravitationally unstable discs with several giant clumps. A separation of $\Delta z \sim 0.2$ between snapshots corresponds at $z \sim 2.5$ to $\sim 220 \text{ Myr}$, which is on the order of the disc orbital time. This is comparable to the lifetime of a clump between formation and end of migration into the central bulge (DSC09, CDB10, Genzel et al. 2011), so each clump is sampled once or maybe twice during its lifetime. In galaxy E, we sample the clumps in snapshots equally spaced in expansion factor $\Delta a = 0.1$, corresponding to $\Delta z \simeq 0.123$, so each clump is sampled more than once during

its lifetime. However, the ~ 130 Myr between snapshots is several times the internal dynamical time in the clump, so it is allowed to evolve considerably between snapshots. While this sample is not strictly a proper statistical sample, we consider it to be a crude approximation for a fair sample spanning the clump properties in clumpy discs of baryonic mass $10^{10} - 2 \times 10^{11} M_{\odot}$, or halo mass $10^{11} - 2 \times 10^{12} M_{\odot}$, in the redshift range 2-3.

In each snapshot the clumps are marked by a random serial number. Table C4 lists for each clump the clump radius R_c , and the baryonic mass M_c within that radius. The gas circular velocity V_{circ} , rotation velocity V_{rot} , radial velocity dispersion σ_r , and the rotation parameter $\mathcal{R} = V_{\text{rot}}^2/V_{\text{circ}}^2$ (eq. (5)) are obtained at the outer half of the clump, as explained in §C. The table then quotes the alignment parameter, defined as the cosine of the tilt angle between the clump spin and the global disc angular momentum. Following is the baryonic surface density in the clump Σ_c , and the contraction factor $c = (\Sigma_c/\Sigma_d)^{1/2}$ (eq. (10)). The relevant disc surface density Σ_d for quantifying a contraction factor is quite uncertain, so the values of c should be taken with a grain of salt. The table also lists the mean stellar age in the clump, the dark-matter fraction and gas fraction within R_c , the position of the clump center in the disc in polar coordinates r and z , and its center-of-mass velocity components V_r , V_z , and V_{ϕ}/V_d , where V_d is the average disc rotation velocity at r . Comments indicate whether the clump is closely interacting with other clumps, whether it has a surface density contrast lower than 3, and whether it is an *ex situ* clump (§7). We also list the progenitor clumps in the preceding snapshot in cases where such progenitors are identified.

Out of the 86 clumps in the sample, 9 (10%) are *ex situ* clumps coinciding with local peaks in the dark matter density and containing an older stellar population, which joined the disc as minor-merging galaxies. We include them in Fig. 9 to Fig. 12, marked by a “x” symbol, but we exclude them from the statistical analysis of the current section, to be addressed separately in §7. The other 77 clumps (90%) were formed *in situ* in the disc and have dark matter fractions comparable to the local background. Out of the 77 *in situ* clumps, 11 clumps (14%) are tagged as closely interacting with other clumps or as remnants of recent binary mergers of clumps. We include these in our analysis, but distinguish them in Fig. 9 to Fig. 12 by open circles. Out of the 77 *in situ* clumps, 12 (16%) seem to have a surface-density contrast below 3, and are marked low-contrast clumps. We include these in our analysis, but distinguish them in Fig. 9 to Fig. 12 by “+” symbols. Some of their properties are less certain. All other *in situ* clumps are marked by filled circles.

4.2 Rotation support

Figure 9 shows the distribution of the rotation parameter \mathcal{R} versus V_{circ} for the cosmological disc clumps. The median value for the *in situ* clumps is found to be $\mathcal{R} \simeq 0.78$, saying that the support in most of the clumps is heavily dominated by rotation. In 82% of the clumps $\mathcal{R} > 0.5$, i.e. the rotation provides most of the support. The massive *in situ* clumps, 17 clumps with $V_{\text{circ}} \geq 100 \text{ km s}^{-1}$, have $\mathcal{R} > 0.75$ (except of one clump of $\mathcal{R} = 0.7$ associated with a merger), namely

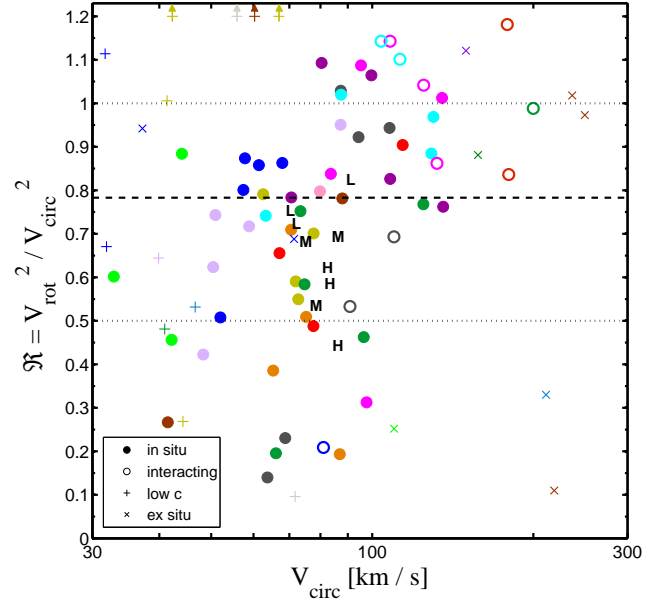


Figure 9. Rotation parameter, $\mathcal{R} = V_{\text{rot}}^2/V_{\text{circ}}^2$, as a function of clump circular velocity, V_{circ} , for the sample of disc clumps (Table C4). The clumps are extracted from the cosmological simulations of clumpy disc galaxies of baryonic mass $10^{10} - 2 \times 10^{11} M_{\odot}$ in the redshift range 1.9 – 3.0. The colors of the symbols mark the relevant galaxy and snapshot as labeled in Fig. 11. Normal *in situ* clumps are marked by filled circles. In-situ clumps that are closely interacting or are remnants of a recent merger are marked by open symbols. Clumps with a surface-density contrast lower than 3 are marked by a “+”. Ex-situ clumps that contain dark-matter are marked by a “x”, but are not included in the current analysis. The median of $\mathcal{R} = 0.78$ is denoted by a dashed horizontal line. We see that the majority of the clumps are supported mainly by rotation. Shown in comparison (marked “L”, “M” and “H”) are the clumps extracted from isolated galaxy simulations (§5) at different resolutions of 70 pc (LR), 12 pc (MR), and 2 pc (HR). At the highest resolution, \mathcal{R} is reduced by $\sim 30\%$, but the rotation still provides a significant fraction of the clump support.

less than 6% have $\mathcal{R} < 0.7$. The less massive clumps show a tail of intermediate and low rotation support down to $\mathcal{R} \sim 0.1$. The clumps that are associated with clump interactions or clump mergers tend to have the highest V_{circ} and be highly supported by rotation.

Figure 9 also shows the clumps extracted from simulations of isolated discs with different resolutions, described in §5 below. The three clumps simulated with a resolution similar to the resolution in the cosmological runs (LR) show rotation parameter values similar to the cosmological simulations, $\mathcal{R} = 0.72 - 0.82$. The three clumps simulated with a much higher resolution of 2 pc (HR), exhibit lower rotation parameters, $\mathcal{R} = 0.44 - 0.62$. While the higher resolution results in a reduction of $\sim 30\%$ in \mathcal{R} , the rotation still tends to be a major player in the support of the highly resolved clumps.

One should note that the measured rotation parameter depends on the actual radius within the clump where it is obtained. We have tried modifications of the algorithm described in §C, including measuring \mathcal{R} at the maximum of the rotation curve or at the clump edge, and found no qualitative change in the result. The typical variation in \mathcal{R} is limited to $\sim 15\%$, reaching $\sim 30\%$ in exceptional

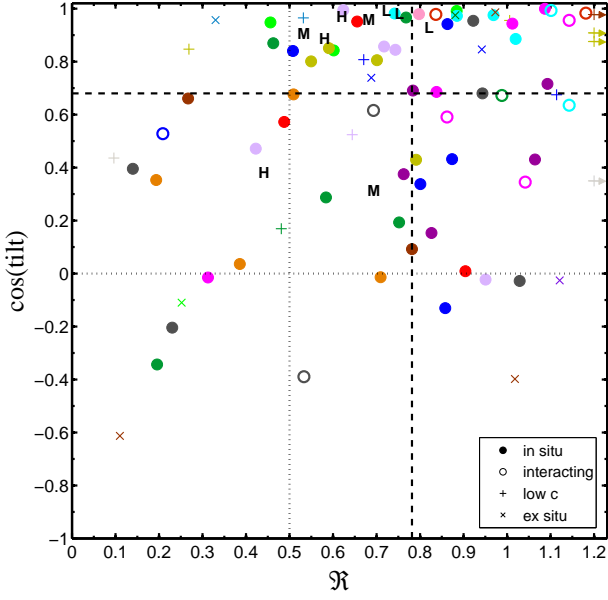


Figure 10. The alignment of clump and disc angular momentum, $\cos(\text{tilt})$, versus rotation parameter \mathcal{R} . The symbols are as in Fig. 9. The medians of $\cos(\text{tilt}) = 0.68$ and $\mathcal{R} = 0.78$ are marked by dashed lines. The average in the case of a random tilt is $\cos(\text{tilt}) = 0$. There is a general tendency for prograde clump rotation, but large tilts occur rather often, and 10% of the *in situ* clumps actually rotate in a retrograde sense, with $\cos(\text{tilt}) < 0$. There is no significant correlation between the tilt and \mathcal{R} . There is a marginal tendency for the more massive clumps to be more aligned with their host discs (not shown). The clumps of the isolated galaxy simulations tend to be more aligned with their discs, but there are also tilted cases.

cases where the measurement is contaminated by nearby perturbations in the disc. The choice of obtaining \mathcal{R} as the average in the outer half of the clump turned out to be a sensible compromise.

In 13 of the *in situ* clumps, the measured rotation parameter is apparently slightly above unity, $1.0 < \mathcal{R} < 1.2$, namely an excess of 10% or less for V_{rot} over V_{circ} . This could reflect small deviations from pure rotation or from spherical symmetry at the radius where these quantities are measured, and they are within the expected scatter of the mean. We therefore do not interpret these deviations as indicating departures from Jeans equilibrium, and adopt $\mathcal{R} = 1$ for these clumps. Four of the low contrast, low mass, clumps have very high values of $1.5 < \mathcal{R} < 2.5$, marked in Figure 9 as “+” symbols with upward pointing arrows. These clumps appear to be unbound, at least at the large radii adopted for these clumps. We also note that these small clumps are rather poorly resolved and the statistical “measurement” error for them is large.

4.3 Tilt relative to the disc

In the analytic model outlined in §2, the disc is assumed to be rotating uniformly and the clumps are predicted to end up in prograde rotation with their spins and minor axes aligned with the disc axis. However, the high-redshift discs in our cosmological simulations are highly perturbed, with the local “plane” sometimes deviating from the global disc plane (as defined either by inertia or by angular momentum),

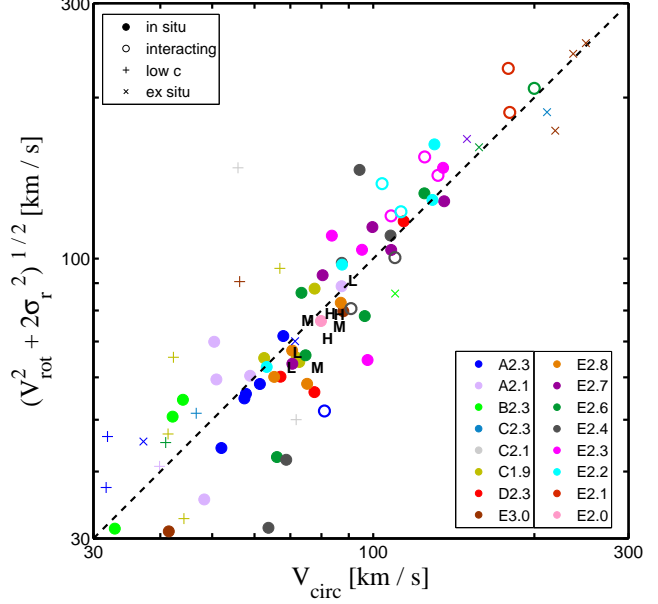


Figure 11. Validity of Jeans equilibrium. The square root of the two sides of eq. (4), $(V_{\text{rot}}^2 + 2\sigma_r^2)^{1/2}$ versus V_{circ} , representing support versus gravity. The symbols are as in Fig. 9. The clumps roughly obey the Jeans equation for an isotropic, isothermal rotator (dashed line). The outliers downwards tend to have a low mass and low \mathcal{R} (not shown). These clumps come closer to the line when the factor 2 multiplying σ^2 in the support term is replaced by a larger factor. The low-contrast clumps tend to lie above the line due to their high velocity dispersions.

as can be seen in the edge-on slices in Fig. 3 and Fig. 4. One may therefore expect some of the clump minor axes to be tilted relative to the global disc minor axis, possibly following their local disc neighborhood (Figure 7).

Figure 10 shows the distribution of the alignment cosine $\cos(\text{tilt})$ versus \mathcal{R} for our sample of clumps. The median is at $\cos(\text{tilt}) = 0.68$, corresponding to a tilt of $\sim 47^\circ$. There is a tail of large tilts extending to $\cos(\text{tilt}) \sim 0$, and 10% of the clumps actually rotate in a retrograde sense, $\cos(\text{tilt}) < 0$. We conclude that the expected tendency for prograde rotation is clearly there, but the occurrence of significant tilts is not infrequent. There is no significant correlation between the tilt and \mathcal{R} . There is a marginal tendency for the more massive clumps, especially the ones associated with merging clumps, to be more aligned with the global disc plane (not shown). For example, there are no retrograde clumps among the *in situ* clumps with $V_{\text{circ}} > 100 \text{ km s}^{-1}$. It is yet to be investigated whether the tilts were generated by the perturbed velocity field at the time of clump formation or by torques from the perturbed environment during the later stages of clump evolution.

The clumps of the isolated galaxy simulations tend to be more aligned with their host discs than the cosmological clumps, as expected, with a median at $\cos(\text{tilt}) = 0.93$, and no retrograde clumps. However, two of these clumps have significant tilts, $\cos(\text{tilt}) \sim 0.3 - 0.4$. There is no obvious dependence on resolution.

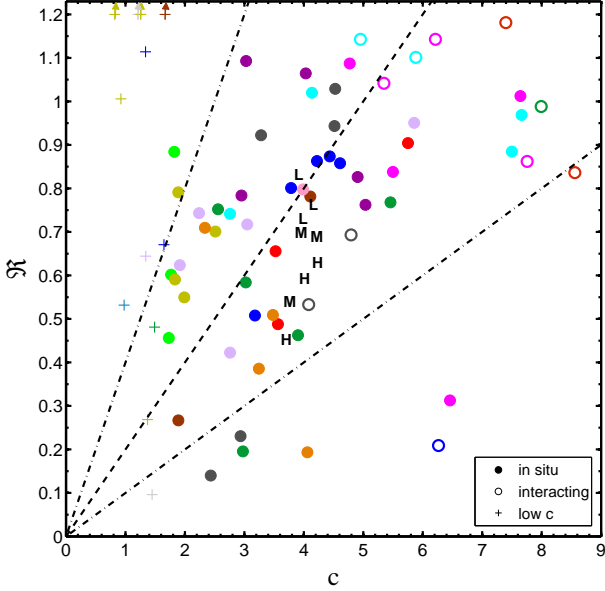


Figure 12. Rotation parameter \mathcal{R} versus contraction factor c . The toy-model prediction assuming conservation of angular momentum, eq. (20), is marked by a dashed line. The symbols are as in Fig. 9. Except for 10% outliers, the clumps lie within a factor two from the model prediction (dash-dotted lines).

4.4 Jeans equilibrium

We wish to find out to what extent the simulated clumps obey the Jeans equation for an isotropic rotator, eq. (4). We find the internal velocity dispersion to be close to isotropic, and the density profile to be not far from that of an isothermal sphere (§3.3), so we expect eq. (4) to be approximately valid for a clump in equilibrium. For this purpose, Fig. 11 compares the square-roots of the two sides of eq. (4), $(V_{\text{rot}}^2 + 2\sigma_r^2)^{1/2}$ versus V_{circ} . We find that most clumps lie close to the line that marks Jeans equilibrium, with a few outliers that correlate with low mass and low \mathcal{R} (not shown). The fit would improve for the clumps with a low \mathcal{R} once the factor 2 in eq. (4) is replaced by 3 or even a higher factor, to take into account the deviation of the clump from an isothermal sphere profile, with a somewhat steeper density profile, as seen in Fig. 8. The low-contrast clumps tend to lie above the line due to their high internal velocity dispersions, indicating that some of them may be transients not in Jeans equilibrium. The clumps of the isolated galaxy simulations roughly obey the Jeans equation, independent of resolution. We see a tendency of the other less massive clumps to show larger deviations from Jeans equilibrium, be less rotationally supported, and contain a younger stellar population (§8 below), indicating that they may be still collapsing toward equilibrium.

4.5 Rotation versus contraction factor

A comparison of the rotation support parameter \mathcal{R} and the contraction factor c could allow us in principle to test the validity of the simple model prediction spelled out in eq. (20), $\mathcal{R} \sim 0.2c$. To the extent that the toy model of §2 is a viable approximation, this will be a measure of the degree

Table 1. Resolution and physical parameters for the high-resolution idealized simulations

Resolution	ϵ_{AMR} (pc)	m_{res} (M_{\odot})	n_{SF} (cm^{-3})	η_{SN}
HR	1.7 pc	2×10^3	5×10^4	50%
MR	10.2 pc	2×10^3	4×10^3	50%
LR	68 pc	2×10^4	8×10^2	50%

of conservation of internal angular momentum during the clump formation and evolution. Figure 12 shows \mathcal{R} versus c . Except for 10% outliers with low \mathcal{R} , the bound clumps lie within a factor of two from the toy-model prediction, and they are spread both above and below the predicted line. This indicates that, on average, the toy model is a viable crude approximation and, on average, angular momentum is roughly conserved. The big scatter, which partly reflects uncertainties in measuring \mathcal{R} and especially c , may imply that some clumps do reach high values of contraction factor that may indicate certain angular-momentum loss. This is especially true for the clumps associated with interactions or mergers, and in general for the most massive clumps with $V_{\text{rot}} > 100 \text{ km s}^{-1}$. There is a correlation between angular-momentum loss and low \mathcal{R} . Most of the low- c clumps are outliers toward a low contraction factor and high rotation, either because they gained angular momentum, or because they are unbound transients (Fig. 11). The clumps from the isolated-galaxy simulations are also in general agreement with eq. (20), with a contraction factor ~ 4 . At the highest resolution, they indicate an angular-momentum loss of about 30%.

5 ISOLATED GALAXIES WITH HIGHER RESOLUTION

The simulations start with a pre-formed exponential disc of half gas and half stars, and a stellar mass of $\sim 1.5 \times 10^{10} M_{\odot}$, embedded in a dark-matter halo. More details are provided in §B. These simulations rapidly evolve into turbulent discs with giant clumps of gas and young stars. The clumpy morphology, the clump formation rate, their mass, number, and migration to the disc centre, are similar to the behavior in the idealized simulations of BEE07 and in the cosmological simulations analyzed above (see CDB10).

In the cosmological simulations analyzed in the previous sections, where the maximum grid resolution is between 35 and 70 pc, the high-redshift giant clumps are only marginally resolved, with the collapsed clump diameter ranging from 6 to 30 grid cells. We should address the possible effects of this marginal resolution on our conclusions concerning the rotational support of the clumps. When the resolution is better, the clumps are expected to develop a rich turbulent substructure including fragmentation to subclumps (see Fig. 14 below). By not including this substructure, the limited resolution may introduce a bias in the rotation support of the clump in several different ways. First, if massive fragmentation happens early in the clump collapse, the collapse might involve less dissipation, because of the potential small cross-section of the sub-clumps. If the clumps are less dissipative, the contraction factor may become smaller, and the clumps could end up with less rotation support

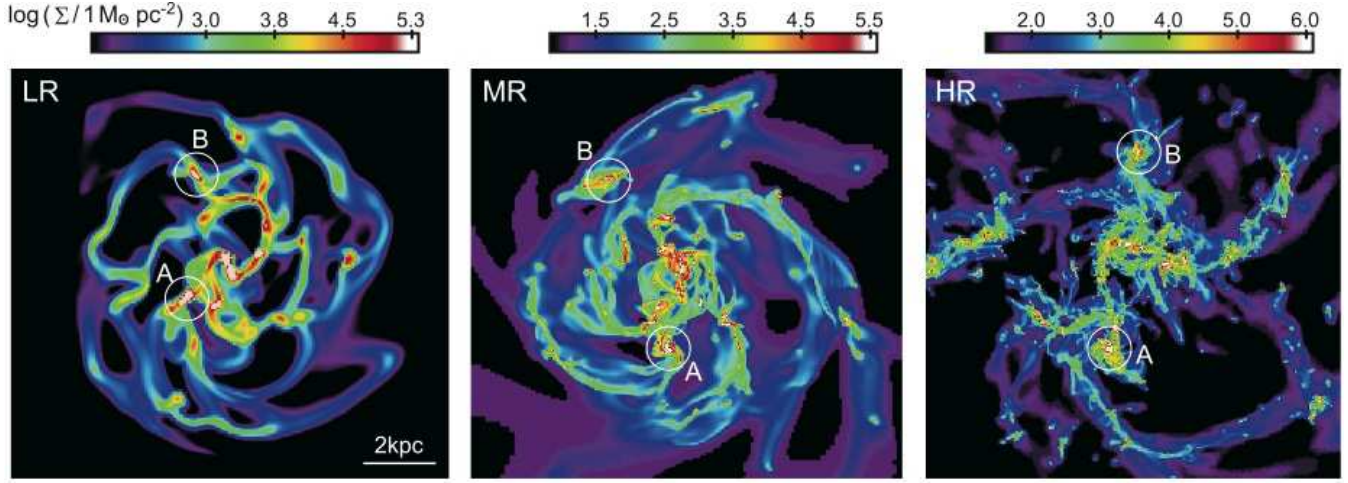


Figure 13. Face-on views of the gas surface density in the simulations of an idealized isolated galaxy with different maximum resolutions of 68 (LR), 10 (MR), and 1.7 pc (HR). This snapshot is when the outer disc has completed two rotations. There is no one-to-one correspondence between the giant clumps at various resolutions, because the initial small-scale fluctuations and noise vary with resolution. Clumps A and B were chosen on the basis of their similar masses and distances from the disc centre. Clump C was picked from a later output.

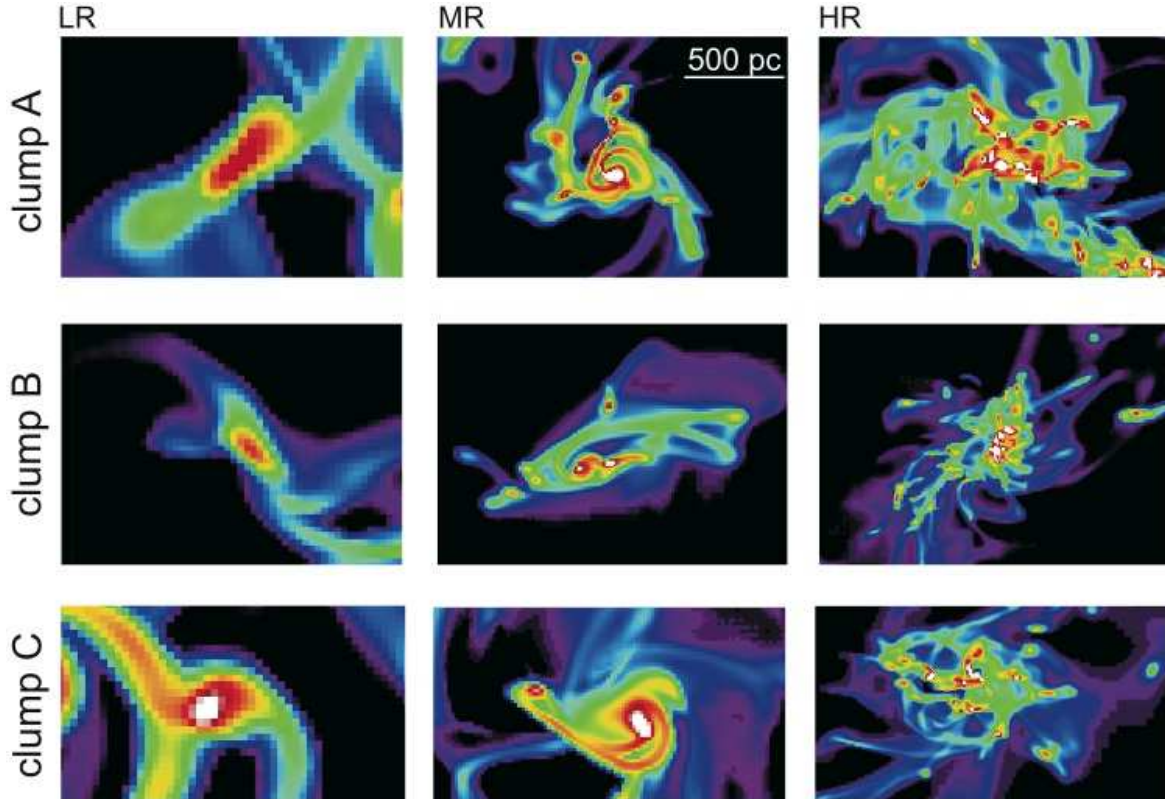


Figure 14. Zoom-in views of clumps A, B and C from the isolated-galaxy simulations at the different resolution levels, LR, MR, and HR. The orientation is face on with respect to the global disc. The morphological appearance of the clumps varies with resolution. The LR clumps resemble inflection knots along broad density waves, with a smooth body and a weak spiral pattern in their outer regions. The MR clumps are mini spiral discs, suggesting local rotation. The HR clumps have substructure with dense subclumps. Internal shocks suggest supersonic turbulent motions, but the global spin of the giant clumps in HR is only $\sim 30\%$ lower than in LR.

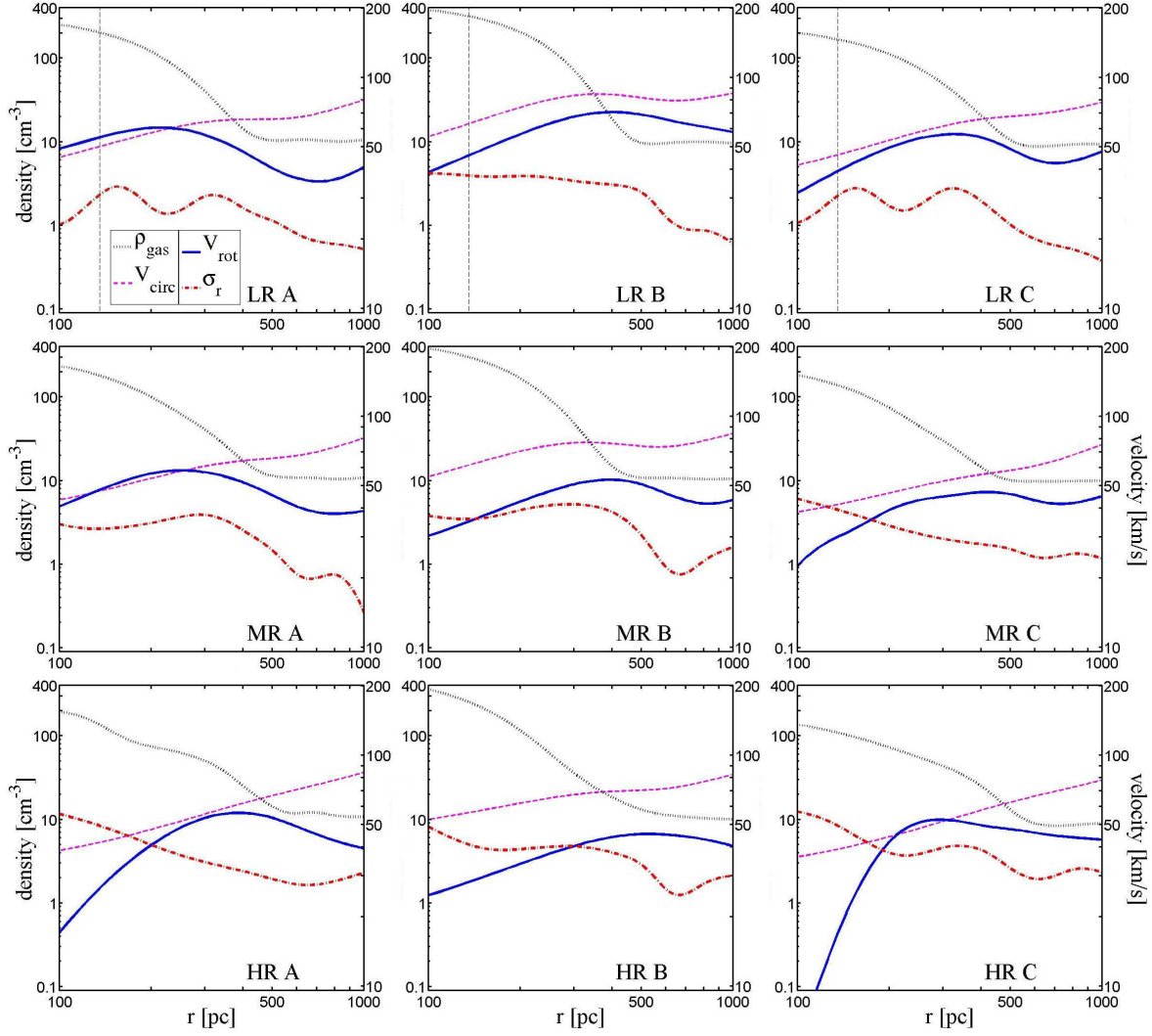


Figure 15. Profiles of the gas in the equatorial plane for three clumps from each of the high- z isolated-galaxy simulations LR, MR, and HR (from top to bottom), with maximum resolution of 68, 10, and 1.7 pc. Each panel shows the profiles of density (left axis), rotation velocity and radial velocity dispersion (right axis). The profiles are smoothed as described in Appendix §C. The LR clump profiles are similar to those of the cosmological clumps when scaled by mass (Fig. 8). While V/σ is decreasing with improving resolution, the clumps remain rotation supported in their outer parts even in the HR case.

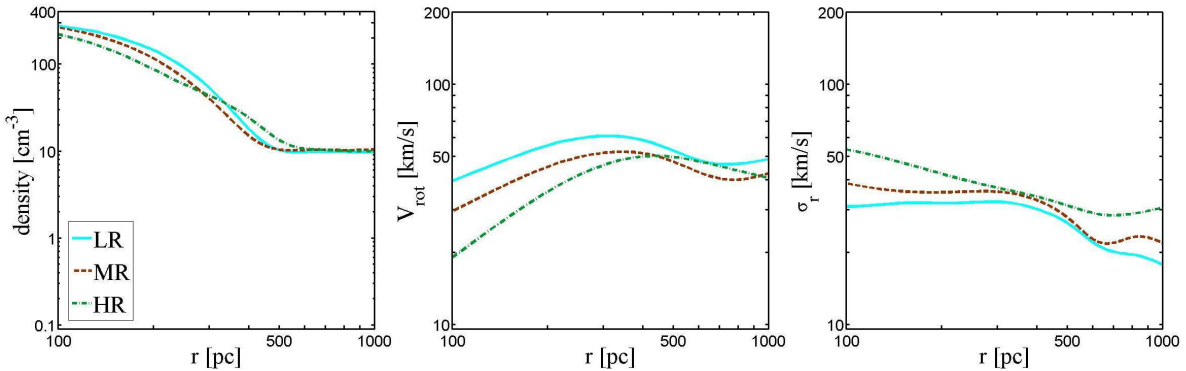


Figure 16. Average profiles over the three clumps shown in Fig. 15 for the three resolution levels, LR, MR, HR. The rotation velocity in HR is on average $\sim 20\%$ lower than in LR, and the velocity dispersion is correspondingly $\sim 20\%$ higher.

(eq. (20)). The kinetic energy of the subclump motions within the clump may add to the pressure support of the giant clump. Second, the limited resolution could introduce a bias of an opposite sign, toward less rotation support, by preventing the (small) clumps from contracting to below a size of a few resolution elements. Third, the limited resolution may cause an error in the torques acting on the clump and thus in the angular-momentum exchange between clumps and disc, which could be of either sign. For example, numerical viscosity may lead to reduced torques and angular-momentum losses. The potential artifacts of numerical viscosity might be non-negligible and hard to estimate, but they should be smaller at higher resolution. Fourth, the level of rotation versus dispersion support may depend on the turbulence within the clumps, which becomes fully developed only when the resolution is sufficiently high.

To investigate the effects of numerical resolution and small-scale substructure, we use simulations of idealized, isolated, gas-rich disc galaxies representative of $z \sim 2$ star-forming galaxies. The absence of continuous cosmological gas supply limits the duration of disc evolution that can be followed, but it permits a much higher resolution than the cosmological simulations. Overall, the initial conditions and evolution into high- z , clumpy discs are as described in Bournaud et al. (2007, BEE07), but the current simulations were performed with much better resolution using the AMR code RAMSES (Teyssier 2002), comparable in many ways to the ART code used in the cosmological simulations utilized in the previous sections. The sub-grid physical recipes include cooling using a barotropic equation of state down to ~ 100 K, star formation and supernova feedback. More details of the RAMSES simulation technique and the sub-grid physical recipes are provided in an appendix, §B, as well as in Bournaud et al. (2010); Teyssier et al. (2010).

We performed three simulations of a system that represents a massive disc at $z \sim 1 - 3$, at a high resolution (HR), medium resolution (MR) and low resolution (LR), as listed in Table 1. The resolution in the LR simulation is similar to the resolution in the cosmological simulations, with slightly lower spatial resolution but somewhat higher mass resolution. The HR simulation resolves gas densities up to 10^7 cm^{-3} and sizes of a few parsecs, comparable to today’s molecular clouds. The resulting density power spectrum for the HR model (Bournaud et al. 2010, section 3.4 and Figure 15) is characteristic of a fully developed three-dimensional turbulence cascade, implying that the HR resolution is sufficient for convergence on the internal properties of kpc-size clumps.

Figure 13 shows the global disc morphology in gas for the three resolution levels. The discs are shown after two rotations of the outer disc, when a clumpy turbulent steady state has been reached, with a constant turbulent speed. We compare three clumps simulated at the three resolution levels. Unfortunately, there is no strict one-to-one correspondence between the clumps in the three resolution levels, because the small scale initial fluctuations that seeded the instabilities were naturally different. We therefore picked from the most massive clumps three that are located at similar distances from the galaxy centre, all with masses of a few $10^8 M_\odot$, as estimated in a circular aperture of radius ~ 500 pc. Two of the clumps, labeled A and B, are shown in

Fig. 13, and a third clump, labeled C, is selected on the same basis from a later output of the three simulations. Zoom-in views of the three clumps at the three resolution levels are shown in Fig. 14.

The morphology of the giant clumps shows substantial variations with resolution. The LR clumps have a smooth ellipsoidal main body, with elongated extensions in the outer parts, somewhat resembling inflection knots along spiral density waves where the vorticity is at a maximum. The MR clumps show a mini-spiral morphology, suggesting internal clump rotation. The spin axis in clumps A and C is aligned with the disc axis, while clump B is significantly tilted. The HR clumps show a rich substructure with many dense sub-clumps. At this resolution, the internal supersonic turbulence (velocity dispersion $\sim 50 \text{ km s}^{-1}$, gas sound speed $\lesssim 5 \text{ km s}^{-1}$) is properly resolved, as indicated by the power spectrum analysis. The turbulent flows generate dense filaments that give rise to even denser sub-clumps. The outer spiral armlets suggest significant clump rotation.

We analyze the kinematic properties of the clumps in each resolution level following a procedure similar to the analysis of the cosmological simulations. The density, velocity and velocity dispersion profiles of the three clumps at the different resolution levels are shown in Fig. 15, and the average profiles over the three clumps are shown in Fig. 16. Rather surprisingly, the density profiles show only a weak systematic variation with the resolution level — no significant change at $r < 100$ pc and at $r > 250$ pc, and an apparent increase of less than 50% in the average density at $r \sim 100 - 200$ pc between HR and LR, which may be insignificant given the small-number statistics. The global kinematics inside the clumps shows only a marginal variation between the HR and MR levels, despite the order-of-magnitude change in resolution. However, comparing HR with LR we see a systematic trend. For example, the average clump rotation curve is $\sim 20\%$ higher in the LR case, and the associated velocity dispersion level is $\sim 20\%$ lower in LR compared to HR. Thus, the 70 pc resolution is responsible for a $\sim 20\%$ overestimate of the rotation velocity and a corresponding underestimate of the velocity dispersion. Combined with the small variation in the density profile, this translates to a $\sim 30\%$ overestimate in the average rotation parameter \mathcal{R} , from $\mathcal{R} = 0.57$ to 0.76. It seems that the main drivers of lower rotation and higher dispersion in the HR case are the reduced dissipation due to substructure, and the enhanced pressure due to resolved internal turbulence. In the HR clumps, some rotational energy is transferred to random motions, as a result of tidal stirring of the subclumps.

The contraction factor is rather insensitive to the resolution, at the level of $c \sim 4$ for all clumps. According to the toy model, eq. (20), this level of contraction roughly corresponds to a rotation parameter of $\mathcal{R} \sim 0.8$ if there is no angular-momentum exchange between clump and disc. This is indeed the case for the median clumps in the cosmological simulations and the clumps in the isolated discs simulated with a similar resolution, LR. The clumps simulated with higher resolution, HR, with an average $\mathcal{R} \sim 0.57$, have lost on average $\sim 30\%$ of their angular momentum. This may be due to torques associated with the clump substructure. We find no variation in the clump size or angular momentum in the direction expected for numerical viscosity. If anything

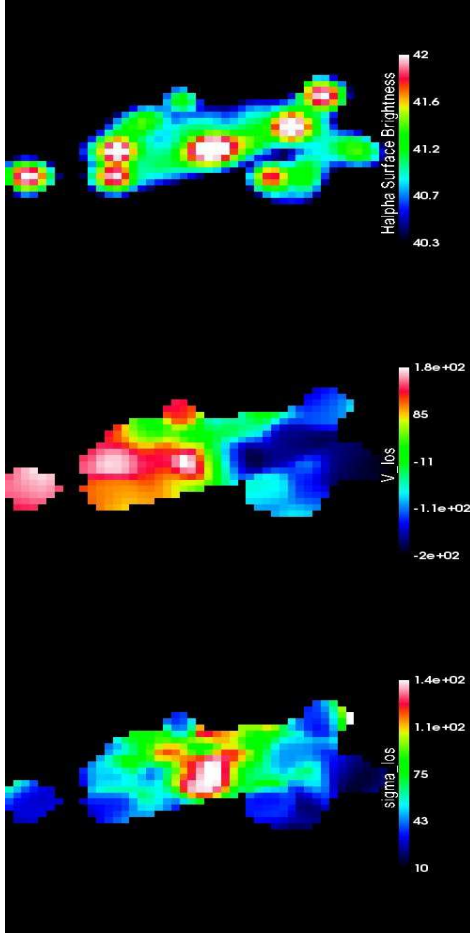


Figure 17. Galaxy A at $z = 2.3$ “observed” in $H\alpha$ at 70° inclination, with the major axis horizontal. Top: $H\alpha$ surface brightness ($\text{erg s}^{-1} \text{ kpc}^{-2}$). Middle: line-of-sight mean velocity (km s^{-1}). Bottom: line-of-sight velocity dispersion (km s^{-1}). The velocities are weighted by $H\alpha$ emissivity. The box size is 10 kpc and the pixel size is 200 pc. All maps are convolved with a Gaussian filter of $\text{FWHM} = 0.5 \text{ kpc}$, corresponding to $\sim 0.06 \text{ arcsec}$. The irregular $H\alpha$ morphology dominated by giant clumps has only little effect on the kinematics, which is dominated by a regular pattern of a rotating disc with a central bulge of high velocity dispersion.

we see small variations in the opposite sense, indicating that the behavior may be driven by physical torquing and dissipation in shocks rather than by numerical viscosity, even at LR and equivalently in the cosmological simulations.

We report in §9 that simulations similar to those described here but with a lower gas fraction that resembles low- z galaxies produce smaller clumps that are not supported by rotation.

6 OBSERVABLE SIGNATURE OF ROTATING CLUMPS

We have learned that the internal kinematics of most giant clumps in our simulated galaxies at $z \sim 2$ is dominated by rotation, with rotation velocities that could be as high as 120 km s^{-1} or more in the biggest clumps, and with a median rotation-support parameter of $\mathcal{R} = 0.78$. One might have assumed that this rotation signal should be detectable. On the other hand, the internal velocity dispersion is not

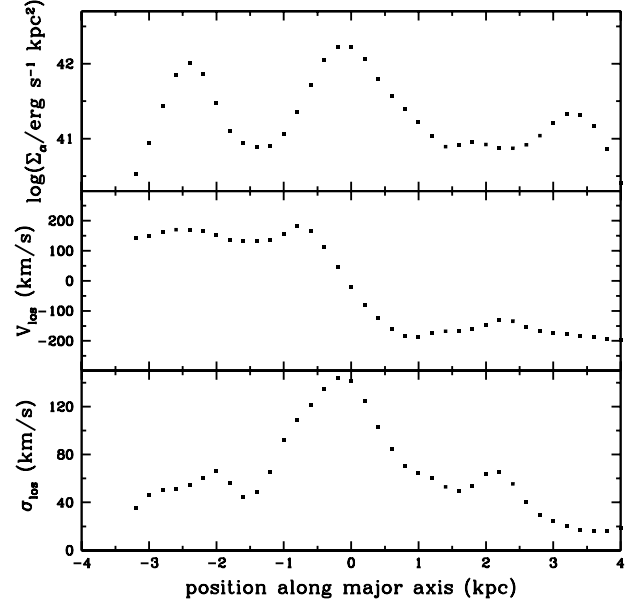


Figure 18. Simulated long-slit “observations” along the major axis of the Galaxy A disc at $z = 2.3$. Top: $H\alpha$ surface brightness. Middle: line-of-sight mean velocity. Bottom: line-of-sight velocity dispersion. After correcting for inclination and beam smearing, the rotation curve is rather flat at a level of 180 km s^{-1} , and the intrinsic central velocity dispersion is $\sim 90 \text{ km s}^{-1}$.

very different from that of the surrounding disc, and is therefore expected to be hardly noticeable. Here we make a quick attempt to learn about the potential observability of the clump rotation signal. We refer in particular to observations in $H\alpha$, tracing the ionized gas in the star-forming regions, which highlight the giant clumps. With a clump diameter $\lesssim 1 \text{ kpc}$, the main observational obstacle is the beam smearing, which is currently at the level of $\text{FWHM} \sim 0.2 \text{ arcsec}$ (Genzel et al. 2011), corresponding to $\sim 1.6 \text{ kpc}$. Other effects that may reduce the rotation signal are (a) contamination by foreground and background gas in the perturbed disc, that may have high velocities driven by supernova feedback, and (b) the unknown inclination of the clump spin axis relative to the line of sight due to the common tilts of the clumps with respect to the disc. In this preliminary study we perform mock observations of the 2D kinematics of a few disc clumps in our simulated galaxies, exploring different levels of beam smearing.

6.1 $H\alpha$ kinematics in the disc

In order to generate mock $H\alpha$ observations, we first compute the star formation rate density, ρ_{SFR} , using the distribution of stellar particles younger than 10 Myr. Then, we use standard conversion factors to compute the $H\alpha$ emissivity $\epsilon_{H\alpha}$, based on the Kennicutt (1998) conversion and adjusted to a Chabrier (2003) IMF,

$$\log \epsilon_{H\alpha} = \log \rho_{\text{SFR}} + 41.33, \quad (23)$$

where $\epsilon_{H\alpha}$ is in $\text{erg s}^{-1} \text{ kpc}^{-3}$ and ρ_{SFR} is in $M_\odot \text{ yr}^{-1} \text{ kpc}^{-3}$. This equation holds as long as the $H\alpha$ emissivity traces the underlying star-formation law, which is

the case on scales of a few hundred parsecs (Kennicutt et al. 2007). The $H\alpha$ surface brightness is obtained by projecting the emissivity along a line-of-sight (los), \mathbf{n} , characterized by an inclination angle i with respect to the galaxy rotation axis (variations in the surface brightness due to variations of dust opacity are not included).

We then convolve it with a Gaussian filter, h_G , of a given FWHM,

$$S_{H\alpha} = \left(\int \epsilon_{H\alpha} dl \right) * h_G. \quad (24)$$

We compute the mean velocity along the line-of-sight, weighted by the $H\alpha$ emissivity, and convolve it with the same Gaussian,

$$\bar{v}_{\text{los}}(x, y) = \frac{1}{S_{H\alpha}} \left[\left(\int \epsilon_{H\alpha} \mathbf{v} \cdot \mathbf{n} dl \right) * h_G \right], \quad (25)$$

where the integrals are along the line-of-sight \mathbf{n} through the point (x, y) . The line-of-sight velocity dispersion is computed via,

$$\sigma_{\text{los}}^2(x, y) = \overline{v_{\text{los}}^2}(x, y) - \bar{v}_{\text{los}}^2(x, y). \quad (26)$$

where, $\overline{v_{\text{los}}^2}$ is the $H\alpha$ -weighted variance of the velocity along the line-of-sight, convolved with the Gaussian filter,

$$\overline{v_{\text{los}}^2}(x, y) = \frac{1}{S_{H\alpha}} \left[\left(\int \epsilon_{H\alpha} (\mathbf{v} \cdot \mathbf{n})^2 dl \right) * h_G \right]. \quad (27)$$

Figure 17 shows $H\alpha$ maps of galaxy A at $z = 2.3$, observed at an inclination $i = 70^\circ$. This inclination, with $\sin i \simeq 0.94$, is close enough to edge-on for capturing most of the rotation signal, but inclined enough to make all the giant clumps visible individually. The figure shows the $H\alpha$ surface brightness, $S_{H\alpha}$, the line-of-sight mean velocity, \bar{v}_{los} , and the line-of-sight velocity dispersion, σ_{los} . We imposed a threshold in star formation surface density, $\Sigma_{\text{SFR}} > 0.1 M_\odot \text{ yr}^{-1} \text{ kpc}^{-2}$ or $\log S_{H\alpha} > 40.33$, a pixel size of 0.2 kpc, and a Gaussian smoothing with FWHM = 0.5 kpc, corresponding to ~ 0.06 arcsec at $z \sim 2$.

The $H\alpha$ density image shows an extended, near edge on, thick and highly perturbed disc. The $H\alpha$ luminosity highlights the central bulge and several large clumps of ~ 1 kpc in size. The clumps account for about half the total star formation rate in the galaxy. In spite of this irregular clumpy morphology, the kinematics is dominated by a systematic pattern of a rotating disc with $V_{\text{rot, max}} \simeq 180 \text{ km s}^{-1}$. This overall rotation pattern is disturbed and shows non-axisymmetric features that reflect significant local non-circular motions, which could be driven by the incoming streams or by the disc instability itself. For example, the clump with a high positive velocity near the positive minor axis is an off-disc satellite in an orbit not related to the disc rotation. However, in general, one sees no obvious correlation between the kinematic features and the giant clumps as observed in the surface-brightness map. The velocity dispersion is dominated by the bulge with a global fall off as a function of radius, and the clumps are not associated with significant peaks in velocity dispersion — if anything, some of them are associated with local minima.

Figure 18 shows a simulated long-slit “observation” of V_{los} and σ_{los} along the major axis of the disc shown in Fig. 17. The surface brightness shows the large star-forming

region at the central bulge and two clumps that lie along the major axis. Overall, the $H\alpha$ surface brightness does not decrease with radius, with the inter-clump medium at roughly a constant level of $H\alpha$ surface brightness out to the disc edge. The line-of-sight velocity along the major axis shows a roughly flat rotation curve of $V_{\text{rot}} \simeq V_{\text{los}} / \sin i = 180 \text{ km s}^{-1}$, outside the central 1-kpc region. The beam smearing has only a 10% effect on the value of the maximum disc rotation velocity. Inside that region, the rotation pattern shows a near solid-body rotation, which is not an artifact of low gas density in the bulge, but the beam smearing of FWHM = 0.5 kpc is responsible for a reduction of 70% in the “observed” velocity gradient compared to the unsmoothed case. The line-of-sight velocity dispersion along the major axis shows a high central peak, and a weak decline with radius outside the central region. The beam smearing converts rotation signal into velocity dispersion at the disc centre, increasing the central velocity dispersion by 60% compared to the unsmoothed value of $\sigma_{\text{intrinsic}} = \sigma_{\text{los}}(r = 0) / \sin i = 90 \text{ km s}^{-1}$. This central velocity dispersion is a signature of a massive spheroidal bulge that dominates the dynamics in the central 1-kpc region.

The mock observations presented here are in qualitative agreement with observed massive discs at $z \sim 2$ in the SINFONI survey (Genzel et al. 2006, 2008, 2011). They both show a perturbed, thick rotating disc, a central mostly stellar bulge, and a few giant clumps with no obvious kinematic signal. Galaxy A is less massive than the most massive galaxies observed by a factor of a few, and the giant clumps are less massive than the observed clumps in proportion, but this does not seem to make a qualitative difference. Galaxy E is closer in mass to the massive observed galaxies, and it shows similar kinematics, with clumps of a few times $10^9 M_\odot$. However, the current sample of simulated galaxies does not contain clumps as massive as the few extreme clumps observed with $\sim 10^{10} M_\odot$.

6.2 Rotating clumps in $H\alpha$ observations

The beam smearing has an important effect on the images of the high- z clumpy discs. Figure 19 shows a face-on $H\alpha$ view of galaxy E at $z = 2.3$ for different Gaussian smoothings, ranging from no smoothing to FWHM = 1.6 kpc, corresponding to ~ 0.2 arcsec. The $H\alpha$ surface brightness was computed much the same way as described in §6.1, except that the star formation rate density, ρ_{SFR} , was computed using the distribution of stellar particles younger than 100 Myr. The unsmoothed $H\alpha$ image roughly follows the high density in the gas map shown in Fig. 5, with the giant clumps particularly pronounced. At a beam smearing of FWHM = 0.4 kpc (0.05 arcsec), the clumps are more than doubled in size and the transient structures in the disc are still clearly seen. At larger smoothing scales, the clumps are not resolved — they get gradually bigger and their contrast relative to the background disc diminishes. With FWHM = 1.6 kpc (0.2 arcsec), clumps 5 and 6 are confused to be one clump. We learn that typical Toomre clumps in discs

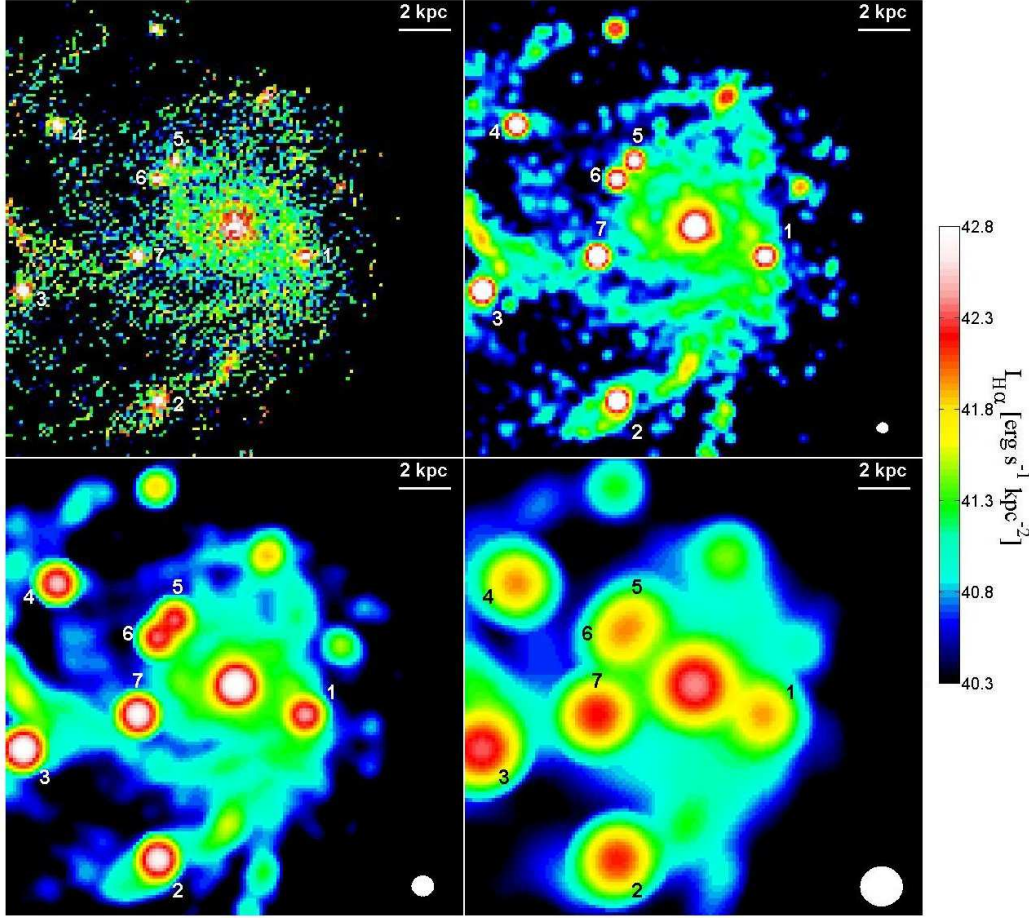


Figure 19. The effect of Gaussian smoothing on the morphology of galaxy E at $z = 2.3$. Shown is the $H\alpha$ surface brightness. The orientation and projection depth are the same as in Fig. 5, namely the disc is face on and the depth is 5 kpc. The 4 panels employ Gaussian smoothing with FWHM= 0, 0.4, 0.8, 1.6 kpc. A white circle in the bottom right corner of each panel has a diameter equal to the FWHM in that panel. The seven clumps of this snapshot are marked in each panel, though with FWHM= 1.6 kpc, clumps 5 and 6 are seen as one clump.

of $\sim 10^{11}M_{\odot}$ are not expected to be resolved with beam smearing of FWHM ~ 0.2 arcsec.³

Figure 20 shows mock observations zooming-in on three rotationally supported clumps from our cosmological simulations: clumps 1 and 4 of galaxy A at $z = 2.3$ and clump 2 of galaxy E at $z = 2.2$. In galaxy A we see one side of the disc, with the clumps along the major axis given the chosen line of sight and the bulge at the right of the frame. In galaxy E the bulge is above the top of the frame, and the clump is along the minor axis given the chosen line of sight. The clump masses are $(0.4, 0.2, 1.2) \times 10^9 M_{\odot}$, their radii determined from the gas density profiles are $(0.45, 0.32, 0.43)$ kpc, their maximum rotation velocities are $(68, 60, 129) \text{ km s}^{-1}$, and the rotation parameters are $\mathcal{R} = 0.86, 0.86, 0.88$. The maximum velocity gradients across the whole clump are $V_{\text{grad}} = 2V_{\text{rot}}/(2R_c) = (150, 190, 280) \text{ km s}^{-1} \text{ kpc}^{-1}$, but it is typically higher

over the range that emits $H\alpha$. The galactic discs are chosen to be observed at high inclinations of $\sin i = 0.98, 0.94$, nearly edge on, and the effective inclinations of the clump spins and the lines of sight are also large, $\sin i_c = 0.98, 0.89, 0.94$. The observed rotation signal is quantified by the maximum gradient across the clump, $V_{\text{grad}} = \max\{\Delta V/(2R_c \sin i)\}$.

Figure 20 shows $H\alpha$ surface density, and $H\alpha$ -weighted line-of-sight velocity and velocity dispersion. The clumps are exposed naked, with no background or foreground contamination from the turbulent and rotating gas in the disc outside the clumps. This is achieved by excluding cells with emissivity below a threshold of $10^{42.2} \text{ erg s}^{-1} \text{ kpc}^{-3}$ for galaxy A and $10^{42.5} \text{ erg s}^{-1} \text{ kpc}^{-3}$ for galaxy E. Each clump is “observed” with 4 different beam smearings, from no smearing, where the signal is smoothed at the 100 pc pixel scale, through Gaussian smoothings of FWHM= 0.2, 0.4, and 0.8 kpc. The latter is comparable to the true clump diameter, and it corresponds to 0.1 arcsec, which is about half the beam smearing in current observations (Genzel et al. 2011).

Clump 3 of galaxy E is close in mass to the typical observed clumps and can thus serve for a direct comparison, but it is significantly smaller than the most massive

³ HST imaging of stellar light in clumps could reach comparable or better resolution, FWHM ≤ 1.2 kpc at $z = 2$ (Förster Schreiber et al. 2011). This provides complementary information on clump stellar mass, radius, and age (Grogin et al. 2011, CANDELS), but it is not useful in the quest for rotation signal.

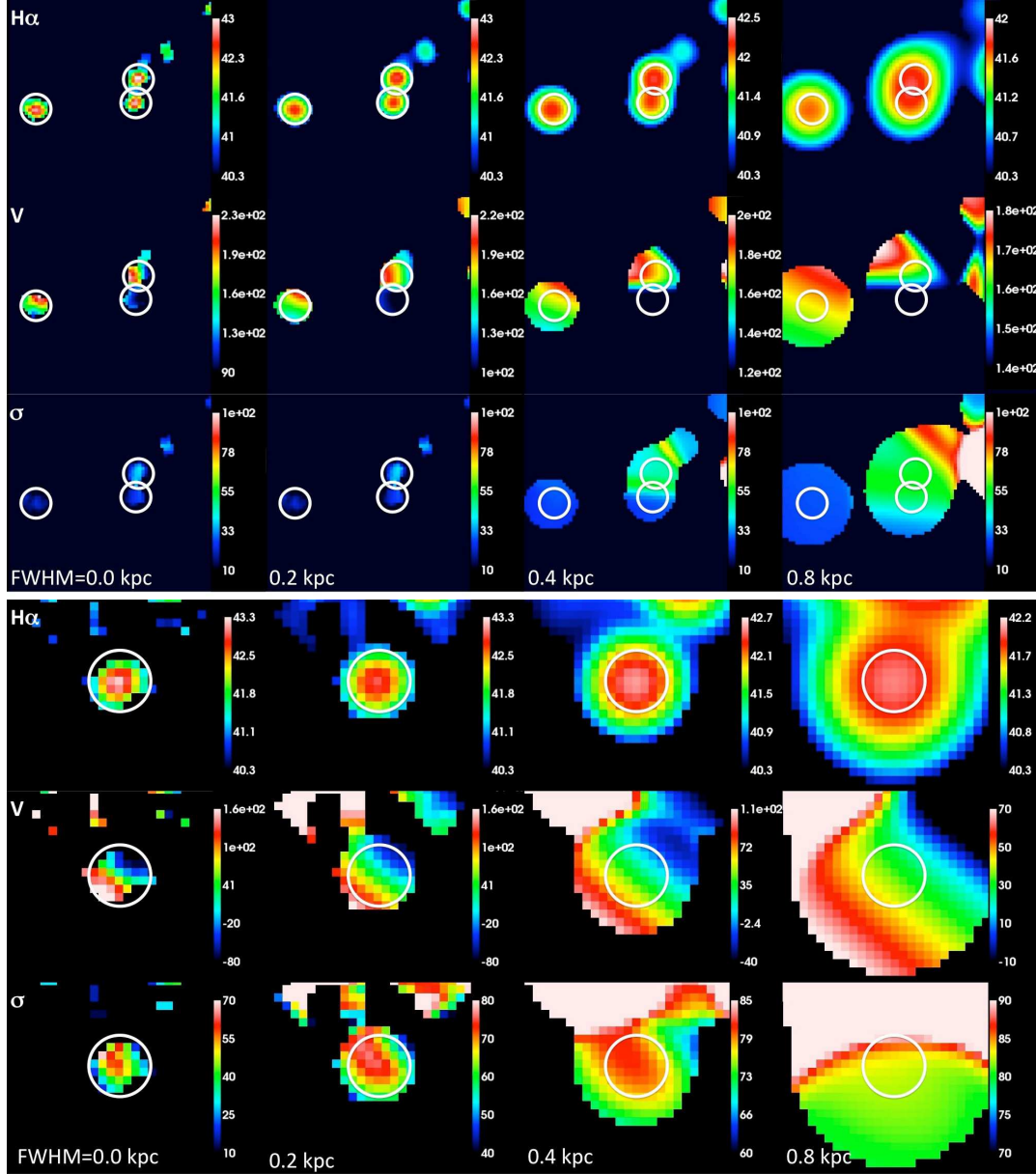


Figure 20. “Observing” rotating giant clumps with different beam smearing. Zoom in on clumps 1 and 4 of galaxy A at $z = 2.3$ (top panels, the clump at the top and the clump on the left) and on clump 2 of galaxy E at $z = 2.2$ (bottom panels). Shown are $H\alpha$ surface brightness (top), $H\alpha$ -weighted line-of-sight velocity (middle), and velocity dispersion (bottom). The clumps are viewed nearly edge on, and almost naked, excluding the foreground and background, to maximize the rotation signal. The beam smearing ranges from zero on the left to FWHM= 0.8 kpc (~ 0.1 arcsec) on the right. The white circles mark radii of 0.3 kpc and 0.42 kpc for the clumps of galaxy A and E respectively, marking the extent of the unsmoothed clump in $H\alpha$.

clumps observed, with $\sim 10^{10} M_{\odot}$. Galaxy A and its clumps are even smaller, and significantly less massive than the big observed galaxies and their clumps, so a quantitative comparison between them requires scaling. Based on Toomre instability (see DSC09), we expect the clump quantities to scale with the galaxy quantities, and $V \sim R \sim M^{1/3}$. This implies that a clump ~ 8 times more massive is expected to have size and velocities twice as big. In particular, when “observing” a clump of mass M_c with a given beam smearing, say FWHM=0.1 arcsec, we mimic the observation of a clump of mass $8M_c$ with twice the beam smearing, FWHM=0.2 arcsec. Once observed with the

proper beam smearing, the velocity gradient, which scales like V/R , is expected to be independent of clump mass.

Clump 1 of galaxy A has been analyzed in some detail in Fig. 3, Fig. 6, and Fig. 8. Its rotation curve is rather flat out to R_c and it is gradually declining outside the clump edge. For this clump, with no beam smearing and naked, we read across the clump $\Delta V = 125 \text{ km s}^{-1}$, which recovers much of the maximum rotation velocity of $2 \times 63 \text{ km s}^{-1}$. Over a scale of $2R = 0.5 \text{ kpc}$, the diameter of the clump in $H\alpha$, unsmoothed, we obtain a gradient of $V_{\text{grad}} = 250 \text{ km s}^{-1} \text{ kpc}^{-1}$. With beam smearing of FWHM= 0.8 kpc, we measure $\Delta V = 28 \text{ km s}^{-1}$ across $2R = 0.8 \text{ kpc}$, namely $V_{\text{grad}} = 35 \text{ km s}^{-1} \text{ kpc}^{-1}$. The

velocity gradient is reduced by a factor of 7 by beam smearing of 0.1 arcsec alone. When including the foreground and background contamination, the gradient is reduced further to $V_{\text{grad}} = 30 \text{ km s}^{-1} \text{ kpc}^{-1}$, another 20% reduction for this clump that resides in the middle of the disc. We measure at the clump position an un-smoothed velocity dispersion of $\sigma = 42 \text{ km s}^{-1}$, and after beam smearing of $\text{FWHM} = 0.8 \text{ kpc}$ it grows to $\sim 60 \text{ km s}^{-1}$, but at such smoothing there is hardly any dispersion signal associated with the clump itself — we basically see a continuous large-scale shallow gradient of dispersion from the bulge (on the left of the picture) outward.

Clump 4 of galaxy A is extremely tilted relative to the disc, $\cos(\text{tilt}) = -0.13$, but it happens to still be not far from edge-on relative to the line of sight, $\sin i_c = 0.89$. The unsmoothed gradient across the $\text{H}\alpha$ clump is $V_{\text{grad}} = 250 \text{ km s}^{-1} \text{ kpc}^{-1}$, and after smoothing with $\text{FWHM} = 0.8 \text{ kpc}$ it is drastically reduced to $V_{\text{grad}} = 15 \text{ km s}^{-1} \text{ kpc}^{-1}$. As in clump 1, there is no noticeable dispersion signal associated with the clump. The contamination by foreground and background in this clump is negligible, because it resides at the outskirts of the disc. Clump 3 of galaxy A, seen just below clump 1, is not seen in the velocity map because its line-of-sight velocity is just outside the range shown by the color scheme.

The massive clump 2 of galaxy E at $z = 2.2$, unsmoothed and naked, shows $\Delta V = 240 \text{ km s}^{-1}$, which recovers much of the maximum rotation velocity of $2 \times 129 \text{ km s}^{-1}$. With $2R = 0.65 \text{ kpc}$, the unsmoothed $\text{H}\alpha$ diameter, we obtain a gradient of $V_{\text{grad}} = 375 \text{ km s}^{-1} \text{ kpc}^{-1}$. With beam smearings of $\text{FWHM} = 0.2, 0.4, 0.8 \text{ kpc}$, we measure $\Delta V = 240, 150, 80 \text{ km s}^{-1}$, and $V_{\text{grad}} = 300, 125, 40 \text{ km s}^{-1} \text{ kpc}^{-1}$ respectively. The velocity gradient is reduced by a factor of 9 by beam smearing of 0.1 arcsec alone. We learn that even this massive clump, which is highly rotation supported and observed nearly edge on, shows only a small rotation signal.

The three clumps analyzed here were all selected to be “observed” with high inclinations relative to the line of sight in order to maximize the rotation signal. Given the frequent occurrence of big tilts between clump and disc, even if the disc is observed nearly edge on, a typical clump is likely not to be edge on, and thus to show an even weaker rotation signal.

In summary, given the current beam smearing, our simulations predict that the typical clumps, which are rotation supported, should show only a weak observable rotation signal, with $\Delta V \sim 10 - 40 \text{ km s}^{-1}$ and $V_{\text{grad}} \sim 15 - 30 \text{ km s}^{-1} \text{ kpc}^{-1}$. The actual signal in individual cases could be even weaker because of (a) low rotation support, (b) low (unknown) inclination of the clump relative to the line of sight, and (c) contamination by gas in the disc outside the clump. The typical clumps, with internal velocity dispersion comparable to the velocity dispersion in the disc, are not expected to show a noticeable signal in the smoothed velocity dispersion field. These predictions for the typical rotation-supported *in situ* disc clumps are consistent with the marginal evidence for weak systematic prograde clump rotation, at a level of $V_{\text{grad}} \sim 10 - 40 \text{ km s}^{-1} \text{ kpc}^{-1}$, and the no noticeable dispersion signal associated with the clumps, as observed for the typical

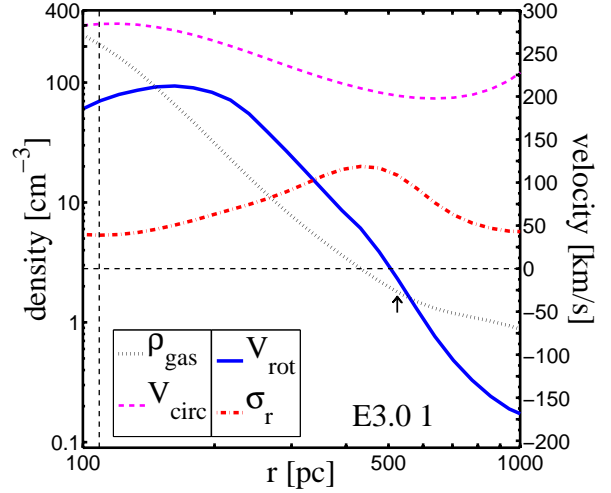


Figure 21. Profiles of the gas in the equatorial plane of *ex situ* clump 1 of galaxy E at $z = 3.0$, similar to Fig. 8. The rotation curve rises to a maximum of $\sim 210 \text{ km s}^{-1}$ but then declines quickly toward the clump edge, beyond which it has a negative value, reflecting the retrograde nature of the clump rotation relative to the disc.

clumps of $\sim 10^9 M_\odot$ (Genzel et al. 2011). This does not apply to the extreme massive clumps observed, which do not have obvious counterparts among the *in situ* Toomre clumps in our simulated discs (see §7).

7 EX-SITU CLUMPS

Among the 86 clumps detected in our simulated discs, we identify 9 (i.e. $\sim 10\%$) as *ex situ* clumps, which came in with the inflowing streams as minor-merging galaxies. They are listed in Table C4 with a proper comment, and appear in some of the statistics figures of §4 marked with a special symbol. Three of these *ex situ* clumps happen to appear in one snapshot, clumps 1, 2 and 4 in galaxy E at $z = 3$, shown in Fig. 5. This is a rare event, immediately following an episode of multiple minor mergers. We defer to another paper a detailed study of the *ex situ* clumps, including their origin, evolution, structure, and kinematics, referring to the three components of gas, stars and dark-matter. Here we limit the discussion to some of the features that distinguish them from the *in situ* clumps.

The *ex situ* clumps are similar in their gas appearance to the *in situ* clumps, and are positioned in or near the disc at different radii, so they cannot be easily distinguished by their morphological appearance. However, in these clumps the dark-matter fraction within the clump radius ranges from 0.1 to 0.4 (compared to less than a few percent in the *in situ* clumps), their mean stellar ages are typically 400 – 1000 Myr (compared to 20 – 400 Myr in the *in situ* clumps), and more than 80% of their stars were formed at distances more than 10 kpc from the disc plane. The *ex situ* clumps mark the massive tail of the clump mass distribution, with clump 1 of galaxy E at $z = 3$ being the most massive clump in the sample, and with 6 of the 9 *ex situ* clumps in the mass range $(2 - 5) \times 10^9 M_\odot$, compared to only 4 *in situ* clumps in that range, all involved in clump interactions

or mergers within the disc. Similarly, 4 of the *ex situ* clumps have a circular velocity V_{circ} in the range $210 - 250 \text{ km s}^{-1}$, compared to the 3 *in situ* clumps with the highest V_{circ} being in the range $180 - 200 \text{ km s}^{-1}$, all involved in mergers, and all other *in situ* clumps having $V_{\text{circ}} < 140 \text{ km s}^{-1}$.

Many of the *ex situ* clumps share the overall disc rotation pattern, but in some cases they have significant velocity components along r or z . However, 3 *ex situ* clumps actually share the overall disc kinematics with deviations much smaller than the dispersion in each component. One of these, clump 2 of galaxy E at $z = 3$, is of mass $M_c \sim 3 \times 10^9 M_\odot$ in a disc of $M_d \sim 3.3 \times 10^{10} M_\odot$ and a bulge twice as massive, thus representing a non-negligible minor merger. This means that minor mergers below a mass ratio of 1:10 may end up joining the disc spatially and kinematically, and could be easily confused with the *in situ* clumps, though they account for only $\sim 10\%$ of the disc clumps.

In terms of their internal kinematics, 5 of the *ex situ* clumps are rotation supported with $\mathcal{R} > 0.88$ and 5 are with a small tilt. They all seem to be in Jeans equilibrium. However, 4 of the clumps are severely tilted by more than 90 degrees, and 3 of the clumps are not supported by rotation, $\mathcal{R} \leq 0.35$. Therefore, the *ex situ* clumps can provide interesting examples of massive clumps that show only little rotation even when marginally resolved. This is because they are not expected to obey the toy model of §2, and the spins of the incoming galaxies could in principle be oriented at a random direction compared to the disc rotation axis. Imagine an *ex situ* clump with a retrograde spin compared to the host disc. The rotation curve in the clump frame will flip from rotation in one sense in the inner radii to rotation in the opposite sense in the outer regions of the clump, where it blends with the overall disc rotation. In this case, it would be hard to detect any rotation signal unless the beam smearing is much smaller than the clump size. There are four examples for this among the *ex situ* clumps in our simulations. Two of them are clumps 1 and 4 of galaxy E at $z = 3$, which have the largest tilts in our whole sample, $\text{costilt} = -0.61$ and -0.40 , respectively. Their inner rotation corresponds to a rotation support factor $\mathcal{R} = 0.11$ and 1.02 , but in both cases it vanishes and then flips to the opposite sense near $r \sim 500 \text{ pc}$, as demonstrated for clump 1 in Fig. 21. These clumps will show no detectable rotation signal when observed with beam smearing of $\text{FWHM} \geq 0.1 \text{ arcsec}$. An example of similar nature is clump 5 of galaxy E at $z = 2.4$, with $\text{costilt} = -0.39$ and $\mathcal{R} = 0.53$, which is a closely interacting clump. These cases may provide a clue for the possible origin of some of the few observed extremely massive clumps that do not show significant rotation despite being marginally resolved (Genzel et al. 2011). Indeed, these clumps have masses $\sim 10^{10} M_\odot$, at the level of $\sim 10\%$ of their host disc mass. This exceeds the Toomre clump mass of only $\sim 2\%$ of the disc mass, as expected from straightforward disc instability analysis (DSC09), and as revealed for the *in situ* clumps in our simulations. Being an *ex situ* clump, or a merger remnant of *in situ* clumps, helps achieving a clump mass more massive than the Toomre mass, though our simulations have not revealed so far clumps as massive as the extreme observed clumps.

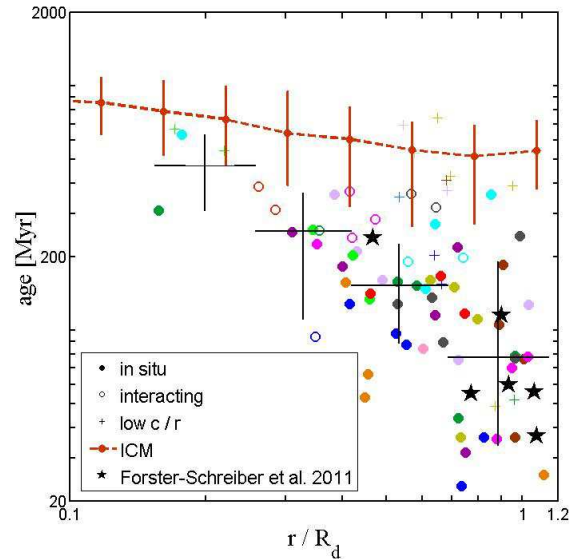


Figure 22. Mean stellar age in clumps versus distance from the disc center relative to disc radius. Symbols and color code for the individual clumps are as in Fig. 9 to Fig. 12. The black crosses mark the median and standard deviation of $\log(\text{age})$ in distance bins, and they are best fitted by the power law $\text{age} \propto r^{-1.2}$. The analysis excludes the low contrast clumps. The dashed line shows the mean stellar age of the inter-clump stellar material in cylindrical shells, best fit by a power law $\text{age} \propto r^{-0.26}$. The black star symbols correspond to estimates based on observations by Förster-Schreiber et al. (2011). There is a significant gradient of clump age with radius, steeper than the gradient of the inter-clump material, and consistent with observations.

8 GRADIENTS OF AGE AND GAS FRACTION

In order to validate our confidence in our predictions for the giant-clump support, it is worthwhile to work out testable predictions for the general scenario of high- z disc instability with long-lived giant clumps as simulated here. Predictions of this sort are associated, for example, with the preferred formation of giant clumps in the outer parts of the disc and their inward migration toward a bulge in the disc center, which imply an age gradient throughout the disc.

Figure 22 shows for all the *in situ* clumps in our simulated sample the mass weighted mean stellar age within each clump radius as a function of its distance from the disc center, normalized to the outer disc radius. One can see a clear trend, where the age is roughly inversely proportional to the radius, fit by a power law $\propto r^{-1.2}$, declining from a median of $\simeq 350 \text{ Myr}$ ($300 - 600 \text{ Myr}$) at $r < 0.3 R_d$ to a median $\simeq 70 \text{ Myr}$ ($20 - 400 \text{ Myr}$) toward $r \sim R_d$. This trend is steeper than the corresponding gradient in the disc stars between the clumps, which is flatter than $r^{-0.3}$ (Mandelker et al., in preparation). The steeper gradient in the clumps reflects the clump migration inwards on top of the inside-out growth of the disc. This difference in the age gradients between the clumps and the inter-clump material thus provides a tool for distinguishing between the scenario simulated here, in which the clumps survive intact during their migration to the bulge, and the scenario where the clumps are disrupted by feedback in $\lesssim 100 \text{ Myr}$, mixing the stellar populations of clumps and disc (Genel et al.

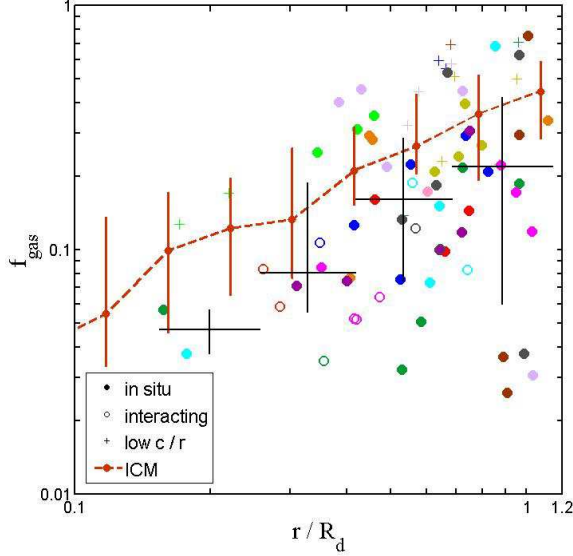


Figure 23. Gas fraction in clumps versus distance from the disc center relative to disc radius. Symbols and lines are as in Fig. 22. The linear regression analysis yields a slope of 0.82. The two outliers with low gas fraction near R_d lie somewhat off plane with non-negligible V_z — the slope becomes unity when these two outliers are excluded. There is a significant gradient of gas fraction with radius.

2010). There are preliminary observational indications for a steep age gradient similar to the gradient predicted here for long-lived clumps (Förster Schreiber et al. 2011).

Figure 23 similarly shows the gas fraction within clumps as a function of distance from the disc center. One can see a clear trend, where the gas fraction is roughly proportional to the radius, increasing from 5-10% in the inner disc to $\sim 30\%$ in the outer disc. Two outliers with low gas fraction near R_d are clumps that lie somewhat off plane with non-negligible V_z . Recall that the overall gas fraction in our simulations at $z \sim 2$ is on the low side compared to observations, associated with a slight overproduction of stars at higher redshifts. This implies that the absolute values of the gas fraction may be unreliable to within a factor of 2, but the trend with radius is likely to be indicative.

The 10% population of *ex situ* clumps would have contaminated these trends, as 8 of the 9 *ex situ* clumps have mean ages older than 400 Myr, and 6 out of the 9 have gas fractions less than 0.05, while they span the whole radius range (Table C4).

9 GMCS AT LOW REDSHIFT

Our simulations of gas-rich discs at high redshift reveal that the typical giant clumps that form *in situ* due to gravitational instability are largely supported by rotation, and indicate that this is not an effect of limited resolution. While this is yet to be confronted with high-redshift observations, the low-redshift analogs, the giant molecular clouds (GMCs), are observed not to be supported by rotation and not in equilibrium (Blitz & Shu 1980; Alves et al. 1998; Blitz & Rosolowsky 2004; Phillips 1999). As a first step in trying to approach this issue, we study the clump support in

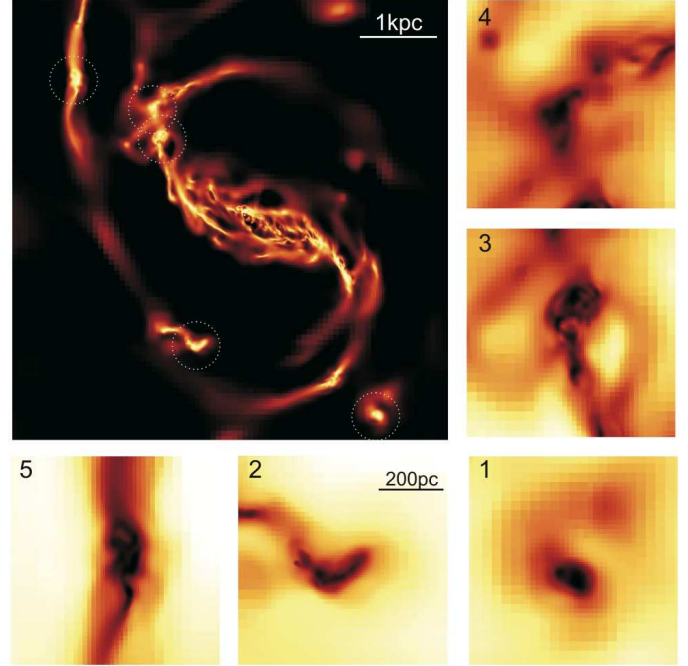


Figure 24. Face-on view of the gas in the low-redshift disc simulation (B10). Surface densities above $50 M_\odot \text{ pc}^{-2}$ are shown in log-scale. The insets zoom in on the five GMCs analyzed in Fig. 25. The GMCs are irregular in shape and dominated by gas.

an isolated $z = 0$ disc galaxy from a RAMSES simulation (Bournaud et al. 2010, hereafter B10), technically similar to the simulations that served our convergence test at high redshift. The simulation technique is the same as described in §5, except that the initial gas fraction is significantly lower, 11% within the stellar disc radius, the initial stellar mass is $3.3 \times 10^9 M_\odot$, one fifth of the stellar mass in the high- z case, and the stellar disc scale length is 1.5 kpc, a factor of 3.7 smaller than in the high- z disc. The model also includes a stabilizing stellar bulge of one tenth of the stellar disc mass. The spatial resolution is $\epsilon_{\text{AMR}} = 0.8 \text{ pc}$ and the mass resolution is $m_{\text{res}} = 5 \times 10^3 M_\odot$, with the Jeans-length floor at 3.2 pc. The simulated GMCs at $z = 0$ are found to be $\sim 10^6 M_\odot$ compared to the $\sim 10^9 M_\odot$ high-redshift clumps. They are typically 10 times smaller in size, with similar central gas volume densities. Thus, the spatial resolution relative to the clump size is slightly better than the MR resolution level in our high- z isolated simulations. With ~ 100 spatial elements per clump in the MR simulation, the rotation parameter was found to be only about 15% higher than in the HR cases, so we expect the resolution effects to be small both in the high- z clumps and the low- z GMCs.

Figure 24 shows a face-on view of the gas surface density in the simulated disc at $t = 268 \text{ Myr}$ after the start, once the turbulent speed and ISM density distribution reached a steady state. Also shown are five main clouds, which are indeed well resolved. These clouds contain mostly gas. They have typical masses and radii $\sim 10^6 M_\odot$ and $\sim 50 - 100 \text{ pc}$ as expected from a Toomre-instability estimate, and their typical internal circular velocity is $V_{\text{circ}} \sim 7.5 \text{ km s}^{-1}$. The five clouds are analyzed in the very same way as the high- z giant clumps. The mass density,

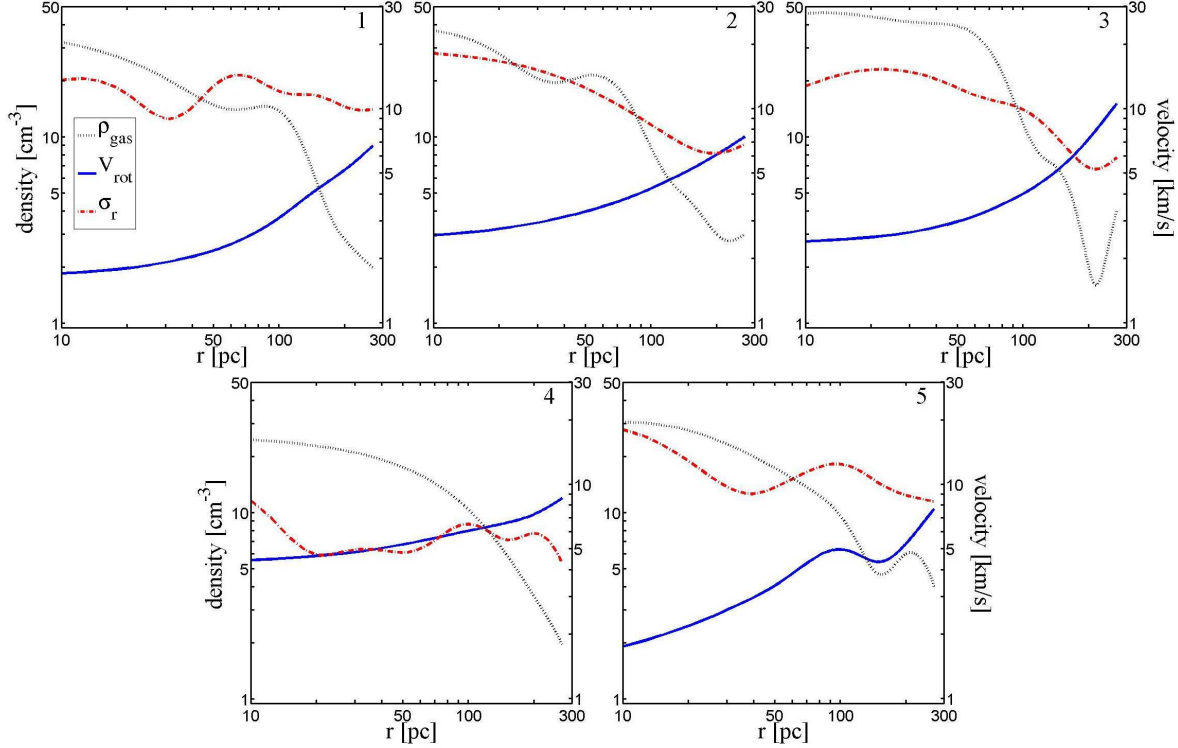


Figure 25. Profiles of the gas in the equatorial plane for the 5 GMCs from the low- z isolated disc simulation (B10). Each panel shows the profiles of density (left axis), rotation velocity and radial velocity dispersion (right axis). The profiles are smoothed as described in Appendix §C. Within the clump, the rotation velocity is smaller than the velocity dispersion.

rotation velocity and radial velocity dispersion profiles are shown in Fig. 25. We see that in 4 out of the 5 GMCs, the rotation velocity within the clump is $V_{\text{rot}} \sim 2.5 \text{ km s}^{-1}$, so the typical rotation parameter is only $\mathcal{R} \sim 0.1$. The rotation velocity is rising only near and outside the clump edge, where it reflects the overall disc rotation. The velocity dispersion is $\sigma \sim 10 \text{ km s}^{-1}$ with an uncertainty $< 1 \text{ km s}^{-1}$ (B10), so $2\sigma^2$ is significantly larger than V_{circ}^2 , indicating that these dispersion-dominated clumps are transients and not in Jeans equilibrium. Indeed, the clump lifetimes are $\sim 20 - 60 \text{ Myr}$. It is encouraging to find that our simulated low- z GMCs are *not* rotation supported, indicating that the rotation support of the high- z clumps is not a numerical artifact.

Fully understanding the origin of the difference between the level of rotation support in high- z and low- z clumps is beyond the scope of the current paper, which focuses on the high- z clumps. We had a quick look at the low- z clumps in order to verify our evaluation that the rotation support at high redshift is not a numerical artifact of resolution, and to demonstrate that having the high- z clumps supported mainly by rotation is not contradictory to having the low- z clumps not supported by rotation (as observed). However, we can highlight important differences and similarities between the high- z and low- z clumps, which may provide hints for the origin of the difference in rotation support.

Assuming that the high- z clumps and the low- z clumps both form entirely by Toomre gravitational instability, a major difference between them is expected to be that the high- z clumps are big and composed of gas and stars, while

the low- z clumps are small and made of gas only. At high redshift, the gas fraction is high, and the stars are relatively young, with their velocity dispersion not much higher than that of the gas, $\sigma_s \sim \sigma_g \sim 50 \text{ km s}^{-1}$. In this case both the stars and the gas participate in the gravitational instability almost as equals, so the clumps are made of the two components. The clump mass, being proportional to the square of the surface density of the baryons, is big, a few percent of the disc mass ($M_c \sim 10^9 M_\odot$ with a circular velocity $V_{\text{circ}} \sim 50 - 100 \text{ km s}^{-1}$). At low redshift, the gas fraction in the disc is low, and the stars keep their high velocity dispersion $\sim 50 \text{ km s}^{-1}$ from the time of their formation. In order to maintain a $Q \sim 1$ Toomre instability under such conditions, the gas has to cool to $\sim 10 \text{ km s}^{-1}$ (Caciatto et al. in prep.). Under the condition $\sigma_g \ll \sigma_s$, only the gas participates in the instability and the clumps contain gas only. Since the gas surface density is low, the forming clumps are small, $M_c \sim 10^{-4} M_d$.

The density contrast between surface density in the clumps and in the background disc, measured at high z for all the baryons and at low z for the gas only, is found in our isolated simulations to be ~ 15 in both cases. Using the simple model of §2, if angular momentum is conserved, the contraction factor $c \sim 4$ implies rotation support with $\mathcal{R} \sim 0.8$ both at high and low redshift. The fact that low- z clumps are not rotation supported, $\mathcal{R} \sim 0.1$, indicates that they must have lost a significant fraction of their angular momentum, by a mechanism that is yet to be understood. This angular-momentum loss may be associated with the escape of a fraction of the few sub-clumps. Given the

lower circular velocity in the low- z clumps, they are also expected to be more susceptible to the effects of supernovae feedback (Dekel & Silk 1986) or radiation-driven feedback (Murray et al. 2010; Krumholz & Dekel 2010) in producing thermal pressure or driving outflows.

As an alternative, it is possible that the trigger for instability and clump formation is somewhat different at low z . While the formation of giant clumps in our simulated high- z discs is initiated by linear gravitational instability in regions where $Q < 1$ (Bournaud et al. 2007; Ceverino et al. 2010; Genzel et al. 2011), the self-gravitating collapse of the low- z GMCs could be triggered by the formation of non-linear perturbations due to gas compression associated with spiral density waves (see also Dobbs et al. 2011) or supersonic turbulent flows. Indeed, some of our low- z clouds seem to form by compression in local shocks, as can be seen, for example, in cloud 2, shown here at $t = 268$ Myr. This cloud started forming just a bit earlier, at $t = 254$ Myr, where an in-plane small-scale velocity component analysis (Fig. 9 in B10) shows a compression flow into a filament, with a local velocity gradient of 27 km s^{-1} over 200 pc. This supersonic velocity also exceeds the circular velocity of this clump, which has a mass of $7 \times 10^5 M_\odot$ and a half-mass radius of 88 pc, indicating that the compression velocity is higher than expected from self-gravitating collapse (though the compression velocity is large only in one direction). This cloud at $t = 268$ Myr has an elongated shape, with 5-6 smaller clumps spread along the filament, suggesting that gas compression by large-scale flows created the initial filament, which subsequently became unstable and fragmented into a few clumps. If low- z GMCs form primarily by turbulent gas compression rather than by pure gravitational instability, then their initial rotation pattern may differ from the global disc rotation assumed in §2, and they may end up rotating with lower velocity than the clumps formed by pure gravitational instability.

10 SUMMARY AND DISCUSSION

We addressed the internal support of the *in situ* giant clumps in gravitationally unstable galactic discs at high redshift, using an analytic model and hydro AMR simulations. Zoom-in cosmological simulations with maximum resolution of 35 – 70 pc were complemented by isolated-disc simulations reaching ~ 1 pc resolution.

The simple analytic model predicts that the protoclumps should be rotating in the sense of the disc rotation. For a disc with a flat rotation curve, if angular momentum is conserved during the collapse of the clump, the relative rotation support of the clump, $\mathcal{R} = V_{\text{rot}}^2 / V_{\text{circ}}^2$, is predicted to be $\mathcal{R} \sim 0.2 c$, where c is the 2D collapse factor of the clump, roughly the square root of the surface-density contrast of the clump with respect to the disc.

We have analyzed 77 *in situ* disc clumps from several snapshots of five zoom-in cosmological simulations of galaxies in the redshift range $z = 2 - 3$, eliminating the few clumps (10%) that contain a significant peak in dark-matter density and are suspect of being external mergers. We also identified $\sim 10\%$ of the *in situ* clumps as associated with a close clump interaction or a recent clump merger, but have not eliminated them from the analysis. The typical clumps

are found to be rotation supported, with a median value of $\mathcal{R} = 0.78$, and where in 82% of the *in situ* clumps the rotation provides most of the support, $\mathcal{R} > 0.5$. The clumps are to a good approximation in Jeans equilibrium, obeying the Jean equation for an isotropic rotator, with the centrifugal force and turbulent pressure force balancing the gravitational attraction. While the typical clump rotation is prograde as expected, except for a few outliers, the clump spin and disc axis show a median tilt of 40° , with a significant tail toward larger tilts. These tilts are associated in many cases with deviations of the local plane from the global disc plane. In general, the clump rotation and contraction factor are consistent with the toy-model prediction and with conservation of angular momentum in the clumps within a factor of a few. There are clumps that indicate significant exchange of angular-momentum, loss by up to 50% or gain by up to a factor of two.

The isolated-galaxy simulations show clumps with similar properties. They are typically rotation supported, but with somewhat smaller tilts. At a resolution comparable to the resolution of the cosmological simulations, they show a similar level of rotation support. Once the clump substructure and internal turbulence are fully resolved, the rotation support parameter is reduced by $\sim 30\%$, at the expense of a comparable increase in the support by velocity dispersion. The median is reduced to $\mathcal{R} \sim 0.6$, confirming the general result that rotation is the dominant source of support in most clumps.

We made a first attempt to address the detectability of clump rotation given the non-negligible beam smearing and other observational limitations at high redshifts. For this purpose, we mimicked H α observations of three clumps from our simulated discs, selected to be highly rotation supported and optimally inclined for a maximum rotational signal. The beam-smearing FWHM was varied from zero to 0.8 kpc, the latter corresponding to ~ 0.1 arcsec at $z \sim 2$, which is about half the beam smearing in current observations. A simple scaling argument implies that an “observation” of a simulated clump of a few $\times 10^8 M_\odot$ with a beam smearing of 0.1 arcsec should have a similar relative smearing effect to the case where a clump 8 times more massive is observed with a beam smearing twice as broad. It also implies that the observed velocity gradient across the clump, $V_{\text{grad}} = \Delta V / (2R_c \sin i)$, should be independent of mass. We find that with a beam smearing of 0.1 arcsec, the rotation signal is reduced by a factor of 5-10, to the level of $V_{\text{grad}} \sim 15 - 30 \text{ km s}^{-1} \text{ kpc}^{-1}$. When the whole clump population is considered, the typical rotation signal is expected to be even weaker because many clumps would be less favorably tilted and with an unknown inclination relative to the line of sight, and because of foreground and background contamination by the turbulent gas in the disc outside the clumps. The rotation signal is also reduced by observational noise, and when the overall disc rotation is subtracted. The velocity dispersion within the clumps is comparable to and sometimes smaller than the dispersion in the disc at the clump vicinity. This leaves no noticeable signal in the observed kinematics for any beam smearing, and the spurious dispersion due to smoothed rotation signal is not enough to make it detectable. These findings from “observing” the simulations are consistent with the marginal detection of a very weak rotation signal, and the lack of a

significant dispersion signal in the typical observed clumps (Genzel et al. 2011).

The extreme observed clumps, with $\sim 10^{10}M_{\odot}$ and no significant rotation signal, are not reproduced as Toomre *in situ* clumps in our current simulations, so they pose an interesting open question. These super-giant clumps may represent merging non-rotating bulges, counter-rotating *ex situ* clumps that joined the host disc (§7), mergers of two or more *in situ* clumps, or, perhaps, big clumps out of equilibrium due to massive outflows (Murray et al. 2010; Genel et al. 2010).

If the high- z clumps indeed tend to be supported by rotation, the fact that the low- z GMCs are observed not to be supported by rotation poses a very interesting open question concerning the clump formation mechanisms in the two cases. We are encouraged by the finding in isolated-galaxy simulations that the low- z clumps indeed tend not to be supported by rotation, while the high- z clumps are mainly rotation supported. We verified that this is not a numerical artifact of resolution (§9). The difference may be due to a different trigger for clump formation. While the high- z clumps are born in a disc that is globally unstable ($Q < 1$) to begin with, it is possible that the low- z GMCs originate from turbulent compression in an otherwise stable disc ($Q > 1$) before they collapse gravitationally. The difference may lie in the fact that the low- z GMCs are less massive by 3 orders of magnitude. For example, if the sub-clumps are of similar masses at low and high redshift clumps, the timescale for two-body relaxation is shorter in the low- z GMCs, which may be associated with escape of subclumps with high angular momentum. Another difference is that supernova feedback and momentum-driven stellar feedback are expected to be more effective in disrupting the less massive low- z GMCs (Murray et al. 2010). The GMCs may therefore be short lived, either collapsing under gravity or expanding due to feedback, but never settled in a long phase of equilibrium. This implies that the clump contraction factor, and the associated surface density contrast, should be small, less than ~ 3 and ~ 10 respectively. This is not the case for the typical clumps in our low- z simulations. However, the short-lived clumps in the simulations with enhanced outflows (Genel et al. 2010) may be of this nature.

Supersonic turbulent motions can dissipate over a dynamical timescale, which is rather short in the giant clumps, ~ 10 Myr, much shorter than the disc orbital time, ~ 250 Myr, or the comparable time for clump migration to the disc centre. The turbulence dissipation time is therefore much shorter than the clump lifetime (unless the clump disrupts on a dynamical timescale). If turbulence was an important source of clump support against gravitational collapse, the turbulence should have been driven continuously by a mechanism that also operates on a dynamical timescale. This could be gravitational interactions between sub-clumps, and between the clump and the rest of the clumpy disc, but it requires further exploration. Our finding that most of the support is actually provided by rotation, which does not dissipate as quickly, alleviates the need for such an efficient driving mechanism for internal turbulence.

If, contrary to the situation in our current simulations, the high- z giant clumps are disrupted on a dynamical timescale, the clumps might never complete their collapse

to rotation-supported equilibrium. This is the case in the simulations of Genel et al. (2010), where disruptive outflows are assumed by implementing an enhanced-outflow version of the phenomenological model of Oppenheimer & Davé (2006, 2008). While this model pushes the effect of outflows to the extreme, as it predicts clump lifetimes shorter than 50 Myr in disagreement with observational estimates, it is certainly possible that the simulations discussed in our paper, which currently implement only energy-driven thermal feedback (Ceverino & Klypin 2009), underestimate the role of outflows. Recent observational indications for massive outflows from massive high- z galaxies (Weiner et al. 2009; Steidel et al. 2010), and from the giant clumps themselves (Genzel et al. 2011), motivate an implementation of more efficient outflow driving mechanisms in our cosmological simulations. It should be done in a physically motivated way, and should allow most clumps to survive in equilibrium for at least ~ 200 Myr, i.e., several clump free-fall times (Dekel & Krumholz, in preparation). But such outflows may keep the clumps somewhat more extended, which may reduce the level of rotation support in them.

Another missing physical mechanism in our current simulations is the effect of magnetic fields. In a different regime, magnetic braking is expected to reduce the angular momentum during the collapse of proto-stellar cores inside molecular clouds (Mouschovias & Paleologou 1979; Basu & Mouschovias 1994). Magnetic effects are expected to become important on a free-fall timescale when the ratio of clump mass to magnetic flux across the clump surface is $\sim (4\pi^2 G \mu_0)^{-1/2}$, where G is Newton's constant and μ_0 is the permeability of free space (Nakano & Nakamura 1978). For a clump of mass $M_c = 10^9 M_{\odot}$ and a proto-clump radius $R_{ci} = 1$ kpc, this condition requires a magnetic field $B \sim (1/2)(M_c/R_{ci}^2)(G\mu_0)^{0.5}$, which is $\sim 100 \mu G$. This is one to two orders of magnitude larger than the ordered magnetic field in the Milky Way, which is a few μG on the large scales relevant for exerting torques on the giant clumps. The magnetic fields in $z \sim 2$ galaxies have not been measured yet, but if they are similarly produced by dynamo effects due to galactic rotation, they are likely to be comparable to the Milky-Way magnetic field, and thus to have only a small effect on any clump angular-momentum loss. On the other hand, the tangled magnetic fields on scales smaller than the giant clumps may be in equipartition with the turbulent motions in the ISM and reach $\sim 100 \mu G$ (Birnboim 2009), thus providing an additional term of pressure support comparable to the turbulent pressure present in the simulations.

The above discussion leads to the conclusion that future cosmological simulations for the study of giant clumps should aim at (1) resolving the clump substructure on scales of a few pc, (2) incorporating realistic momentum-driven outflows via radiative transport, and eventually (3) including magnetic fields via an MHD treatment.

ACKNOWLEDGMENTS

We acknowledge stimulating discussions with Y. Birnboim, M. Cacciato, A. Klypin, T. Naab, and R. Teyssier. The simulations were performed in the astro cluster

at HU, at the National Energy Research Scientific Computing Center (NERSC), Lawrence Berkeley National Laboratory, at NASA Advanced Supercomputing (NAS) at NASA Ames Research Center, and at CCRT and TGCC under GENCI allocation 2011-GEN2192. This work was partially supported by ISF grant 6/08, by GIF grant G-1052-104.7/2009, by a DIP grant, by NSF grant AST-1010033, and by an ERC grant ERC-StG-257720 (FB).

REFERENCES

- Adelberger K. L., Steidel C. C., Shapley A. E., Hunt M. P., Erb D. K., Reddy N. A., Pettini M., 2004, *ApJ*, 607, 226
- Agertz O., Teyssier R., Moore B., 2009, *MNRAS*, 397, L64
- Alves J., Lada C. J., Lada E. A., Kenyon S. J., Phelps R., 1998, *ApJ*, 506, 292
- Basu S., Mouschovias T. C., 1994, *ApJ*, 432, 720
- Binney J., Tremaine S., 2008, *Galactic Dynamics*. Princeton Univ. Press, Princeton, NJ
- Birnboim Y., 2009, *ApJ*, 702, L101
- Birnboim Y., Dekel A., 2003, *MNRAS*, 345, 349
- Blitz L., Rosolowsky E., 2004, *ApJ*, 612, L29
- Blitz L., Shu F. H., 1980, *ApJ*, 238, 148
- Bournaud F., Elmegreen B. G., 2009, *ApJ*, 694, L158
- Bournaud F., Elmegreen B. G., Elmegreen D. M., 2007, *ApJ*, 670, 237
- Bournaud F., Elmegreen B. G., Teyssier R., Block D. L., Puerari I., 2010, *MNRAS*, 409, 1088
- Bournaud, F., in *IAU Symposium 270: Computational Star Formation*, Alves, Elmegreen, Girart & Trimble Eds.
- Bournaud, F., Powell, L. C., Chapon, D., & Teyssier, R. 2011, in *IAU Symposium 271*, N. Brummell, A. S. Brun, M. S. Miesch & Y. Ponty Eds. ; arXiv:1012.5227
- Burkert A., 1995, *ApJ*, 447, L25+
- Burkert A., Genzel R., Bouché N., Cresci G., Khochfar S., Sommer-Larsen J., Sternberg A., Naab T., Förster Schreiber N., Tacconi L., Shapiro K., Hicks E., Lutz D., Davies R., Buschkamp P., Genel S., 2010, *ApJ*, 725, 2324
- Cacciato M., Dekel A., Genel S., 2011, arXiv:1107.0000
- Ceverino D., Dekel A., Bournaud F., 2010, *MNRAS*, 404, 2151
- Ceverino D., Klypin A., 2009, *ApJ*, 695, 292
- Chabrier G., 2003, *PASP*, 115, 763
- Cowie L. L., Hu E. M., Songaila A., 1995, *AJ*, 110, 1576
- Cresci G., Hicks E. K. S., Genzel R., Schreiber N. M. F., Davies R., Bouché N., Buschkamp P., et al., 2009, *ApJ*, 697, 115
- Daddi E., Bournaud F., Walter F., Dannerbauer H., Carilli C. L., Dickinson M., Elbaz D., Morrison G. E., Riechers D., Onodera M., Salmi F., Krips M., Stern D., 2010, *ApJ*, 713, 686
- Daddi E., Cimatti A., Renzini A., Fontana A., Mignoli M., Pozzetti L., Tozzi P., Zamorani G., 2004, *ApJ*, 617, 746
- Daddi E., Dannerbauer H., Elbaz D., Dickinson M., Morrison G., Stern D., Ravindranath S., 2008, *ApJ*, 673, L21
- Danielson A. L. R., Swinbank A. M., Smail I., Cox P., Edge A. C., Weiss A., Harris A. I., Baker A. J., De Breuck C., Geach J. E., Ivison R. J., Krips M., Lundgren A., Longmore S., Neri R., Flaqueur B. O., 2011, *MNRAS*, 410, 1687
- Dekel A., Birnboim Y., 2006, *MNRAS*, 368, 2
- Dekel A., Birnboim Y., Engel G., Freundlich J., Goerdt T., Mumcuoglu M., Neistein E., Pichon C., Teyssier R., Zinger E., 2009, *Nature*, 457, 451
- Dekel A., Sari R., Ceverino D., 2009, *ApJ*, 703, 785
- Dekel A., Silk J., 1986, *ApJ*, 303, 39
- Dobbs C. L., Burkert A., Pringle J. E., 2011, *MNRAS*, 413, 2935
- Dubois Y., Teyssier R., 2008, *A&A*, 477, 79
- Elmegreen B. G., Bournaud F., Elmegreen D. M., 2008, *ApJ*, 688, 67
- Elmegreen B. G., Elmegreen D. M., 2005, *ApJ*, 627, 632
- Elmegreen B. G., Elmegreen D. M., 2006, *ApJ*, 650, 644
- Elmegreen B. G., Elmegreen D. M., Fernandez M. X., Lemonias J. J., 2009, *ApJ*, 692, 12
- Elmegreen D. M., Elmegreen B. G., Hirst A. C., 2004, *ApJ*, 604, L21
- Elmegreen D. M., Elmegreen B. G., Marcus M. T., Shahinyan K., Yau A., Petersen M., 2009, *ApJ*, 701, 306
- Elmegreen D. M., Elmegreen B. G., Ravindranath S., Coe D. A., 2007, *ApJ*, 658, 763
- Elmegreen D. M., Elmegreen B. G., Rubin D. S., Schaffer M. A., 2005, *ApJ*, 631, 85
- Elmegreen D. M., Elmegreen B. G., Sheets C. M., 2004, *ApJ*, 603, 74
- Ferland G. J., Korista K. T., Verner D. A., Ferguson J. W., Kingdon J. B., Verner E. M., 1998, *PASP*, 110, 761
- Förster Schreiber N. M., Genzel R., Bouché N., Cresci G., Davies R., Buschkamp P., Shapiro K., et al., 2009, *ApJ*, 706, 1364
- Förster Schreiber N. M., Genzel R., Lehnert M. D., Bouché N., Verma A., Erb D. K., Shapley A. E., et al., 2006, *ApJ*, 645, 1062
- Förster Schreiber N. M., Shapley A. E., Erb D. K., Genzel R., Steidel C. C., Bouché N., Cresci G., Davies R., 2011, *ApJ*, 731, 65
- Förster Schreiber N. M., Shapley A. E., Genzel R., Bouché N., Cresci G., Davies R., Erb D. K., Genel S., Lutz D., Newman S., Shapiro K. L., Steidel C. C., Sternberg A., Tacconi L. J., 2011, *ArXiv e-prints*
- Fumagalli M. J., Prochaska X., Kasen D., Dekel A., Ceverino D., Primack N., 2011, arXiv:1103.2130
- Genel S., Naab T., Genzel R., Förster Schreiber N. M., Sternberg A., Oser L., Johansson P. H., Davé R., Oppenheimer B. D., Burkert A., 2010, *ArXiv e-prints*
- Genzel R., Burkert A., Bouché N., Cresci G., Förster Schreiber N. M., Shapley A., Shapiro K., et al., 2008, *ApJ*, 687, 59
- Genzel R., Newman S., Jones T., Förster Schreiber N. M., Shapiro K., Genel S., Lilly S. J., Renzini A., Tacconi L. J., et al., 2011, *ApJ*, 733, 101
- Genzel R., Tacconi L. J., Eisenhauer F., Förster Schreiber N. M., Cimatti A., Daddi E., Bouché N., et al., 2006, *Nature*, 442, 786
- Goerdt T., Dekel A., Sternberg A., Ceverino D., Teyssier R., Primack J. R., 2010, *MNRAS*, 407, 613
- Grogin, N. A., Kocevski, D. D., Faber, S. M., et al. 2011, arXiv:1105.3753
- Haardt F., Madau P., 1996, *ApJ*, 461, 20
- Hopkins, P. F., Quataert, E., & Murray, N. 2011, arXiv:1101.4940
- Immeli A., Samland M., Gerhard O., Westera P., 2004,

A&A, 413, 547
 Immeli A., Samland M., Westera P., Gerhard O., 2004, *ApJ*, 611, 20
 Kennicutt Jr. R. C., 1998, *ApJ*, 498, 541
 Kennicutt Jr. R. C., Calzetti D., Walter F., Helou G., Hollenbach D. J., et al., 2007, *ApJ*, 671, 333
 Kereš D., Katz N., Weinberg D. H., Davé R., 2005, *MNRAS*, 363, 2
 Knebe, A., Knollmann, S. R., Muldrew, S. I., et al. 2011, *MNRAS*, 415, 2293
 Komatsu E., Dunkley J., Nolte M. R., Bennett C. L., Gold B., Hinshaw G., Jarosik N., Larson D., Limon M., Page L., Spergel D. N., Halpern M., Hill R. S., Kogut A., Meyer S. S., Tucker G. S., Weiland J. L., Wollack E., Wright E. L., 2009, *ApJS*, 180, 330
 Kravtsov A. V., 2003, *ApJ*, 590, L1
 Kravtsov A. V., Klypin A. A., Khokhlov A. M., 1997, *ApJS*, 111, 73
 Krumholz M., Burkert A., 2010, *ApJ*, 724, 895
 Krumholz M. R., Dekel A., 2010, *MNRAS*, 406, 112
 Law D. R., Steidel C. C., Erb D. K., Larkin J. E., Pettini M., Shapley A. E., Wright S. A., 2007, *ApJ*, 669, 929
 Law D. R., Steidel C. C., Erb D. K., Larkin J. E., Pettini M., Shapley A. E., Wright S. A., 2009, *ApJ*, 697, 2057
 Martig M., Bournaud F., Teyssier R., Dekel A., 2009, *MNRAS*, 707, 250
 Mouschovias T. C., Paleologou E. V., 1979, *ApJ*, 230, 204
 Murray N., Quataert E., Thompson T. A., 2010, *ApJ*, 709, 191
 Nakano T., Nakamura T., 1978, *PASJ*, 30, 671
 Noguchi M., 1999, *ApJ*, 514, 77
 Ocvirk P., Pichon C., Teyssier R., 2008, *MNRAS*, 390, 1326
 Oppenheimer B. D., Davé R., 2006, *MNRAS*, 373, 1265
 Oppenheimer B. D., Davé R., 2008, *MNRAS*, 387, 577
 Phillips J. P., 1999, *A&AS*, 134, 241
 Rand R. J., Kulkarni S. R., 1990, *ApJ*, 349, L43
 Saintonge A., Kauffmann G., Kramer C., Tacconi L. J., et al., 2011, *ArXiv e-prints*
 Shapiro, K. L., Genzel, R., Förster Schreiber, Tacconi, L. J., et al., 2008, *ApJ*, 682, 231
 Stark D. P., Swinbank A. M., Ellis R. S., Dye S., Smail I. R., Richard J., 2008, *Nature*, 455, 775
 Steidel C. C., Adelberger K. L., Giavalisco M., Dickinson M., Pettini M., 1999, *ApJ*, 519, 1
 Steidel C. C., Erb D. K., Shapley A. E., Pettini M., Reddy N., Bogosavljević M., Rudie G. C., Rakic O., 2010, *ApJ*, 717, 289
 Tacconi L. J., Genzel R., Neri R., Cox P., Cooper M. C., Shapiro K., Bolatto A., et al., 2010, *Nature*, 463, 781
 Teyssier R., 2002, *A&A*, 385, 337
 Teyssier R., Chapon D., Bournaud F., 2010, *ApJ*, 720, L149
 Toomre A., 1964, *ApJ*, 139, 1217
 van den Bergh S., 1996, *AJ*, 112, 2634
 Weiner B. J., Coil A. L., Prochaska J. X., Newman J. A., Cooper M. C., Bundy K., Conselice C. J., Dutton A. A., Faber S. M., Koo D. C., Lotz J. M., Rieke G. H., Rubin K. H. R., 2009, *ApJ*, 692, 187

APPENDIX A: COSMOLOGICAL SIMULATIONS WITH THE ART CODE

The cosmological simulations utilize the ART code (Kravtsov et al. 1997; Kravtsov 2003), which accurately follows the evolution of a gravitating N-body system and the Eulerian gas dynamics using an adaptive mesh refinement approach. Beyond gravity and hydrodynamics, the code incorporates many of the physical processes relevant for galaxy formation, as described in Ceverino & Klypin (2009) and in CDB10. These processes, representing subgrid physics, include gas cooling by atomic hydrogen and helium, metal and molecular hydrogen cooling, and photoionization heating by a UV background with partial self-shielding. Cooling and heating rates are tabulated for a given gas density, temperature, metallicity and UV background based on the CLOUDY code (Ferland et al. 1998), assuming a slab of thickness 1 kpc. A uniform UV background based on the redshift-dependent Haardt & Madau (1996) model is assumed, except at gas densities higher than 0.1 cm^{-3} , where a substantially suppressed UV background is used ($5.9 \times 10^{26} \text{ ergs}^{-1} \text{ cm}^{-2} \text{ Hz}^{-1}$) in order to mimic the partial self-shielding of dense gas. This allows the dense gas to cool down to temperatures of $\sim 300 \text{ K}$. The assumed equation of state is that of an ideal mono-atomic gas. Artificial fragmentation on the cell size is prevented by introducing a pressure floor, which ensures that the Jeans scale is resolved by at least 7 cells (see CDB10).

Star formation is assumed to occur at densities above a threshold of 1 cm^{-3} and at temperatures below 10^4 K . More than 90% of the stars form at temperatures well below 10^3 K , and more than half the stars form at 300 K in cells where the gas density higher than 10 cm^{-3} . The code implements a stochastic star-formation model that yields a star-formation efficiency per free-fall time of 5%. At the given resolution, this efficiency roughly mimics the empirical Kennicutt law (Kennicutt 1998). The code incorporates a thermal stellar feedback model, in which the combined energy from stellar winds and supernova explosions is released as a constant heating rate over 40 Myr following star formation, the typical age of the lightest star that explodes as a type-II supernova. The heating rate due to feedback may or may not overcome the cooling rate, depending on the gas conditions in the star-forming regions (Dekel & Silk 1986; Ceverino & Klypin 2009). No shutdown of cooling is implemented. We also include the effect of runaway stars by assigning a velocity kick of $\sim 10 \text{ km s}^{-1}$ to 30% of the newly formed stellar particles. The code also includes the later effects of type-Ia supernova and stellar mass loss, and it follows the metal enrichment of the ISM.

The five selected halos were drawn from an N-body simulation. The initial conditions corresponding to each of the selected haloes were filled with gas and refined to a much higher resolution on an adaptive mesh within a zoom-in Lagrangian volume that encompasses the mass within twice the virial radius at $z = 1$, roughly a sphere of comoving radius 1 Mpc. This was embedded in a comoving cosmological box of side 20 and $40 h^{-1} \text{ Mpc}$ for galaxies A-C and D-E respectively. A standard ΛCDM cosmology has been assumed, with the WMAP5

cosmological parameters $\Omega_m = 0.27$, $\Omega_\Lambda = 0.73$, $\Omega_b = 0.045$, $h = 0.7$ and $\sigma_8 = 0.82$ (Komatsu et al. 2009). The zoom-in regions have been simulated with $\sim (4 - 11) \times 10^6$ dark-matter particles of mass $6.6 \times 10^5 M_\odot$ each, and the particles representing stars have a minimum mass of $10^4 M_\odot$. Each galaxy has been evolved forward in time with the full hydro ART and subgrid physics on a adaptive comoving mesh refined in the dense regions to cells of minimum size 70 pc or smaller in physical units at all times. Each AMR cell is refined to 8 cells once it contains a mass in stars and dark matter higher than $2 \times 10^6 M_\odot$, equivalent to 3 dark-matter particles, or it contains a gas mass higher than $1.5 \times 10^6 M_\odot$. This quasi-Lagrangian strategy ends at the highest level of refinement that marks the minimum cell size at each redshift. In particular, the minimum cell size is set to 35 pc in physical units at expansion factor $a = 0.16$ ($z = 5.25$), but due to the expansion of the whole mesh while the refinement level remains fixed, the minimum cell size grows in physical units and becomes 70 pc by $a = 0.32$ ($z = 2.125$). At this time we add a new level to the comoving mesh, so the minimum cell size becomes 35 pc again, and so on. This maximum resolution is valid in particular throughout the cold discs and dense clumps, allowing cooling to ~ 300 K and gas densities of $\sim 10^3 \text{ cm}^{-3}$.

APPENDIX B: ISOLATED GALAXY SIMULATIONS WITH THE RAMSES CODE

To investigate the effects of numerical resolution and small-scale substructure, we use simulations of idealized, isolated, gas-rich disc galaxies representative of $z \sim 2$ star-forming galaxies. The absence of continuous cosmological gas supply limits the duration of disc evolution that can be followed, but it permits a much higher resolution than the cosmological simulations. Overall, the initial conditions and evolution into $z = 2$ -like clumpy discs are as described in Bournaud et al. (2007, BEE07), but the current simulations were performed with much higher resolution using the AMR code RAMSES (Teyssier 2002), comparable in many ways to the ART code used in the cosmological simulations utilized in the rest of this paper.

The technique relies on a quasi-Lagrangian refinement of the AMR grid and a barotropic equation of state for the heterogeneous ISM (Teyssier et al. 2010; Bournaud et al. 2010). Each AMR cell is refined once (i) it contains a gas mass higher than m_{res} , or (ii) it contains more than 20 particles, or (iii) the local thermal Jeans length is resolved by less than four cells. The refinement continues up to a minimum cell size ϵ_{AMR} . To avoid artificial fragmentation, a pressure floor ensures that the thermal Jeans length is at least $4\epsilon_{\text{AMR}}$. Star formation occurs above a volume density threshold n_{SF} , with an efficiency 4% per free-fall time (Teyssier et al. 2010). Supernovae feedback is implemented based on the blast-wave model of Dubois & Teyssier (2008), where a fraction $\eta_{\text{SN}} = 50\%$ of the supernova energy is deposited as bulk motion in a gas bubble of radius $3 \times \epsilon_{\text{AMR}}$, and the rest being radiated away. Gas cooling down to low temperatures (below 100 K at the highest resolution) is modeled using a barotropic equation of state, which assumes thermal equilibrium between heating by a standard UV background and cooling by fine-structure and metal

lines. While a possible multi-phase instability is neglected, a cloudy, heterogeneous medium naturally results. This technique reproduces a realistic phase-space ISM structure for nearby disc galaxies (Bournaud et al. 2010), their molecular clouds (Bournaud 2010), and basic properties of merging galaxies (Teyssier et al. 2010; Bournaud 2011).

We performed three simulations of a system that represents a massive disc at $z \sim 1 - 3$, at a high resolution (HR), medium resolution (MR) and low resolution (LR), as listed in Table 1. The resolution in the LR simulation is similar to the resolution in the cosmological simulations, with slightly lower spatial resolution but somewhat higher mass resolution. The HR simulation resolves gas densities up to 10^7 cm^{-3} and sizes of a few parsecs, comparable to today's molecular clouds. The resulting density power spectrum for the HR model (Bournaud et al. 2010, section 3.4 and Figure 15) is characteristic of a fully developed three-dimensional turbulence cascade, implying that the HR resolution is sufficient for convergence on the internal properties of kpc-size clumps.

The simulations start with a pre-formed disc of half gas and half stars, and a stellar mass of $\sim 1.5 \times 10^{10} M_\odot$. The initial stellar disc is exponential with radial scale-length $R_d/4$, truncated at radius $R_d = 16 \text{ kpc}$. The gas disc is exponential with scale-length $R_d/1.5$. The ratio of dark matter to baryons within R_d is 0.33, and the spherical dark matter halo has a Burkert (1995) profile with radial-scale length $R_d/3$, matching high-redshift rotation curves.

APPENDIX C: MEASURING CLUMP PROPERTIES IN THE SIMULATIONS

C1 Clump finding

The disc plane is determined by the angular momentum of cold gas ($T < 10^4 \text{ K}$) within a sphere of radius comparable to the disc radius, as estimated by eye. Clump candidates are identified upon visual inspection of the face-on, gas surface density map of the disc, searching for compact gas structures with an estimated surface density contrast of ~ 3 or more compared to the local background. Therefore, we exclude low-contrast, elongated features from our analysis.

A cube of side $\pm 1.2 \text{ kpc}$ is examined about the estimated centre of each clump. For a smoother calculation, the AMR cells in this volume are split to create a uniform grid, with a cell size half the size of the smallest AMR cell. A friends-of-friends algorithm is then employed, linking together neighboring cells with gas temperature $T < 10^4 \text{ K}$. Of all the identified groups with more than 80 cells, the one closest to the initial guess for the center is selected as the clump. In most cases, this is also the largest identified group (excluding the central bulge). Otherwise, the group with the highest central density is selected. The center of mass of this group is calculated, $\vec{r}_{\text{cm,temp}}$, and is further refined as follows. All the cells in the clump within 500 pc of $\vec{r}_{\text{cm,temp}}$ are searched for the point which maximizes the mass in a sphere of radius $r = 250 \text{ pc}$ centered on that point. The clump center \vec{r}_{cm} is then taken to be the center of that sphere. The center of mass velocity of the clump, v_{cm} , is the center of mass velocity inside that sphere.

C2 Clump minor axis

The spherical density profile of the gas about the clump center is calculated in 80 equal bins of $\log r$, of width 0.15 dex each, in the interval 1.0 to 3.4 (where r is in pc), namely spacing of 0.03 dex between the bin centers. The profile is smoothed such that the density in every bin is replaced by a Gaussian weighted average of the densities in the 5 neighboring bins, with a FWHM of 0.06 dex. The radius of the spherical clump, R_s , is then determined by searching the smoothed density profile at $r_i > 178$ pc for the smallest radius that meets one of the following three conditions:

- (i) $\rho'_i > -2$
- (ii) $\rho'_i/\rho'_{i-1} < 0.8$
- (iii) $|\rho'_i| < \min\{|\rho'_{i-1}|, |\rho'_{i+1}|\}$

where $\rho' \equiv d \log \rho / d \log r$. If $\rho'_i > -2$ for all bins, the first condition is replaced by $\rho'_i > -1$. This happened in 4 out of the 86 clumps. The above definition of clump radius is very similar to the standard definition of subhalo radius generally used in dark-matter halo-finders (Knebe et al. 2011). The subhalo radius is defined as the truncation radius or saddle point, where the density profile has an inflexion or upturn point due to the embedding of the subhalo within a background host. The angular momentum is computed for the cold gas ($T < 10^4$ K) in a spherical shell between $(2/3)R_s$ and R_s about \vec{r}_{cm} . This determines the minor axis of the clump, \hat{z} .

C3 Internal clump structure and kinematics

The profiles of density and velocity are computed in the major, equatorial plane of the clump, that is perpendicular to the minor axis. For this, we rotate the uniform cubic grid to match the clump frame. In an equatorial slice of thickness 100 pc along the minor axis, we use 80 cylindrical radial bins of width 0.15 dex spaced 0.03 dex as before. Using these bins, we compute the gas density profile, and the mass weighted average value of the rotation velocity v_ϕ , as well as the three components of velocity dispersion σ_r , σ_ϕ and σ_z . The profiles in the equatorial plane are smoothed in the same manner described in the previous section for the spherical profiles. The clump radius, R_c , is determined from the density profile in the equatorial plane in the same manner as R_s was determined from the spherical density profile. The average rotation velocity V_{rot} and radial velocity dispersion σ_r are computed mass-weighted within the cylindrical bin $0.5R_c - R_c$ in the equatorial plane. For clumps where $0.5R_c < 150$ pc, namely smaller than the force resolution, the inner radius $0.5R_c$ is replaced by 150 pc. Our adopted definition of clump radius agrees well with the visual impression from the face on images of the gas surface density in the clumps and the local disc environment. We tested several alternative definitions for the clump radius and the average internal velocities, and found that our qualitative conclusions are insensitive to the exact algorithm adopted.

C4 Global clump properties

The total clump mass M_c , including gas, stars and dark matter, is computed within R_c . The gas mass, stellar mass,

and dark-matter mass, are computed accordingly. For the purpose of computing the effective circular velocity of the clump, we define the mass-weighted average radius R_{sh} in the shell $0.5R_c - R_c$, compute the total mass within a sphere of that radius, $M(R_{\text{sh}})$, and then compute $V_{\text{circ}}^2 = GM(R_{\text{sh}})/R_{\text{sh}}$. The rotation parameter is $\mathcal{R} = (V_{\text{rot}}/V_{\text{circ}})^2$.

In order to determine a contraction factor c , we compute the clump baryonic surface density $\Sigma_c = M_{\text{bar}}(R_{\text{sh}})/(\pi R_{\text{sh}}^2)$, and write $c^2 = \Sigma_c/\Sigma_d$ where Σ_d is the relevant background density in the disc. Σ_d is computed in a cylindrical shell from R_{bulge} to R_d , and with height h . The values of these three numbers are determined by visual inspection as follows. The disc radius is set where the gas surface density profile averaged over circular rings drops below 10^{21} cm^{-2} . The bulge radius is taken to be where the stellar density profile drops below $10^4 \text{ M}_\odot \text{ pc}^{-2}$. The scale height is determined where the edge-on surface density drops below 10^{21} cm^{-2} , but the mean disc surface density is insensitive to the choice of scale height. If the disc surface density severely deviates from axial symmetry, e.g., in galaxy E at $z = 2.2\text{--}2.4$, then the center of the cylindrical shell is taken to be at the center of mass in the disc. We include all the gas in the disc. A star particle is assigned to the disc only if the z -component of its angular momentum j_z (parallel to the total galaxy angular momentum) is higher than a fraction f_J of the maximum angular momentum for the same orbital energy, $j_{\text{max}} = |v|r$, where $|v|$ is the magnitude of the particle velocity and r is its distance from the center. We adopt as default $f_J = 0.7$ (see CDB10). We note that the relevant surface densities for quantifying a contraction factor as well as the clump radii are quite uncertain, so the values of c should be taken with a grain of salt.

When comparing the clump masses and radii, we find a general trend $R_c \propto M_c^{1/3}$, as expected. The relation between these quantities do not reveal an obvious sign of resolution effects limiting the clump properties at small clumps, but naturally clumps of $R_c < 300$ pc or $M_c < 3 \times 10^8 \text{ M}_\odot$ should be considered less certain.

The mean stellar age of each clump is determined by the mass-weighted average of the stellar ages inside R_c .

The profiles of gas density, rotation velocity and velocity dispersion shown in Fig. 15, Fig. 16 and Fig. 25 for the clumps from the high-resolution isolated-galaxy simulations were obtained in radius bins and then smoothed using a cubic spline algorithm. This is obtained by fitting a piecewise 3rd degree polynomial, such that the sums in quadrature of both the residuals and the second derivatives are minimized. Tolerance for the sum in quadrature of residuals is taken to be equal to the total variance of the data for the velocity curves and 0.15 of the variance for the density profiles.

This paper has been typeset from a \LaTeX file prepared by the author.

Table C3. Masses and Radii of the selected galaxies. The radii are in kpc and the masses are in $10^{10}M_{\odot}$.

Gal z	R_{disc}	R_{bulge}	M_{gas}	M_{star}	M_{DM}	M_{bulge}	M_{disc}	$M_{\text{disc}}/M_{\text{total}}$	$M_{\text{gas}}/M_{\text{disc}}$	$M_{\text{bulge}}/M_{\text{disc}}$	$M_{\text{clumps}}/M_{\text{disc}}$
A 2.3	5.8	2.0	0.37	1.7	2.1	1.0	1.1	0.26	0.35	0.93	0.19
A 2.1	5.5	2.0	0.36	2.4	2.1	1.2	1.6	0.32	0.23	0.75	0.14
B 2.3	3.4	1.0	0.20	1.3	0.92	0.81	0.66	0.27	0.30	1.22	0.21
C 2.3	4.6	1.5	0.46	11.0	3.4	6.6	5.3	0.35	0.09	1.25	0.008
C 2.1	5.0	1.5	0.75	13.2	3.9	9.7	4.2	0.24	0.18	2.30	0.05
C 1.9	5.0	1.5	0.97	17.9	4.8	13	5.9	0.25	0.17	2.22	0.06
D 2.3	5.0	2.0	0.39	3.9	2.7	2.2	2.0	0.29	0.19	1.09	0.08
E 3.0	6.0	2.0	0.75	9.7	7.9	7.1	3.3	0.18	0.23	2.16	0.08
E 2.8	8.0	2.0	0.89	11.3	11.9	7.9	4.2	0.17	0.21	1.89	0.04
E 2.7	8.0	2.0	0.93	11.8	11.5	7.9	4.8	0.20	0.19	1.65	0.07
E 2.6	8.0	2.0	0.85	12.4	11.9	7.9	5.3	0.21	0.16	1.49	0.09
E 2.4	8.0	2.0	0.83	13.3	12.1	8.2	5.8	0.22	0.14	1.41	0.08
E 2.3	8.5	2.0	0.73	14.1	13.3	8.4	6.4	0.23	0.11	1.32	0.11
E 2.2	8.5	2.0	0.80	14.9	13.6	8.7	6.9	0.24	0.12	1.26	0.10
E 2.1	8.5	2.0	0.81	15.5	13.9	9.1	7.1	0.24	0.11	1.28	0.08
E 2.0	9.0	2.0	0.90	15.9	14.8	9.4	7.4	0.23	0.12	1.28	0.005

Table C1. Virial properties of the selected galaxies. All virial properties are defined at the virial radius that encompasses a mean mass density of 180 times the universal density. The radius R_v is expressed in proper kpc, the mass M_v is in units of $10^{12}M_{\odot}$, and the velocity V_v is in km s^{-1} .

Gal z	R_v	M_v	V_v
A 2.3	70	0.40	150
A 2.1	88	0.60	171
B 2.3	68	0.35	140
C 2.3	83	0.61	180
C 2.1	97	0.81	188
C 1.9	109	0.94	192
D 2.3	96	0.94	205
E 3.0	91	1.35	252
E 2.8	95	1.37	249
E 2.7	100	1.43	248
E 2.6	105	1.47	245
E 2.4	109	1.52	244
E 2.3	114	1.54	241
E 2.2	118	1.55	237
E 2.1	122	1.57	235
E 2.0	127	1.63	234

Table C2. Kinematic disc properties of the selected galaxies. Rotation velocities and radial velocity dispersions for gas and stars are in km s^{-1} .

Gal z	V_{gas}	σ_{gas}	$(\sigma/V)_{\text{gas}}$	V_{star}	σ_{star}	$(\sigma/V)_{\text{star}}$
A 2.3	180	20	0.11	160	33	0.22
A 2.1	203	22	0.11	178	37	0.21
B 2.3	180	25	0.14	157	34	0.26
C 2.3	380	60	0.16	356	107	0.30
C 2.1	427	52	0.12	331	103	0.31
C 1.9	465	41	0.09	378	128	0.34
D 2.3	264	24	0.09	222	53	0.24
E 3.0	370	29	0.08	311	88	0.28
E 2.8	397	22	0.05	295	81	0.27
E 2.7	382	25	0.06	309	81	0.26
E 2.6	384	24	0.06	342	92	0.27
E 2.4	400	23	0.06	322	92	0.28
E 2.3	407	27	0.07	346	98	0.28
E 2.2	419	17	0.04	345	102	0.29
E 2.1	433	17	0.04	368	109	0.30
E 2.0	424	9	0.02	346	107	0.31

Table C4. Clump properties. “cl” marks the arbitrary clump number. R_c is the clump radius in pc. M_c is the clump mass in $10^8 M_\odot$. Velocities are in km s^{-1} . “tilt” is $\cos(\text{tilt})$. Σ_c is the baryonic surface density within the clump in $10^8 M_\odot \text{kpc}^{-2}$. f_{DM} and f_g are the fractions of dark matter and gas within the clump radius. “age” is the mean stellar age within the clump in Myr. r and z are the disc polar coordinates of the clump center in kpc.

Gal z	cl	R_c	M_c	V_{circ}	V_{rot}	σ_r	\mathcal{R}	tilt	Σ_c	c	f_{DM}	f_g	age	r	z	V_r	V_z	V_{rot}/V_d	comm.
A2.3	1	454	3.9	68	63	24	0.86	0.94	1.1	4.2	0.07	0.12	128	2.4	-0.20	13	20	190/170	merger
	2	278	3.8	81	37	26	0.21	0.53	2.4	6.3	0.02	0.10	94	2.0	0.37	13	11	177/170	
	3	454	2.5	52	37	17	0.51	0.84	0.6	3.2	0.05	0.21	87	3.2	-0.14	-35	11	157/170	
	4	322	1.9	61	57	9.2	0.86	-0.13	1.3	4.6	0.01	0.21	36	4.8	-0.34	-1.4	13	166/170	
	5	292	1.8	58	54	10	0.87	0.43	1.2	4.4	0.02	0.07	97	3.1	-0.04	-12	60	191/170	low c
	6	411	2.6	57	51	13	0.80	0.34	0.9	3.8	0.02	0.29	23	4.2	0.58	33	44	180/170	
	7	816	2.4	32	33	12	1.1	0.67	0.1	1.3	0.29	0.42	203	3.7	0.03	-5.4	12	202/170	low c
	8	609	1.9	32	26	27	0.67	0.80	0.2	1.6	0.18	0.46	155	3.8	0.24	-37	14	172/170	
	9	816	4.2	37	36	20	0.94	0.85	0.1	1.4	0.42	0.17	412	2.4	-0.12	-1.3	-18	164/170	<i>ex situ</i>
	10	338	3.2	71	59	26	0.69	0.74	1.2	4.5	0.30	0.05	393	2.8	0.74	-204	-236	93/170	<i>ex situ</i>
A2.1	1	229	3.2	87	85	18	0.95	-0.02	3.1	5.9	0.00	0.03	127	5.7	-0.62	-61	-93	137/150	low c
	2	355	1.8	48	31	12	0.42	0.47	0.7	2.8	0.03	0.43	76	4.0	-0.98	-69	-8.1	208/200	
	3	900	4.9	40	32	18	0.64	0.52	0.2	1.3	0.21	0.45	374	3.7	-0.63	-37	-29	222/200	
	4	431	3.1	59	50	24	0.71	0.86	0.8	3.0	0.04	0.21	161	2.7	0.52	-1.2	-19	203/210	
	5	552	3.9	51	44	28	0.74	0.84	0.4	2.2	0.12	0.40	211	2.4	-0.07	1.3	2.0	190/210	
	6	671	5.4	50	40	41	0.62	0.99	0.3	1.9	0.18	0.33	360	2.1	0.07	23	-19	220/220	
B2.3	1	373	4.6	52	73	58	1.9	0.98	0.6	2.4	0.18	0.10	667	0.6	0.08	22	93	203/220	low r
	2	391	3.0	43	81	33	3.5	0.93	0.4	1.8	0.23	0.13	547	0.8	-0.06	-34	23	240/220	low r
	3	454	2.9	44	41	25	0.88	0.99	0.4	1.8	0.18	0.20	258	1.2	0.08	23	1.8	178/180	<i>ex situ</i>
	4	454	2.6	42	28	30	0.46	0.94	0.3	1.7	0.16	0.26	203	1.4	0.01	-1.9	-0.3	174/180	
	5	292	1.0	33	26	13	0.60	0.84	0.4	1.8	0.10	0.32	134	1.6	-0.09	6.3	-9.8	167/180	
	6	338	7.5	110	55	47	0.25	-0.11	3.3	5.4	0.18	0.11	218	2.6	-0.07	-94	169	-318/-100	
C2.3	1	278	24	211	121	101	0.33	0.96	15	5.6	0.09	0.01	940	4.9	0.54	-166	-166	300/260	<i>ex situ</i>
	2	454	4.2	47	34	27	0.53	0.97	0.5	1.0	0.11	0.12	352	2.5	-0.38	22	-104	431/440	low c
C2.1	1	776	7.4	56	89	84	2.5	0.35	0.4	1.2	0.16	0.37	534	2.9	-2.0	41	62	437/410	low c
	2	900	14	72	22	32	0.10	0.44	0.5	1.4	0.17	0.27	695	2.7	1.0	34	-52	443/420	low c
C1.9	1	373	4.0	73	54	25	0.55	0.80	1.5	2.0	0.03	0.26	111	4.0	1.3	-40	-53	464/450	low c
	2	292	2.4	63	56	24	0.79	0.43	1.4	1.9	0.03	0.20	160	3.1	0.55	-8.6	-105	544/470	
	3	391	4.3	72	55	25	0.59	0.85	1.3	1.8	0.06	0.22	151	3.5	0.39	-69	6.1	483/460	
	4	229	3.1	78	65	42	0.70	0.81	2.4	2.5	0.00	0.40	36	3.6	0.00	28	-8.6	453.6/460	
	5	252	1.3	44	23	16	0.27	0.85	0.7	1.4	0.03	0.22	49	4.4	0.2	-42	41	452/450	
	6	671	3.0	42	54	27	1.6	0.91	0.3	1.4	0.16	0.42	390	4.8	0.06	42	85	404/440	
	7	740	12	67	82	35	1.5	0.88	0.6	1.3	0.12	0.20	740	3.2	-0.24	90	-50	550/470	
	8	476	2.3	41	41	16	1.0	0.96	0.3	0.9	0.15	0.43	427	3.5	1.1	116	46	371/460	
D2.3	1	338	2.7	67	54	18	0.66	0.95	1.4	3.5	0.05	0.15	141	2.3	-0.48	-58	-4.6	286/300	
	2	432	4.6	78	54	11	0.49	0.57	1.5	3.6	0.03	0.14	118	3.7	-0.49	45	36	285/260	
	3	373	8.3	114	108	32	0.90	0.01	3.8	5.8	0.02	0.10	167	3.3	0.60	31	-12	222/270	

Table C5. Continuation of Table C4

Gal z	cl	R_c	M_c	V_{circ}	V_{rot}	σ_r	\mathcal{R}	tilt	Σ_c	c	f_{DM}	f_g	age	r	z	V_r	V_z	V_{rot}/V_d	comm.
E3.0	1	525	49	219	73	111	0.11	-0.61	8.3	8.0	0.17	0.04	727	1.3	-0.47	-148	76	469/450	<i>ex situ</i>
	2	265	31	250	246	40	0.97	0.99	21	13	0.11	0.07	636	4.3	-0.04	-6.1	-0.7	368/390	<i>ex situ</i>
	3	391	5.2	88	78	13	0.78	0.09	2.2	4.1	0.02	0.29	36	5.8	-0.48	135	40	319/350	
	4	292	31	236	239	27	1.02	-0.40	18	12	0.15	0.01	831	7.4	1.1	59	465	351/320	<i>ex situ</i>
	5	816	7.0	56	80	31	2.00	0.98	0.4	1.7	0.27	0.50	414	4.1	-0.19	42	64	370/390	low c
	6	373	1.8	41	21	16	0.27	0.66	0.5	1.9	0.05	0.72	76	6.0	0.16	-164	-5.5	347/350	
	7	391	4.4	80	79	37	0.97	-0.26	1.8	3.7	0.04	0.02	185	5.4	-1.8	-5.7	181	461/370	
	8	579	8.5	86	114	114	1.76	-0.05	1.3	3.1	0.07	0.03	106	5.3	-1.1	17	101	472/370	
E2.8	1	338	5.0	87	38	52	0.19	0.35	2.3	4.1	0.04	0.07	157	3.3	0.33	-51	110	432/410	3
	2	355	3.9	75	54	16	0.51	0.68	1.7	3.5	0.05	0.28	53	3.6	0.67	-20	-4.5	374/420	
	3	292	2.8	65	41	31	0.39	0.04	1.5	3.2	0.05	0.27	66	3.6	0.26	-39	-37	455/420	
	4	671	6.3	71	59	22	0.71	-0.01	0.8	2.3	0.06	0.32	25	8.9	0.42	-19	-83	226/280	
E2.7	1	432	5.0	80	84	28	1.09	0.72	1.6	3.0	0.07	0.07	183	3.2	-1.0	97	-33	380/410	3
	2	307	6.2	108	98	24	0.83	0.15	4.2	4.9	0.03	0.07	253	2.5	0.59	108	-116	442/440	1
	3	355	3.2	71	32	8.4	0.78	0.69	1.5	3.0	0.02	0.30	32	6.0	0.80	-98	26	383/370	
	4	431	14	136	118	34	0.76	0.69	4.4	5.0	0.01	0.12	220	5.8	0.89	-127	6.6	355/370	
	5	373	6.6	100	103	36	1.06	0.43	2.8	4.0	0.02	0.10	115	5.1	-0.59	-3.1	19	335/380	4
	6	500	1.8	150	158	38	1.1	-0.03	4.5	5.1	0.18	0.01	988	8.0	1.4	73	-3.3	165/360	<i>ex situ</i>
E2.6	1	338	5.5	96	66	30	0.46	0.87	3.0	3.9	0.03	0.21	44	5.8	0.33	-173	38	411/380	
	2	342	24	200	199	43	0.99	0.67	12	8.0	0.01	0.03	257	2.9	0.12	1.3	-46	438/440	mer. 2,4
	3	476	21	158	148	46	0.88	0.98	4.7	4.9	0.16	0.05	965	2.6	0.23	14	7.0	451/440	<i>ex situ</i> 6
	4	252	8.1	125	109	53	0.77	0.97	5.8	5.4	0.05	0.05	309	1.3	0.02	79	11	569/520	5
	5	338	3.2	75	57	23	0.58	0.29	1.8	3.0	0.01	0.19	79	7.7	-1.1	-35	84	305/350	
	6	391	1.8	41	28	25	0.48	0.17	0.4	1.5	0.05	0.68	52	7.7	0.28	-34	-44	309/350	low c
	7	454	4.2	73	64	41	0.75	0.19	1.3	2.6	0.08	0.05	152	4.7	-0.19	53	-129	410/410	
	8	252	2.1	66	29	22	0.20	-0.34	1.7	3.0	0.01	0.03	158	4.2	-0.47	-3.8	-75	306/420	
E2.4	1	609	10	94	91	81	0.92	0.95	1.5	3.3	0.06	0.17	136	5.1	-0.20	-61	-43	393/410	6
	2	432	4.1	69	33	18	0.23	-0.2	1.2	2.9	0.04	0.51	89	5.3	0.01	-164	-25	363/410	
	3	552	5.4	64	24	14	0.14	0.40	0.8	2.4	0.06	0.59	77	7.7	-1.0	-1.9	-2.4	321/360	
	4	411	9.7	110	91	30	0.69	0.61	0.4	4.8	0.05	0.10	319	5.1	0.05	84	86	426/410	interact 1
	5	391	5.6	91	66	32	0.53	-0.39	2.3	4.1	0.03	0.12	363	4.5	0.17	66	2.7	301/410	interact
	6	432	9.6	108	105	25	0.94	0.68	2.8	4.5	0.03	0.13	128	4.2	0.14	42	-3.8	470/410	5
	7	307	3.8	87	89	30	1.03	-0.03	2.8	4.5	0.02	0.04	244	7.9	-0.95	-29	-50	318/360	7
E2.3	1	411	13	135	136	41	1.01	0.94	4.7	7.6	0.03	0.08	226	3.0	0.27	34	-20	523/480	1
	2	307	5.3	98	55	24	0.31	-0.01	3.3	6.5	0.01	0.22	36	7.5	0.34	-84	-24	369/330	
	3	525	8.4	95	99	21	1.09	1.0	1.8	4.8	0.02	0.12	78	8.8	0.2	-2.8	24	308/330	
	4	307	3.9	84	77	56	0.84	0.69	2.4	5.5	0.01	0.17	70	8.1	0.00	61	-20	319/330	
	5	411	8.2	108	115	24	1.14	0.96	3.1	6.2	0.04	0.05	372	3.5	-0.27	127	45	414/460	interact 5
	6	411	12	132	123	52	0.86	0.59	4.8	7.8	0.03	0.05	240	3.6	-0.04	69	29	414/460	interact 6
	7	736	21	125	127	62	1.04	0.34	2.3	5.3	0.09	0.06	285	4.0	-0.07	17	27	396/440	mer. 4,7
E2.2	1	740	6.8	63	54	22	0.74	0.98	0.5	2.8	0.10	0.61	360	7.2	0.00	-6.2	-5.2	326/360	
	2	432	12	129	121	31	0.88	0.97	4.1	7.5	0.02	0.07	148	5.2	0.35	32	-16	420/420	2
	3	638	12	104	111	58	1.14	0.64	1.8	5.0	0.05	0.08	198	6.3	0.37	14	1.0	386/380	interact 3
	4	525	12	113	118	22	1.10	0.99	2.5	5.9	0.05	0.18	192	4.8	0.12	101	29	393/420	interact 4
	5	350	15	130	128	72	0.97	0.98	4.2	7.7	0.10	0.03	634	1.5	-0.08	115	6.5	534/510	5
	6	638	9.2	87	88	29	1.02	0.89	1.2	4.1	0.07	0.14	273	5.4	-0.08	-51	5.5	397/400	
E2.1	1	552	34	179	194	83	1.18	0.98	6.1	7.4	0.06	0.08	389	2.2	-0.08	-45	4.9	537/490	mer. 3,4
	2	411	25	180	165	64	0.84	0.98	8.2	8.6	0.04	0.06	313	2.4	0.02	-21	13	440/500	mer. 2,6
E2.0	1	278	3.4	80	71	20	0.80	0.98	2.3	4.0	0.02	0.17	84	5.4	-0.05	105	11	441/430	